Title

INTEGRATED ABSORPTION COEFFICIENTS FOR SEVERAL VIBRATION-ROTATION TRANSITIONS OF THE GAS PHASE HYDROXYL RADICAL USING A TUNABLE DIODE LASER

Author

Podolske, J.R.

Publication Date

1981-09-01

Lawrence Berkeley Laboratory
UNIVERSITY OF CALIFORNIA

Materials & Molecular
Research Division

INTEGRATED ABSORPTION COEFFICIENTS FOR SEVERAL VIBRATION-ROTATION TRANSITIONS OF THE GAS PHASE HYDROXYL RADICAL USING A TUNABLE DIODE LASER

James Robert Podolske
(Ph.D. thesis)

September 1981

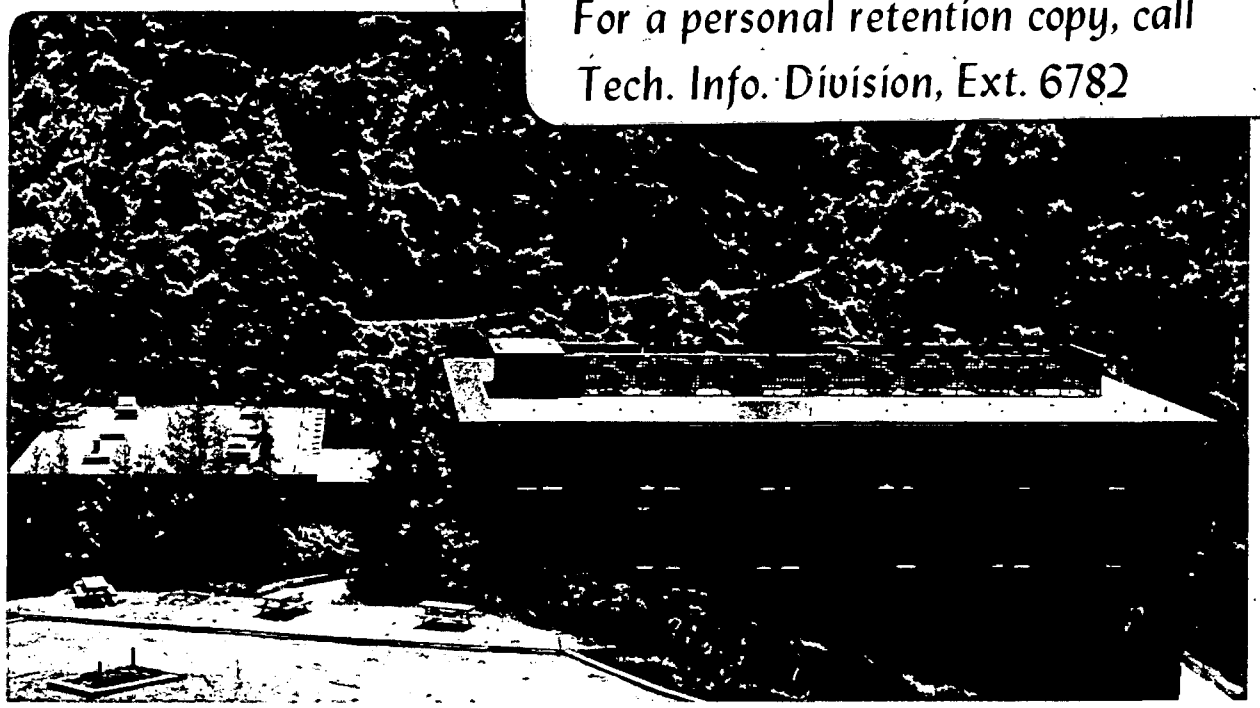

Prepared for the U.S. Department of Energy under Contract W-7405-ENG-48

DISCLAIMER

LBL-13218

INTEGRATED ABSORPTION COEFFICIENTS FOR SEVERAL VIBRATION-ROTATION TRANSITIONS OF THE GAS PHASE HYDROXYL RADICAL USING A TUNABLE DIODE LASER

James Robert Podolske

Materials and Molecular Research Division
Lawrence Berkeley Laboratory
and
Department of Chemistry
University of California
Berkeley, California 94720

September 25, 1981

This work was supported by the Director, Office of Energy Research, Office of Basic Energy Sciences, Chemical Sciences Division of the U.S. Department of Energy under Contract No. W-7405-ENG-48.

TABLE OF CONTENTS

INTEGRATED ABSORPTION COEFFICIENTS FOR SEVERAL VIBRATION-ROTATION TRANSITIONS OF THE GAS PHASE HYDROXYL RADICAL USING A TUNABLE DIODE LASER

James Robert Podolske

Materials and Molecular Research Division
Lawrence Berkeley Laboratory
and
Department of Chemistry
University of California
Berkeley, California 94720

ABSTRACT

Integrated absorption coefficients for several vibration-rotation transitions of the gas phase OH radical have been measured for the first time. The rate constant for the electronic energy transfer reaction between the excited oxygen molecule, $O_2(^1\Delta_g)$, and the ground state HO_2 radical has also been measured.

The molecular modulation technique was combined with high resolution diode laser spectroscopy to observe four OH transitions near 3410 cm^{-1}. Hydroxyl radicals were produced by the photolysis of O_3 at 2537 Å in the presence of H_2O, and their time-dependent concentration calculated by numerical simulation of the complete photochemical system. The narrow linewidth of the diode laser (~3 x 10^{-4} cm^{-1}) allowed direct measurement of the absorption line profiles. The measured integrated absorption coefficients are:

$S(3407.6069\ cm^{-1}) = 3.26 \pm 1.52 \times 10^{-20}$ cm/molecule

$S(3407.9890\ cm^{-1}) = 2.87 \pm 1.58 \times 10^{-20}$ cm/molecule

$S(3421.9360\ cm^{-1}) = 1.64 \pm 1.22 \times 10^{-20}$ cm/molecule

$S(3422.0123\ cm^{-1}) = 1.85 \pm 1.32 \times 10^{-20}$ cm/molecule

where the uncertainties listed are twice the standard deviation.

Photolysis of O_3 at 2537 Å in a flow system was performed, both with and without H_2O present, and steady state O_3 concentrations measured by UV absorption at 3150 Å. $O_2(^1\Delta)$ is a primary product of O_3 photolysis, and in a pure O_3 system each $O_2(^1\Delta)$ is responsible for the destruction of two additional O_3 molecules. With H_2O present, the $O(^1D)$ formed by O_3 photolysis reacts with H_2O to initiate generation of OH and HO_2. The change in O_3 upon addition of H_2O reflects the inhibition of $O_2(^1\Delta)$ destruction of O_3 caused by HO_2 quenching of $O_2(^1\Delta)$,

$$HO_2(^2A'') + O_2(^1\Delta_g) \longrightarrow HO_2(^2A') + O_2$$

Careful numerical simulation of this system under a variety of conditions allowed determination of the rate constant for this quenching process:

$$k_Q = 3.3 \pm 1.6 \times 10^{-11} \text{ cm}^3/\text{molecule s}$$

Sensitivity of this result to the uncertainty in the rate constant for the radical termination reaction $OH + HO_2$ was also investigated.

Harold S. Johnston

INTEGRATED ABSORPTION COEFFICIENTS FOR SEVERAL VIBRATION-ROTATION TRANSITIONS OF THE GAS PHASE HYDROXYL RADICAL USING A TUNABLE DIODE LASER

James Robert Podolske

I. INTRODUCTION

The hydroxyl radical and the hydroperoxyl radical are both important reaction intermediates in many gas phase chemical systems, including combustion environments,[1,2] interstellar space,[3,4] and the earth's troposphere[5,6] and stratosphere.[7,8] Understanding the behavior of such systems requires detailed knowledge about elementary reaction processes between these radicals and other species present in the system, and the ability to measure these radicals in the system directly. A complete understanding of stratospheric chemistry, in particular, is critical, as it is dominated by the ozone layer, which protects the earth's surface from short wavelength ultraviolet radiation.[9]

Although there has been a continual improvement over the last decade in the understanding of the reaction mechanisms, transport dynamics, photochemical processes and trace species distributions of the stratosphere, discrepancies still exist between observed trace chemical species distributions and those predicted by numerical models of this region.[7,10] Since OH and HO_2 play critical roles in the catalytic cycles of NO_x, ClO_x, and HO_x radicals, which destroy O_3 in the natural stratosphere, improved knowledge of their abundances and interactions with other species is necessary.

The purpose of this research was to determine integrated absorption coefficients for several vibration-rotation transitions of the OH radical and further characterize the energy transfer reaction between the HO_2 radical and electronically excited oxygen, $O_2(^1\Delta_g)$.

These results suggest new methods for monitoring the OH and HO_2 radicals in the stratosphere.

A. OH Infrared Spectroscopy

The spectroscopy of the hydroxyl radical has been studied extensively over the last several decades because of its participation in many diverse systems. The first spectroscopic studies of OH were done on the $A\ ^2\Sigma \leftarrow\!- X^2\pi$ system in the 2800-3200 Å region, initially observed in hydrocarbon flames and electric discharges in water vapor, because of its high absorption and emission intensities and the convenient wavelength range. This system has been utilized extensively both in absorption and emission to probe OH concentrations in a variety of environments, and several analyses of this system have been done.[11-14] The most recent work by Goldman and Gillis[14] gives line positions and line intensities relevant to low (240 K) and high (4600 K) temperature studies for this system. The results of studies in this region have been used in determining spectroscopic constants for the $X^2\pi$ ground electronic state.

The discovery by Meinel[15,16] of infrared vibration-rotation emission from vibrationally excited OH originating in the upper mesosphere and lower thermosphere from the exothermic reaction:

$$H + O_3 \longrightarrow OH\ (v \leq 9) + O_2 \qquad (1)$$

produced more spectroscopic information about the $^2\pi_i$ ground electronic state of OH and increased interest in the role of this radical in upper atmospheric photochemistry. Since then high

resolution emission spectra of OH from intense sources were observed, and accurate line position data for OH transitions in the 0.9–3.7 μm region obtained.[17] These data were combined with line position data from the $A^2\Sigma \leftarrow\!- X^2\pi$ system and microwave frequency data obtained from studies of the Λ splittings of low J $^2\pi_i$ levels to give very good molecular constants and term values for the $X^2\pi_i$ state for $v \leq 5$.[18]

Although transition frequencies for the hydroxyl radical are known accurately from experiment and theory, information on integrated absorption coefficients (also called line intensities) has been restricted to results of theoretical calculations[19] and inference from emission studies.[20] Previously, no direct experimental determination of integrated absorption coefficients of OH vibration-rotation transitions had been made. This is because of the difficulty of preparing large concentrations of the radical, the relatively weak oscillator strength of these transitions and, previously, the lack of a spectral source with narrow enough linewidth to accurately probe the absorption lines of these transitions. In this study a narrow linewidth tunable diode laser was coupled with a molecular modulation spectrometer to directly measure integrated absorption coefficients of several vibration-rotation transitions of the OH radical.

B. $HO_2 - O_2(^1\Delta_g)$ Collisional Energy Transfer

The photolysis of O_3 in the Hartley band has been shown to yield mainly excited products,[21,22] O_2 and O:

$$O_3 + h\nu \longrightarrow O_2(^1\Delta_g) + O(^1D_2) \qquad \phi \simeq 0.9 \qquad (2)$$

$$O_3 + h\nu \longrightarrow O_2 + O \qquad \phi \simeq 0.1 \qquad (3)$$

In a pure ozone system, further O_3 destruction occurs by the reactions:

$$O(^1D) + O_3 \longrightarrow O + \tfrac{3}{2} O_2 \ (\Sigma \text{ all channels}) \qquad (4)$$

$$O_2(^1\Delta) + O_3 \longrightarrow O_2 + O_2 + O \qquad (5)$$

$$O + O_3 \longrightarrow O_2 + O_2 \qquad (6)$$

If O_2 and other buffer gas are present, additional reactions need to be considered:

$$O(^1D) + M \longrightarrow O + M \qquad (7)$$

$$O_2(^1\Delta) + M \longrightarrow O_2 + M \qquad (8)$$

$$O + O_2 + M \longrightarrow O_3 + M \qquad (9)$$

When water is added to an $O_3 - O_2$ mixture, a chain reaction occurs to destroy ozone by the elementary steps:

initiation $\quad O(^1D) + H_2O \longrightarrow OH + OH \qquad (10)$

chain $\quad OH + O_3 \longrightarrow HO_2 + O_2 \qquad (11)$

$$HO_2 + O_3 \longrightarrow OH + O_2 + O_2 \qquad (12)$$

termination $OH + HO_2 \longrightarrow H_2O + O_2$ (13)

$HO_2 + HO_2 \longrightarrow H_2O_2 + O_2$ (14)

This mechanism predicts that photolysis of a flowing O_3 mixture would produce a steady state O_3 concentration that would decrease when water was added to the mixture. However, in preliminary experiments, under some conditions just the opposite effect was observed. Numerical simulation of the system with an expanded reaction set, in which key reaction rate constants were varied over their estimated uncertainty range,[23] yielded results which agreed qualitatively with the predictions of the above mechanism. If the destruction of O_3 by the O_x reactions is partially inhibited by the quenching of $O_2(^1\Delta)$ by the hydroperoxyl radical, according to the proposed mechanism:

$$HO_2\ (^2A'') + O_2(^1\Delta_g) \longrightarrow HO_2(^2A') + O_2(^3\Sigma_g^-)\ \Delta E \simeq 75\ cm^{-1} \qquad (15)$$

then adjustment of the rate constant for this process in the numerical simulation brought the calculated ozone behavior into agreement with experiment. Since O_3-H_2O systems are widely used to investigate HO_x chemistry,[24-26] further investigation was indicated.

The possibility of rapid energy transfer between $O_2(^1\Delta)$ and HO_2 has been postulated for some time.[27] Evidence of the $^2A'$ first excited state of HO_2 predicted by Walsh[28] came first from theoretical studies[29,30] and later from emission[27,31,32] and absorption studies.[33] Investigation of the near infrared emission

bands of HO_2 by Becker et al.[27] produced the first evidence that this $^2A' \longrightarrow {}^2A''$ emission was being pumped by O_2 ($^1\Delta$), for which excitation to $^2A'(\nu_3 = 1)$ was energetically possible. This pumping mechanism was later used to probe HO_2 concentrations in a flow tube by addition of metastable oxygen to the flow and observing the resultant $^2A'(000) \longrightarrow {}^2A''(000)$ emission at 1.43 μm.[34] Indirect evidence that this rapid electronic-electronic energy transfer process should occur comes from analogy with several observed near-resonant processes:[35,36]

$$Tl\ (^2P_{1/2}) + O_2(^1\Delta_g) \rightleftarrows Tl\ (^2P_{3/2}) + O_2(^3\Sigma_g^-) \qquad (16)$$

$$I(^2P_{3/2}) + O_2(^1\Delta_g) \rightleftarrows I(^2P_{1/2}) + O_2(^3\Sigma_g^-) \qquad (17)$$

Although Becker[34] states that the HO_2-$O_2(^1\Delta)$ transfer is fast, no quantitative study of this exchange rate has been done.

In this study a flowing O_3-H_2O system was investigated over a range of O_3 and H_2O concentrations and photolysis intensities, and numerically simulated to obtain a best estimate for the HO_2 + $O_2(^1\Delta)$ energy transfer rate constant.

II. EXPERIMENTAL METHODS AND APPARATUS

A. Methods

A combination of standard ultraviolet spectroscopy and high resolution diode laser infrared spectroscopy was employed in this study to measure steady state and time dependent concentrations of the chemical species of interest. The range of O_3 concentrations used in this work indicated 3150 Å as the optimal wavelength to monitor this species. H_2O was measured with the diode laser at 3406.675 cm^{-1}, since the strength of this water line had been measured previously. Finally, the OH radical was observed at four vibration-rotation transition frequencies around 3415 cm^{-1}, again employing the tunable diode laser.

1. Steady State Photolysis. In order to investigate the HO_2-$O_2(^1\Delta)$ quenching reaction, a chemical system is needed in which both these transient species can be produced in high enough concentration so that their interaction affects an observable property of the system. Such a system was discovered, quite accidentally, during preliminary investigation of a flowing O_3-H_2O mixture irradiated by ultraviolet light.

The method employed for this investigation involved steady state photolysis of both O_3-He (dry ozone) and O_3-H_2O-He (wet ozone) mixtures at 2537 Å, the peak of ozone's Hartley band absorption. In the O_3-He system, $O_2(^1\Delta)$ is produced by the simple mechanism:

$$O_3 + h\nu \longrightarrow O_2(^1\Delta) + O(^1D) \quad (18)$$

$$O(^1D) + O_3 \longrightarrow O + 3/2\ O_2\ (\Sigma \text{ all channels})^{37} \quad (19)$$

$$O_2(^1\Delta) + O_3 \longrightarrow O + O_2 + O_2 \quad (20)$$

$$O + O_3 \longrightarrow O_2 + O_2 \quad (21)$$

which predicts a quantum yield for O_3 destruction of 5, in reasonable agreement with experiment.[38] Measurement of steady state O_3 concentration in the reaction cell both before and during irradiation and knowledge of gas flow rate through the cell allows direct determination of the primary photolytic rate constant.

Addition of H_2O to the O_3–He mixture produces the required HO_2 radicals by the following elementary steps:

$$O(^1D) + H_2O \longrightarrow OH + OH \quad (22)$$

$$OH + O_3 \longrightarrow HO_2 + O_3 \quad (23)$$

$$HO_2 + O_3 \longrightarrow OH + O_3 \quad (24)$$

$$OH + HO_2 \longrightarrow H_2O + O_2 \quad (25)$$

$$HO_2 + HO_2 \longrightarrow H_2O_2 + O_2 \quad (26)$$

$$HO_2 + O_2(^1\Delta) \longrightarrow HO_2 + O_2 \quad (27)$$

As described in the introduction, this second set of reactions can be considered a chain reaction in which the OH and HO_2 radicals catalytically destroy ozone. These reactions inhibit the O_x destruction mechanism both by scavenging the $O(^1D)$ produced in the initial photolysis of O_3 as well as quenching the $O_2(^1\Delta)$ also

produced. Experimental conditions were selected to make the HO_2 concentration relatively large, so that it might compete effectively with O_3 for the $O_2(^1\Delta)$, while keeping the HO_x catalytic chain relatively short, so that the decrease in O_3 destruction caused by (27), the process of interest, was not blanketed by a large increase in O_3 destruction from the HO_x chain. After the first two measurements on the dry ozone system were made, a stream of H_2O-He was added to the O_3-He stream flowing through the cell. The ozone concentration was measured as the H_2O concentration went from zero (dry ozone case) to its final steady state value (wet ozone case). This change in steady state ozone was then used as the diagnostic for $O_2(^1\Delta)$ quenching by the HO_2 radical.

The sequence of ozone measurements just described was performed for a series of conditions, over a range of water and ozone concentrations and photolysis intensities. To extract the desired quenching rate constant from the ozone measurement, a comprehensive reaction set, described in Appendix A, was employed in a numerical simulation of the experimental system. The simulation program is described in a later section. Variation of the quenching rate constant in the numerical model revealed the value of this parameter for which the root-mean-square deviation between experimental and calculated O_3 concentrations for all the experiments in the series was a minimum. Also, sensitivity of this minimum value to variation in the rate constants for other key reactions in the mechanism was explored.

2. Molecular Modulation with Diode Laser Detection. Quantitative measurement of hydroxyl radical infrared absorptions requires:

1) absolute measurement of absorption linewidths which are much smaller than the resolution of conventional spectrometers employing grating monochromators or interferometers,
2) absolute measurement of the transient hydroxyl radical concentration in a system where this concentration is both large and uniform,
3) absolute measurement of extremely small absorption signals.

These restraints are true, in general, for any short-lived species, and have hindered exploitation of the selectivity which the infrared region offers in detecting such species.

The development of the tunable diode laser in recent years has helped overcome the first of these restraints, by providing spectroscopists with a source of infrared radiation which has a spectral linewidth much smaller than the doppler width of molecular absorptions in this wavelength region and an output frequency tunable over a 20-100 cm^{-1} range.[39] This laser system has recently been employed to make band strength measurements on the diatomic gas phase radicals ClO[40] and BF.[41] The diode laser used in this study, with a manufacturer's stated linewidth of ~3 x 10^{-4} cm^{-1}, could accurately probe the absorption profile of the OH transitions investigated, which were found to be about 30 percent broader than their doppler broadened width, calculated to be 0.010 cm^{-1}. An alternative to using a narrow linewidth spectral source is to pressure broaden the absorption lines

until their widths are comparable to the resolution of a more conventional spectrometer, but this causes the absorption at the peak to decrease inversely to the linewidth, making the absorption signals, which are already small for doppler broadened lines, even smaller.

The second requirement, that of producing a known concentration of hydroxyl radicals which is both spatially uniform and relatively large, was met by employing the same O_3-H_2O system as was described in the last subsection. This system was calculated to be capable of producing OH concentrations greater than 10^{12} molecules/cm^3, which is very good for such a reactive radical. The photolytic reaction cell, which will be described in detail later, was designed so that reactant flow in and product flow out kept the contents of the cell evenly distributed. Spatial uniformity of OH also required that the absorption of the photolytic light by the system be uniform. This was accomplished by keeping the steady state O_3 concentration in the cell during the experiments at or below 2.4×10^{15} molecules/cm^3, which kept spatial deviations in photolytic rate due to finite optical density below 2 percent.

The absolute concentration of hydroxyl radical was determined, as before, by numerical simulation of the reaction cell chemistry. This calculation required knowledge of the rate constants for all the elementary processes in the reaction set, as well as the photolysis light flux, the reaction cell flow rate constant (f/V), and the flow rates of H_2O and O_3 into the cell. The photolysis light flux and

O_3 flow in rate were determined, as in the earlier HO_2-$O_2(^1\Delta)$ experiments, by measuring the O_3 concentration both with and without the photolysis lamps turned on. The H_2O flow rate was determined from a measurement of the steady state H_2O concentration in the cell by a high resolution infrared absorption technique, combined with knowledge of the cell total pressure and flow rate constant during the measurement. The reaction cell flow rate constant was determined two ways: by combining a measurement with a calibrated flowmeter of the total gas flow through the cell and a measurement of the cell volume to get f/V, and directly by monitoring the decay of the O_3 concentration in the cell when addition of O_3 to the flow stream into the cell was terminated. An estimate of the uncertainty in the calculated OH concentration required calculating the sensitivity of OH to several key reaction rate constants.

Meeting the third stated requirement, making absolute measurement of extremely small absorption signals, can be approached in several ways. The most obvious approach was to tune the diode laser through the region where an OH line is known to exist and measure the absorption directly. Unfortunately, even with the large radical concentrations ($\sim 10^{12}$ cm^{-3}), the long absorption path (~30m) and absorption lines nearly as narrow as their doppler limit, the direct absorption signals were smaller than 1 percent, and could not be observed.

The most sensitive technique, to date, for measuring small absorptions with a diode laser is derivative spectroscopy, which has

recently been the subject of an excellent review.[42] Direct absorption measurements require observing small changes in a large D.C. level. This observation is limited by the noise and drift of the D.C. level and the slope of the baseline caused by the slit function of the monochromator, used to select the desired laser mode. Derivative spectroscopy takes advantage of the rapid tunability of the laser to measure the derivative of the absorption by modulating the laser frequency over a small interval and synchronously detecting changes in laser power transmitted through the absorption system at the modulation frequency. In the limit that the interval over which the laser frequency is modulated is small compared to the absorption linewidth, this method produces a signal proportional to the first derivative of the absorption at the central laser frequency. Similarly, detecting at twice the modulation frequency produces a signal proportional to the second derivative. When the laser frequency is scanned through an absorption, a complete first or second derivative of the absorption profile is produced. The advantage of observing the first derivative profile is that the derivative of the large D.C. baseline which caused problems in direct absorption is either zero, if spectrometer throughput versus laser frequency is flat, or a constant, as in the case where throughput versus frequency is a nearly triangular slit function, while the derivative of the absorption consists of both a positive and negative going lobe. Second derivative spectroscopy further reduces the problem of finite background signal and produces two negative and one large positive lobe. A diode laser spectrometer

optimized for second derivative detection has been reported[43] to have an absorption limit of better than 10^{-5}. Both first and second derivative techniques were used in this study to locate small absorptions.

While derivative spectroscopy is sensitive, absolute determination of absorbance by this technique is difficult. Although the mathematical treatment requires the laser frequency modulation amplitude to be small compared to the absorption linewidth, best sensitivity results when the two are about equal.[44] This results in distortion of the measured signal from that of the true derivative. Conversion of the derivative signal to absorbance also requires knowing the absolute laser frequency modulation amplitude, which is difficult to experimentally determine, and the D.C. laser intensity, to which the preamplifier of the infrared detector does not respond. This technique is best applied to measuring unknown concentrations of a species, by calibration of the derivative signal amplitude with a known concentration of that species, as has been done recently with N_2O.[45]

An alternate method to modulate the desired absorption signal, so that phase sensitive detection can be used to measure it, is to modulate the hydroxyl radical concentration directly. This technique, called molecular modulation spectroscopy, has been developed in this laboratory previously.[46] The basic concept is that by modulating the photolysis intensity in some periodic fashion, fluctuations in reactant, intermediate and product concentrations are induced and may be measured at the same frequency. Analysis of the differential

equations governing the chemical system, either by analytic solutions or numerical simulation, can either predict the amplitudes of the concentration modulation of each species and their phase relative to the photolysis lamps, or conversely, can predict values for rate constants and absorption cross sections from measured modulation amplitudes and phase shifts. From an elementary viewpoint, information about a species' chemical lifetime in the system is being determined by this frequency domain technique, much as fluorescence lifetimes are measured in phase shift fluorometry.[47,48] While earlier workers chose to modulate their photolysis lamps in an "on-off" square wave fashion,[49] in this study the lamp intensity was modulated sinusoidally about a D.C. level, to reduce the complexity of the analysis.

To better illustrate the information content of a molecular modulation experiment, consider the following simple system:

$$\longrightarrow A \qquad k_f A' \qquad (28)$$

$$A \longrightarrow \qquad k_f \qquad (29)$$

$$A + h\nu \longrightarrow B \qquad j_o + j_1 e^{i\omega t} \qquad (30)$$

$$B + C \longrightarrow D \qquad k_B \qquad (31)$$

$$D \longrightarrow \qquad k_f \qquad (32)$$

where (28) represents flow-in and (29) and (32) represent flow-out. Complex notation is used to express the photolytic excitation, but final results will be taken as the real part of the derived solutions, following the example of Hunziker.[50] Mathematical intuition suggests that the solutions for species A, B and D (assuming C is constant), can be expressed to good approximation by a truncated Fourier series:

$$A = A_o + A_1 e^{i(\omega t+\phi_A)}$$

$$B = B_o + B_1 e^{i(\omega t+\phi_B)} \tag{33}$$

$$D = D_o + D_1 e^{i(\omega t+\phi_D)}$$

The resulting coupled differential equations describing this system then become

$$\dot{A} = i\omega A_1 e^{i(\omega t+\phi_A)} = k_f A' - k_f A_o - k_f A_1 e^{i(\omega t+\phi_A)} - j_o A_1 - j_o A_1 e^{i(\omega t+\phi_A)} - j_1 A_o e^{i\omega t} - j_1 A_1 e^{i(2\omega t+\phi_A)} \tag{34}$$

$$\dot{B} = i\omega B_1 e^{i(\omega t+\phi_B)} = j_o A_o + j_o A_1 e^{i(\omega t+\phi_A)} + j_1 A_o e^{i\omega t} + j_1 A_1 e^{i(2\omega t+\phi_A)} - k_B B_o C - k_B B_1 C e^{i(\omega t+\phi_B)} \tag{35}$$

$$\dot{D} = i\omega D_1 e^{i(\omega t+\phi_D)} = k_B B_o C + k_B B_1 C e^{i(\omega t+\phi_B)} - k_f D_o - k_f D_1 e^{i(\omega t+\phi_D)} \tag{36}$$

Each equation can be separated into a time dependent and a time independent part. To simplify the solution, the second harmonic terms such as $j_1 A_1 e^{i(2\omega t+\phi)}$ are ignored, and since j_o and j_1 are usually of equal magnitude whereas A_1/A_o is generally 10^{-3} or less, the terms $j_o A_1$ are also deleted since they are much smaller than $j_1 A_o$. The steady state solutions can now be written:

$$A_o = k_f A'/(j_o + k_f)$$

$$B_o = j_o A_o / k_B C \qquad (37)$$

$$D_o = k_B C / k_f$$

Similarly, the expression for the time dependent part of the species concentrations are:

$$A_1 = j_1 A_o/(k_f^2 + \omega^2)^{1/2} \qquad \phi_A = \tan^{-1}(-\omega/k_f) + 180^\circ \qquad (38)$$

$$B_1 = j_1 A_o/(k_B^2 C^2 + \omega^2)^{1/2} \qquad \phi_B = \tan^{-1}(-\omega/k_B C) \qquad (39)$$

$$D_1 = k_B B_1/(k_f^2 + \omega^2)^{1/2} \qquad \phi_D = \tan^{-1}(-\omega/k_f) + \phi_B \qquad (40)$$

Under most experimental conditions the flashing frequency ($\omega/2\pi$) is much faster than the cell turnover rate constant k_f, so the terms $\tan^{-1}(-\omega/k_f) \simeq -90^\circ$ and $(k_f^2 + \omega^2/)^{1/2} \simeq \omega$. Qualitatively then, a reactant subject to photolysis, such as species A, will have a phase shift of $-90^\circ + 180^\circ = +90^\circ$ with respect to the photolysis lamps, and a modulation amplitude which decreases as ω^{-1}. A photochemical intermediate, such as species B, will have a phase shift between 0° and -90°, depending on the ratio $\omega/k_B C$, and an amplitude which is constant for $k_B C \gg \omega$ and decreases as ω^{-1} for $k_B C \ll \omega$. A product species, such as D, will have a phase shift between -90° and -180°, and an amplitude decreasing as ω^{-1} to ω^{-2} going between the low and high frequency limits as defined for B. Therefore, the

quadrant in which the phase shift of an observed absorption lies indicates whether it belongs to a photochemical reactant, intermediate or product. This is summarized in Fig. 1.

Closer inspection of the equation describing ϕ_B, the phase shift of the reaction intermediate with respect to the photolysis lamps, reveals that the chemical lifetime of B ($\tau_B = 1/k_BC$) can be determined by measuring ϕ_B as a function of flashing frequency. This measurement will be most sensitive when $\omega \simeq k_BC$, that is, when the intermediate is measured in its "tuned" region. The phase and normalized amplitude behavior of reaction intermediate B versus ω/k is shown in Fig. 2, where:

$$k = k_BC = 1/\tau_B \tag{41}$$

The equations describing B are completely analagous to the transfer function of a single pole low-pass filter; τ_B is equivalent to the RC time constant. While the results derived above for the simple system give a good first-order picture for OH in the O_3-H_2O system, final analysis relied on numerical simulation to obtain very accurate solution of the differential equations describing the system.

The method finally employed to measure the OH line strengths involved a combination of molecular modulation and diode laser spectroscopy. First the OH absorptions were found with derivative spectroscopy. Next the diode frequency was slowly scanned through the OH absorption line while the average laser intensity, I, and the in-phase and quadrature components, a and b, of the signal with respect

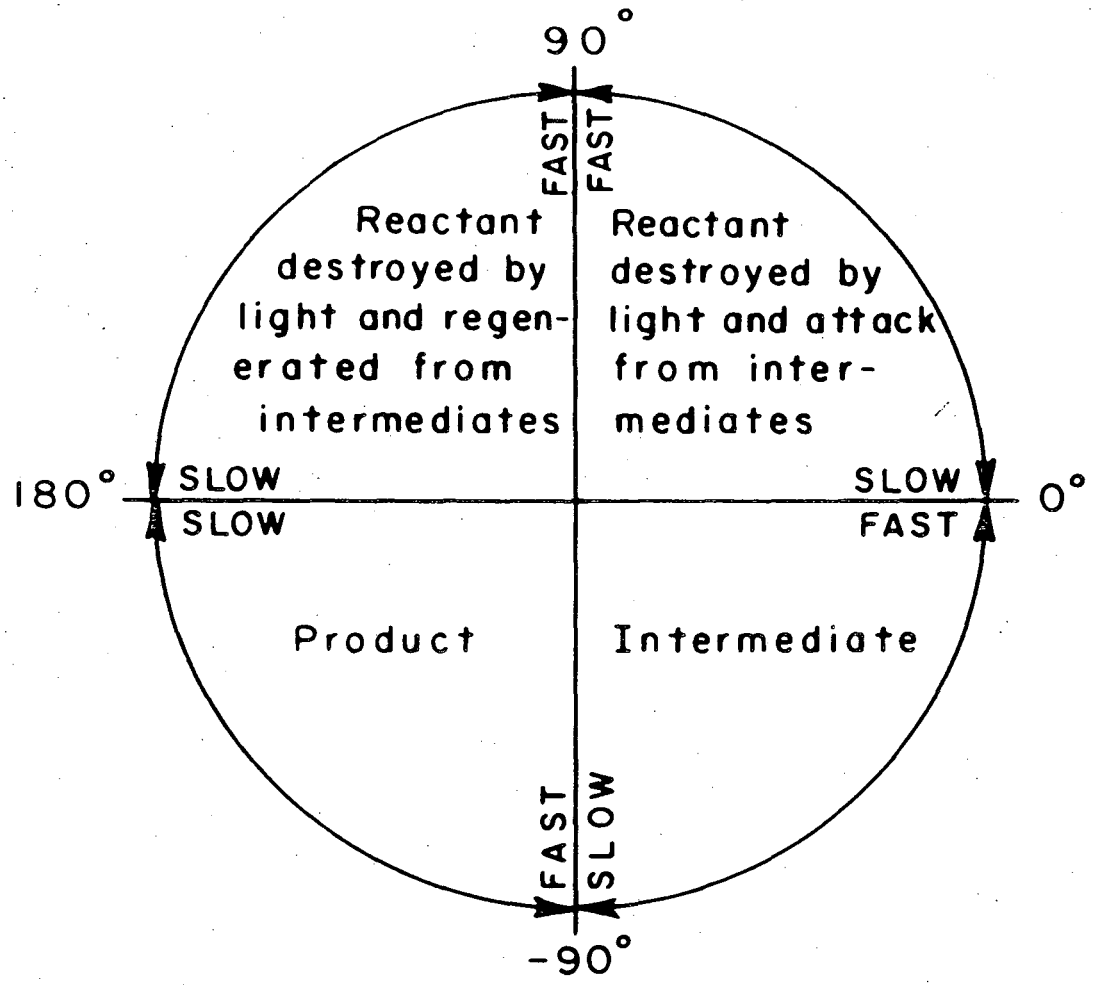

Fig. 1. Phase shifts of modulated reaction species.

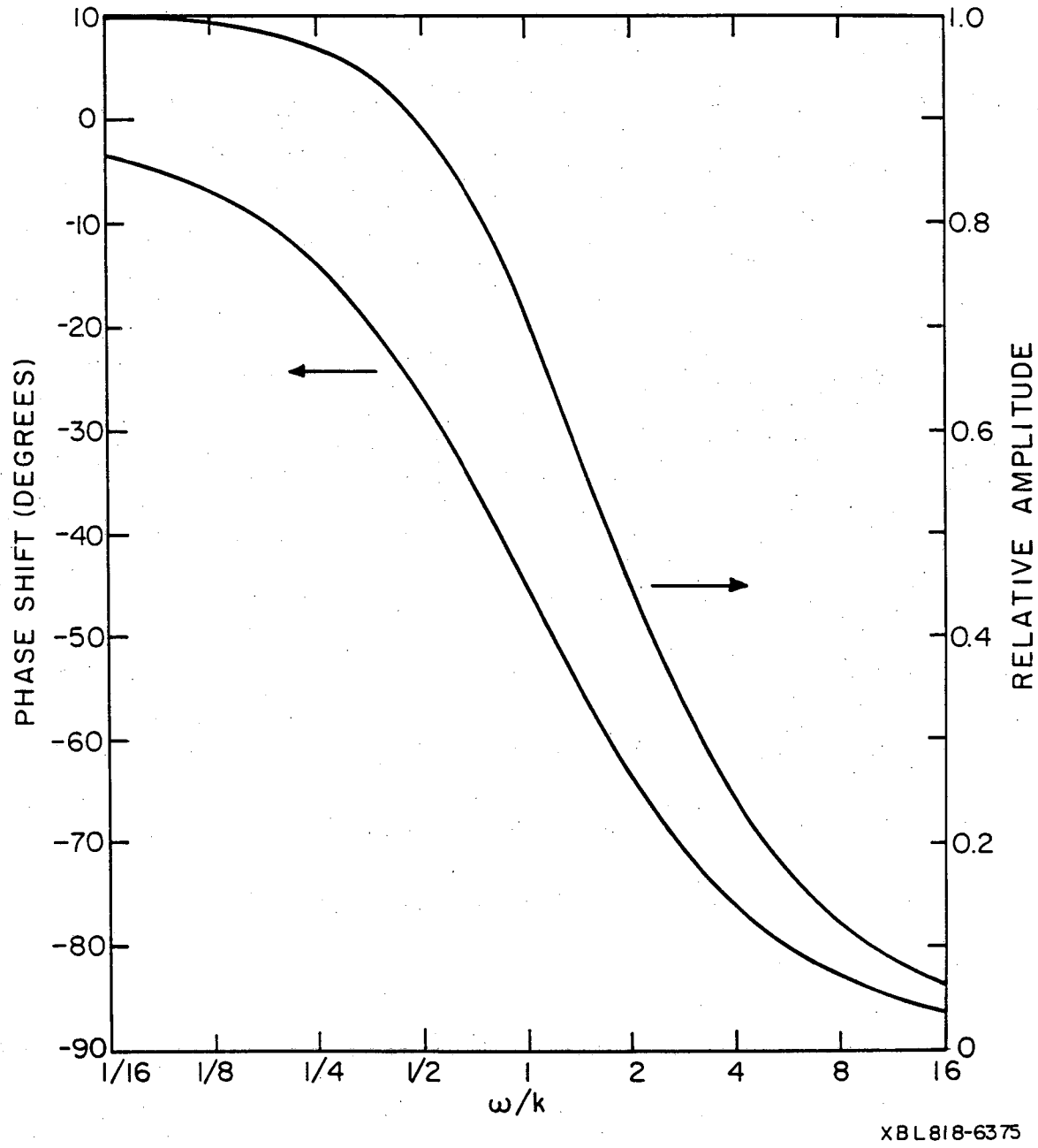

Fig. 2. Phase shift and normalized amplitude behavior of a reaction intermediate.

to the photolysis lamps were recorded. The modulation amplitude and phase were then calculated by the relations:

$$\Delta I = (a^2 + b^2)^{1/2} \tag{42}$$

$$\phi = \tan^{-1} (b/a) \tag{43}$$

The relationship between modulation amplitude and cross section is derived from the Beer-Lambert law for absorption of light, which relates the intensity of the beam transmitted through the cell to the incident intensity, the pathlength traversed, the number density of the absorbing species, and its absorption cross section

$$I = I_0 e^{-\sigma n l} \quad . \tag{44}$$

Taking the derivative of I with respect to number density gives

$$dI/dn = -\sigma l I_0 e^{-\sigma n l} \tag{45}$$

and since in all cases $\Delta I/I \sim 10^{-3}$, this can be rewritten as

$$\Delta I/\Delta n = -\sigma l I_0 e^{-\sigma n l} = -\sigma l I \tag{46}$$

$$\sigma = -\frac{\Delta I}{I \Delta n l} \tag{47}$$

Thus, combining the known pathlength, l, with the measured modulation amplitude and average laser intensity, ΔI and I, and the calculated concentration amplitude, Δn, gives the absolute cross section for OH. Finally the integrated absorption coefficient, or line strength

$$S = \int_{line} \sigma(\nu) d\nu \tag{48}$$

is calculated by integrating the measured cross section over the entire line. The phase shift information obtained during the experiment is needed to determine the cross section. However, comparison of both phase shift and amplitude as a function of flashing frequency as measured in the experiments with those predicted from calculation lends credence to the numerical model's ability to adequately describe the experimental system.

3. Numerical Simulation of the Chemical Systems. Exact analytical solutions for the chemical concentrations in a complex reaction system cannot, in general, be derived. Often the use of the steady state approximation for some species and assumptions about a rate-determining step will simplify matters so that approximate solutions may be written. These solutions are helpful in gaining insight about the mechanism and making qualitative predictions about the chemical system. However, when accurate time dependent solutions are required, especially for predicting subtle effects, numerical methods must be employed.

In this study all calculations of reaction cell chemistry were made by solving a complete reaction mechanism, as described in Appendix A, with a modified version of the CHEMK program.[51,52] This program employs the method of Gear[53] for numerically integrating the "stiff" set of first order differential rate equations which describe the system, to calculate the time dependent concentrations of each species. The code has been modified to simulate square wave and sinusoidal variation of photolytic intensity, as well as constant illumination. The integration subroutine, as implemented by Hindmarsh,[54] allows access to the Taylor series coefficients which describe concentration as a function of time in the interval between times at which concentrations are explicitly calculated. These allow very accurate calculation of the Fourier coefficients of each species at the photolysis flashing frequency, as the relative change in concentration is usually small and the time steps relatively large. For the sake of efficiency, modulation simulations are done by first calculating steady state concentrations of each species under constant light intensity conditions, and then calculating several modulation cycles under periodic photolysis. Comparison of the phase and amplitude information for the last several cycles reveals when the system has stabilized.

B. APPARATUS

1. Reaction Cell and Temperature Control. A schematic diagram of the experimental apparatus is presented in Fig. 3. The reaction cell is a cyclindrical quartz tube which has an inside diameter of 15 cm

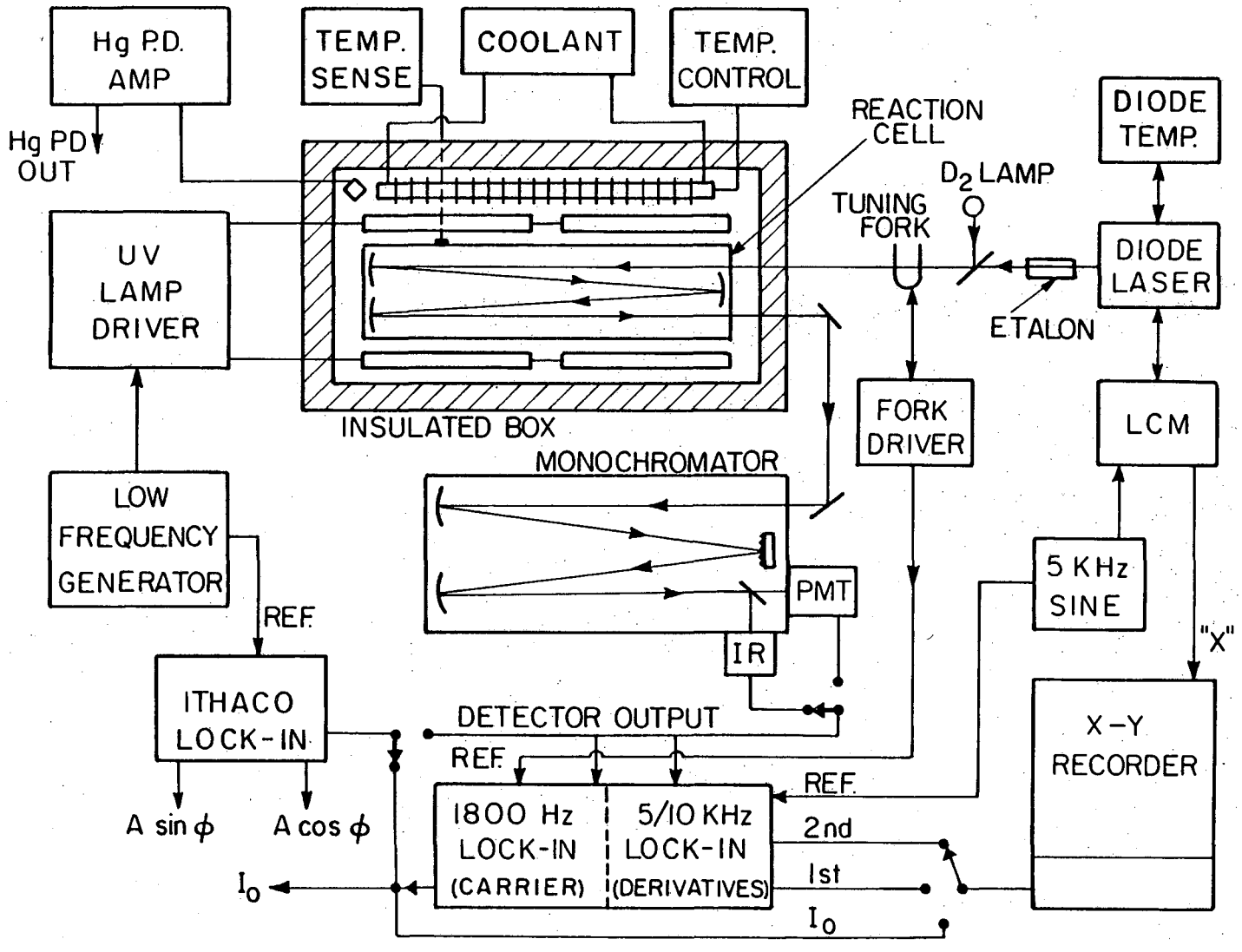

Fig. 3. Schematic diagram of experimental apparatus.

XBL 818-6378

and a length of 178 cm. The tube is closed at both ends by stainless steel endcaps which are mounted on a rigid steel frame and sealed onto the quartz tube with a compressed O-ring. Three 7.6 cm diameter spherical mirrors with a 185 cm radius of curvature are mounted in the endcaps to give multipass capability as first described by White.[55] Adjustment of the angle of the rear mirrors with respect to the optical axis by means of an external fine adjustment screw allows selection of a 742, 1482, 2222 or 2962 cm pathlength. The mirrors, which were custom fabricated by the John Unertl Optical Company to a specified radius of 185 ± 0.2 cm, are aluminum-coated and overcoated with 500 Å of magnesium fluoride both to maximize the ultraviolet reflectivity[56] near 2000 Å and to protect the aluminum from chemical attack from the strong oxidizers used in this investigation.[57] The calcium fluoride entrance and exit windows of the cell are O-ring mounted on the front end of the cell and transmit radiation from below 2000 Å in the ultraviolet to approximately 9.0 microns in the infrared. Silicone rubber was selected over Viton for all the O-rings used on the cell because it retains its elasticity better at low temperature and holds up better against attack from O_3 and H_2O_2. A liquid nitrogen trapped oil diffusion pump is capable of evacuating the cell to less than 10^{-2} Torr. The volume of the cell was determined, by a series of expansions of nitrogen gas from a calibrated bulb into the cell, to be 37.5 liters. The pressure in the cell is measured with a Baratron Model 310 BHS-1000 0-1000 Torr capacitance manometer with a stated accuracy above 10 Torr of 0.1 percent. The reaction cell and

entire optical train are mounted on a Newport Research Corporation vibration isolation table.

The entire cell assembly rests on 3" nylon pads to reduce the thermal conductivity between the steel table top and the cell compartment. The cell is separated from the table by 3" of rigid polyurethane foam board and 1/4" thick high density closed cell neoprene foam sheet. Also, the cell is enclosed in an insulated box, built with 2" thick aluminum-backed fiberglass. The optical probe beam passes through the insulated box via two evacuated glass tubes with calcium fluoride windows sealed on the ends. The cell compartment is cooled by a finned radiation coil mounted above the cell, through which cooling fluid, either methanol or chilled water, is circulated. Heat is added via three heating tapes set on top of the coil and connected in parallel. The air temperature in the box is regulated by driving the heaters with a proportional temperature controller, which employs a precision thermistor as a sensing element. A "squirrel cage" blower mounted inside the box circulates the air over the coil and reaction cell to keep the compartment temperature uniform. The temperature of the cell itself is monitored with eight solid state temperature sensors taped to the outside wall of the cell and one sensor mounted in a stainless steel thermowell that extends about 15 cm into the cell from the end opposite the optics. The sensors and their electronics are described in Appendix D. The air temperature in the box is sensed with mercury thermometers extending through the top of the box at each end. The temperatures determined by these sensors and thermometers agreed with each other to ±1.0 K.

2. Optical System. A kinematically mounted mirror at the front end of the optical train allows selection of any one of three spectroscopic light sources. In the first position is a Sylvania DE450A deuterium arc lamp powered by a modified Bausch and Lomb current regulated D.C. power supply which produces usable output in the 190–400 nm region of the ultraviolet. The second position, not shown in Fig. 3, accomodates either a 6 volt tungsten lamp for cell alignment or a Nernst glower for low resolution infrared work. The third position is for a Laser Analytics tunable diode laser. The diode laser system is an early manufacturing prototype; few were built, fewer sold, and no coherent documentation produced. Therefore, further description is indicated.

The diode laser system consists of several components. The actual emitter is a $Pb_{1-x}Cd_xS$ crystal, mounted on a gold-plated copper package, whose composition was selected so that it would produce gain in the 3400 cm^{-1} region. It was purchased from the Laser Analytics Division of Spectra-Physics as a Model SDL-10 laser diode (serial number 9261-17) capable of laser output covering 3405–3435 cm^{-1} (3395–3445 cm^{-1} measured). The diode laser package is mounted on a heatsink attached to the cold station of the cold head of a CTi Cryodyne Model 70 closed cycle helium refrigerator. A heating coil and a calibrated temperature sensitive diode attached to this heatsink allow the temperature controller (Lake Shore Cryotronics, Inc., Model DTC-500) to maintain the diode operating temperature anywhere between 10–70 K with stability of about 10^{-3} K. In order to maintain such

low temperatures and prevent air from condensing on the diode, the entire heatsink and cold station of the cold head are encased in a vacuum jacket with a KRS-5 window at one end. Course tuning of the diode output frequency is accomplished by adjusting this temperature. The diode emits when the current passing through it exceeds a characteristic threshold current. Variation of the diode current results in small changes in laser frequency, and so can be exploited for fine tuning the laser. The diode current is supplied by a Laser Analytics LPS-2 control module. The LPS-2 performs the following functions:

1) supplies a stable D.C. current through the diode which is set by the user on the front panel and read out on a 4-1/2 digit DVM,
2) supplies an additional ramping current to scan the diode at a rate selected by the user, and outputs a voltage proportional to the ramp to drive an X-Y recorder,
3) supplies a third current component to the diode which is proportional to a voltage presented by the user. This allows frequency modulation of the laser by an external oscillator for derivative techniques.

The cold head assembly (diode/heatsink/cold head) is mounted on an LOA optical assembly. The optical assembly provides an f/1 ZnSe lens on an X-Y-Z translation stage to convert the diverging laser beam (~60° cone) into a parallel beam, an iris for aperaturing the beam, and a

four position carousel to optionally insert a He-Ne alignment laser, a reference gas cell, or a 2.5 cm Ge etalon into the beam. The entire LOA assembly is mounted above the rest of the optical system on the table, and the laser beam is brought down to the lower optical plane with several mirrors. To make the beam compatible with the rest of the optical train, which is set up to handle radiation from point sources, the beam is focused at the proper distance from the source selection mirror with an f/2 calcium fluoride lens.

After the selection mirror, the probe beam encounters a 15 cm focal length spherical mirror which images it on to the slits of a Bulova 1800 Hz tuning fork chopper. A second 15 cm focal length spherical mirror after the chopper focuses the beam into the cell entrance slit. After making from 4 to 16 passes through the cell (depending on the rear mirror adjustment) the beam emerges and is focused with a third spherical mirror onto the slits of a McPherson Model 2051 one meter grating monochromator. This monochromator has snap-in gratings, so that switching between the 1200 line/mm grating blazed at 300 nm and the 300 line/mm grating blazed at 3.5 microns allows easy sequential monitoring in the middle ultraviolet and the middle infrared.

Three detectors were employed in the course of this investigation. An RCA 4832 photomultiplier tube was used in the visible to detect several Ne lines for wavelength calibration. The infrared detector is a Santa Barbara Research Center indium antimonide photovoltaic detector operated at liquid nitrogen temperature. It has

a 60° field of view, is 2.0 mm in diameter and responds to 1.0 to 5.5 micron radiation. The output of this detector is fed to a Santa Barbera Model A210 preamplifier which was optimized for this particular detector element. The third detector is an EMI 9783B photomultiplier tube which is particularly sensitive in the ultraviolet. Since the ultraviolet beam intensity was relatively large, the overall gain of the PMT is kept low by operating it with a total dynode string voltage of -600 VDC. To reduce statistical noise in the dynode string, the first stage gain is increased by holding the photocathode to first dynode voltage at a constant 100 volts with a Zener diode, as suggested by EMI.[58] A schematic of the PMT and its preamplifier are shown in Fig. 4. The InSb infrared detector and the EMI 9783B PMT are mounted on the two exit ports of the monochromator. Turning a lever on top of the monochromator moves an internal mirror which diverts the output from one detector to the other.

3. Photolysis Lamps and Monitor. The photolytic light for these experiments came from eight 30 watt General Electric G30T8 low pressure mercury germicidal lamps, which emit most of their output in the 2537 Å Hg line. Four of the 36" lamps are mounted along each side of the cell about 1" from the cell wall. Specially formed mirrors made out of high reflectance Alzak aluminum sheeting are placed around the lamps to increase both light intensity and uniformity in the cell. The heater filaments at the ends of the lamps are heated to incandescence by six volt filament transformers to facilitate lamp starting and stabilize lamp operating characteristics.

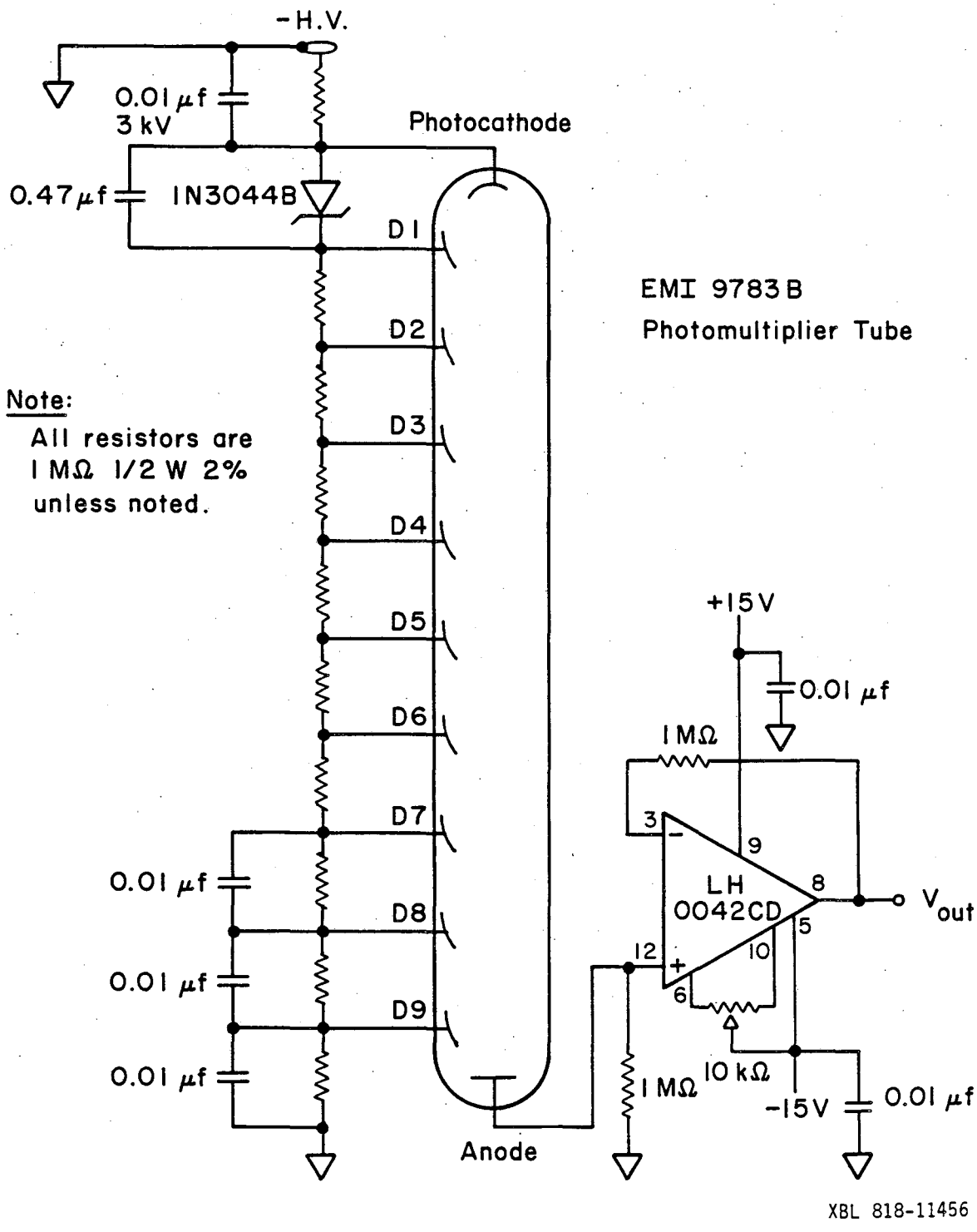

Fig. 4. Photomultiplier dynode string and preamplifier.

The circuit to drive the lamps is shown schematically in Fig. 5. Early experiments with these lamps indicated that above a minimum discharge maintenance current the lamp output was nearly proportional to lamp current. Therefore, by controlling the lamp current with series pass transistors, the lamp current and intensity can be made to follow any programming voltage signal within the circuit's bandwidth. Generally, this consists of a D.C. level set by the D.C. adjustment potentiometer and a variable amplitude sinusoidal modulation signal from the digital sine wave generator (Appendix B).

Photolysis lamp intensity is monitored with an EG and G UV100B ultraviolet enhanced silicon photodiode mounted beneath the front end cap and pointed at the center of the cell. In order to detect just the lamp output which leads to photolysis, a 254 nm interference filter with 15 nm bandwidth and 12 percent peak transmittance is mounted in front of the UV photodiode. A schematic diagram of this monitor is shown in Fig. 6. When the cell is empty the photodiode can be used to measure changes in the lamp output due to aging or temperature change. When there is ozone in the cell, quantifying changes in lamp output is difficult because the light reaching the photodiode comes both directly around the cell and scattered through the cell. A decrease in lamp output causes an increase in steady state ozone which further attenuates the portion of the light coming through the cell. Since the large lamp intensity changes seem to occur as step functions, the main purpose of the monitor in this case is to indicate if an output change has occured in the course of a series of experiments.

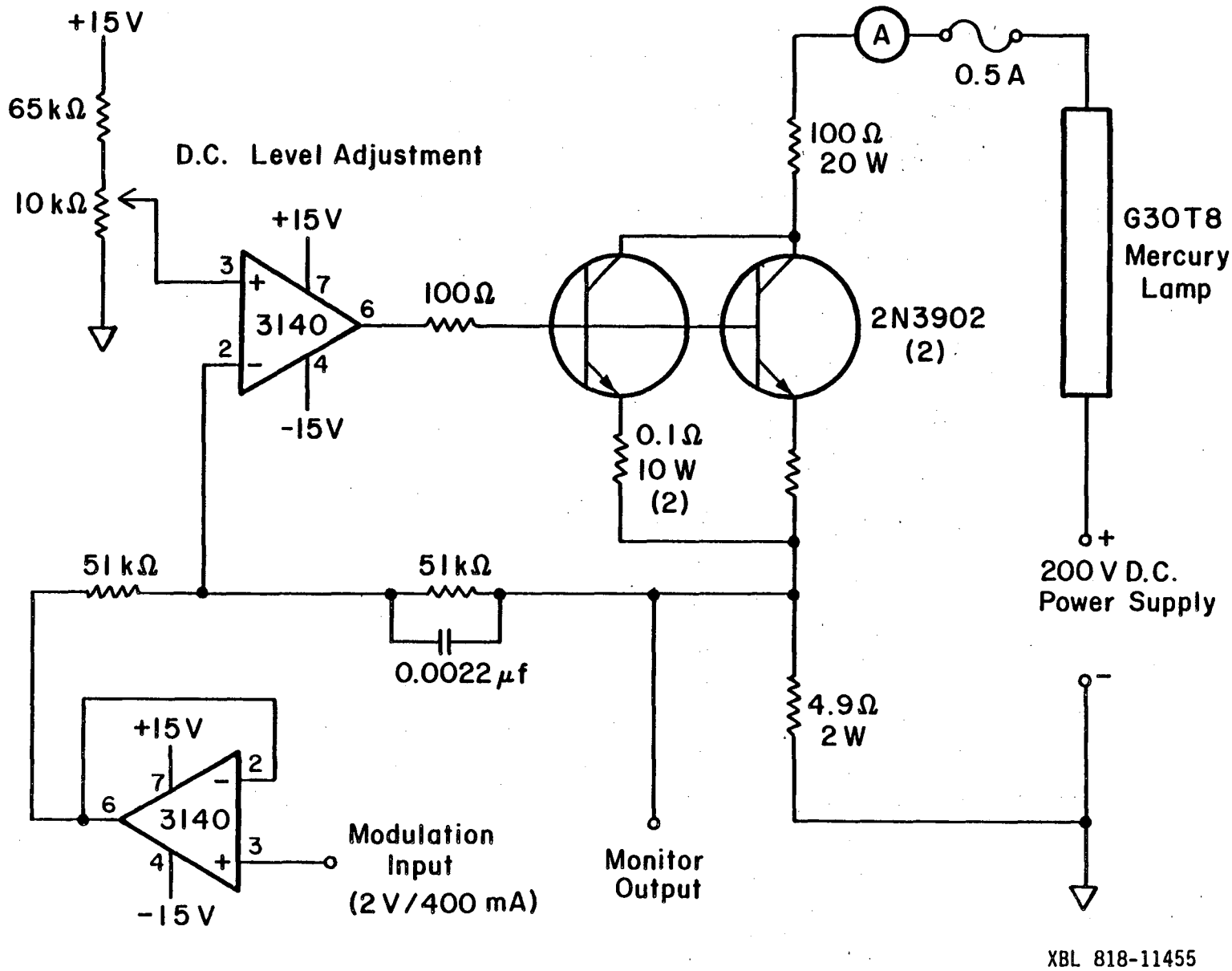

Fig. 5. Photolysis lamp driver circuit schematic.

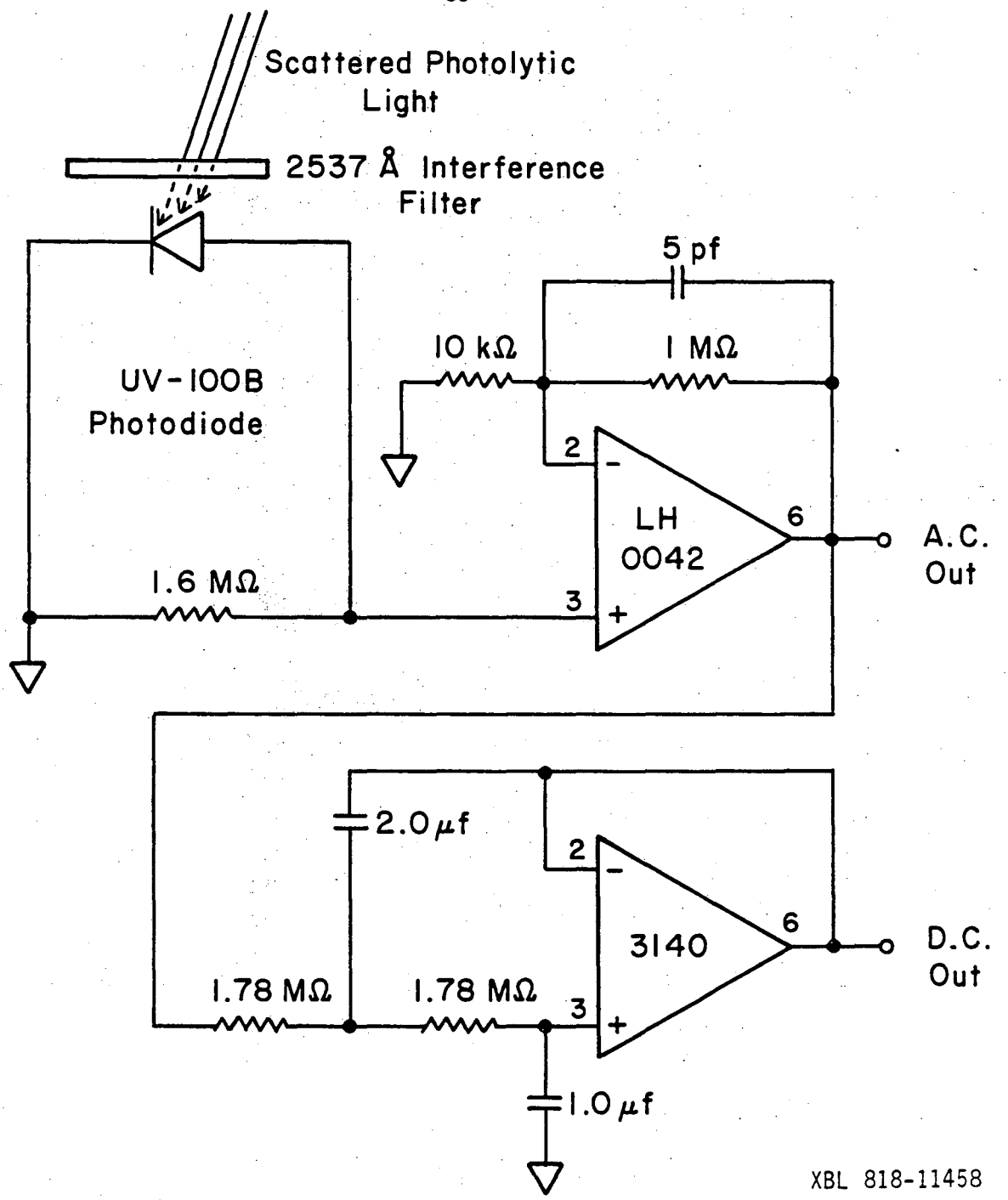

Fig. 6. Photolysis lamp monitor circuit schematic.

4. Detection Electronics. Inspection of Fig. 3 reveals that the spectroscopic probe beam can be modulated three different ways and that these modulations are detected at four different frequencies. The purpose of each is described in the following subsections.

a. Derivative Signals. As described previously, the most sensitive way to detect small absorptions is by observing the first or second derivative of them. That is accomplished by modulating the laser frequency rapidly over a small interval while slowly sweeping it over the frequency range of interest. The derivative profiles are obtained by phase sensitive detection of the laser intensity fluctuations at the modulation frequency as the laser center frequency is swept.

In this system the laser frequency is modulated by a variable amplitude 5 kHz oscillator connected to the current programming input of the Laser Control Module. The laser frequency is slowly swept by the internal ramp generator, which also drives the X axis of the recorder. The laser intensity fluctuations are detected by the InSb detector and sent to two phase sensitive detectors; one set to detect at 5 kHz (first derivative) and one set to detect at 10 kHz (second derivative). The output of either the first or second derivative detector can then be sent to the X-Y recorder. Although not imperative, this type of detection is best done when the other beam modulation sources are not operative.

b. Carrier Signal. The spectroscopic probe beam from the selected source is chopped at 1800 Hz by the tuning fork chopper in

order to move the signal information carried on the beam to a frequency above the region of electronic 1/f noise. Also, the infrared sources must be chopped so that the A.C.-coupled infrared detector preamplifier will respond to them. During a molecular modulation experiment the concentrations in all the species of the reaction cell are being modulated at the flashing frequency, f, of the photolysis lamps. After the probe beam has traversed the reaction cell, it is amplitude modulated at the wavelengths where one or more of the chemical species absorbs. For these wavelengths the resultant detector signal is composed of an 1800 Hz carrier signal, 1800 ± f Hz sideband components which contain the modulation information, and a low frequency f Hz component which arises from the D.C. component of the chopped beam.

The detector signal goes to the 1800 Hz carrier lockin amplifier, which amplifies it, effectively cross multiplies it with a square wave function which is in-phase with the reference signal from the chopper, and filters the result with a time constant of about 1 millisecond (about 2 cycles). This process converts the 1800 Hz carrier to a D.C. level proportional to its original amplitude and converts the sidebands containing the modulation information to an f Hz signal on top of the D.C. level. This resultant signal is split and processed by two separate devices. One device is a two pole low-pass Bessel active filter which cleans up the D.C. component to give a voltage which is proportional to average beam intensity, called either I or I_o depending on cell contents. This voltage is displayed on a digital

voltmeter and recorded either by the X-Y recorder or the data acquisition system. Since this D.C. level must have good long term stability to make accurate absorption measurements, the standard driver electronics for the tuning fork chopper have been replaced with a more sophisticated circuit, described in Appendix C, which results in better chopper and beam amplitude stability. The f Hz modulation is sent on for detection to the second device, a dual phase lockin amplifier described in subsection C.

Both the 1800 Hz carrier and 5/10 kHz derivative lockin amplifiers were constructed in this laboratory from commercially obtained components. They share the same chassis and power supplies, and have equal access to the two 3-1/2 digit DVMs used for signal display. Except for a few components which determine operating frequency, the two channels are identical. The reference signal is processed by an Evans Associates Model 4114 phase control unit, which converts any periodic reference signal into two symmetrical logic waveforms which differ in phase by 90°. The phase of these waveforms with respect to the reference can be changed in steps of 90° as well as continuously over ±100°. In the second harmonic mode the waveform frequency is twice the reference frequency, the outputs differ by 180°, and the controls change the phase by twice the amount as they do in the fundamental mode. The carrier signal is processed in each channel by two Evans Associates Model 4110 phase sensitive detectors, one each to detect the in-phase and quadrature components. They have switch selectable gain and output time constant, optional bandpass filter

(Q = 8), and take their reference from the phase control of their channel. They operate by using the reference logic waveform to determine the instantaneous sign with which they pass the incoming signal to the output lowpass filter; this is referred to as synchronous conversion. An input signal phase-coherent to the reference is therefore added coherently to the output to produce a D.C. signal proportional to the amplitude of the input. Signals at frequencies adjacent to the reference produce a difference frequency output which is attenuated by the post conversion lowpass filter. Measurement of the derivatives requires output time constants of 0.1 to 1.0 second and insertion of the bandpass filter on the input so that incoherent signals do not overload the converter. Modulation experiments require using the minimum output time constant (~1 millisecond) and removing the bandpass filter so that the carrier sidebands are not severely attenuated.

c. Chemical Modulation Signal. The unfiltered output from the 1800 Hz carrier lockin goes to an Ithaco Dynatrac 3 lockin analyzer for detection of the chemical modulation signal. This lockin is superior to those described previously in terms of output stability at lower frequency, harmonic rejection, dynamic range, and range of operating frequency. This is important, as the small modulation signals ($\Delta I/I \simeq 10^{-3}$) are again at low frequency. This lockin amplifier is referenced to the low frequency generator which modulates the photolysis lamps, and measures both the in-phase and quadrature components of the signal simultaneously. These two outputs are

recorded by the data acquisition computer during the course of an experiment for display, storage and later analysis.

Since the carrier lockin affects both the amplitude and phase of the chemical modulation signal, a calibration of this effect is required. The modulation standard circuit, shown in Fig. 7, fills this need. This circuit produces a square wave modulation on the 1800 Hz carrier signal with a phase shift of 0° with respect to the low frequency input and an amplitude set by three precision resistors of $\Delta I/I = 1.003 \times 10^{-3}$. This signal is then processed by the detection electronics and both the final amplitude and phase of the low frequency modulation and the D.C. level out of the carrier lockin are measured. Since the "chemical" lockin responds to RMS signal amplitude, the measured modulation amplitude should be 9.03×10^{-4} times the measured D.C. carrier output. Comparison of this value with the measured amplitude gives the attentuation factor of the carrier lockin at this modulation frequency. The measured phase of the signal gives the phase shift of the carrier lockin at this frequency directly. Consequently experimental modulation signals can be corrected for the carrier lockin transfer function.

5. Data Acquisition System. A schematic diagram of the computer system used for collecting, analyzing and storing experimental data is shown in Fig. 8. Most of this research was performed with a Digital Equipment Corporation PDP 8/E minicomputer having 32K of memory. An analog multiplexer controlled by the computer selects both the signal channel to measure and the gain to use. The output of the multiplexer

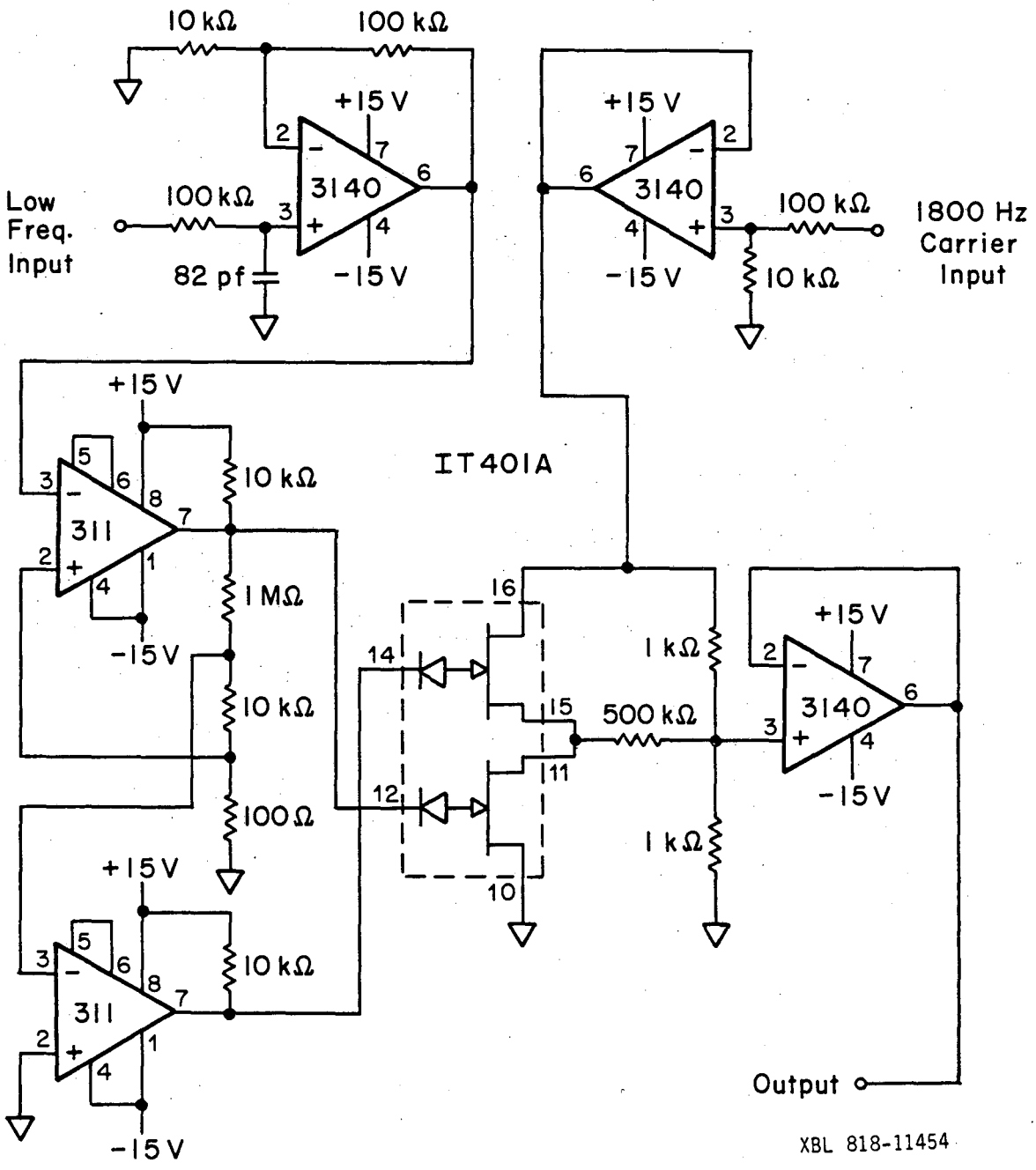

Fig. 7. Modulation standard circuit schematic.

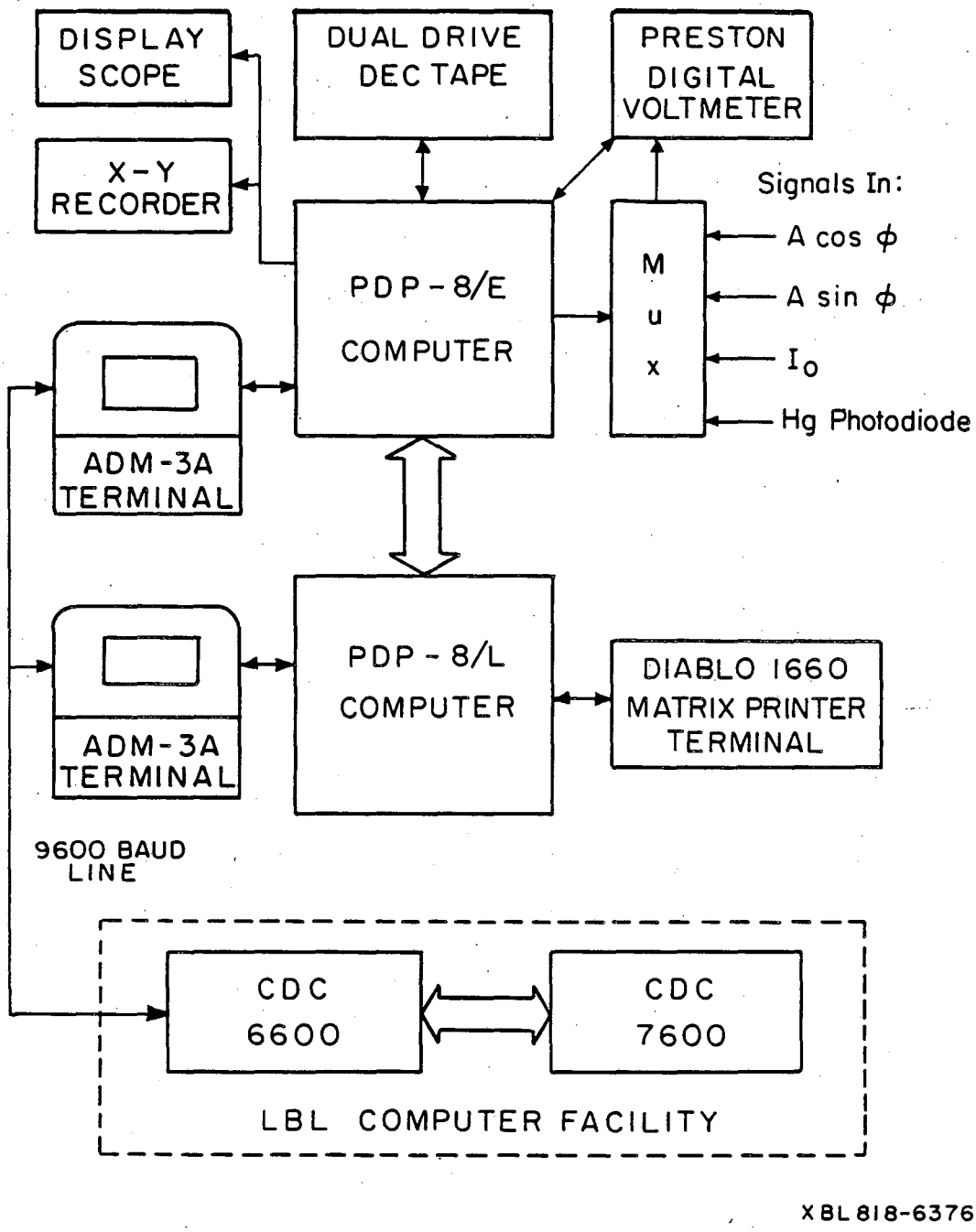

Fig. 8. Schematic diagram of data acquisition computer system.

goes to a Preston X-Mod 723A 4-1/2 digit digital voltmeter, which has a stated accuracy of 1 part in 20,000. A programmable real-time clock internal to the computer controls the rate at which the DVM samples its input, digitizes it, and sends it to the computer for storage in memory. The dual drive Dectape unit interfaced to the PDP 8/E allows storage of programs and data on magnetic tape. A highly modified verison of the interactive language FOCAL developed by Richard Graham[59] allows use of all the above features in an interactive environment, as well as collection of data under interrupt control so that other calculations can be done simultaneously. A display scope allows real-time viewing of the data as they are collected, and an X-Y recorder plots out the final results. An interface to the PDP 8/L minicomputer provides high speed printed output capability on the Diablo Model 1660 matrix printer terminal.

Direct computer-computer communication between the laboratory system and the Lawrence Berkeley Laboratory computer complex is possible via a 9600 baud dedicated line between the two sites. In one mode printer output is sent from LBL through the ADM-3A terminal to the PDP 8/E computer, which acts as a storage buffer and implements the required software "handshake" signals. The 8/E then asynchronously sends the output to the 8/L, and from there is sent to the Diablo printer. In the other mode, laboratory data is sent from the 8/E to the 8/L, which buffers the data flow and implements a software version of "X-on:X-off" control with LBL. The 8/L then sends the data through the ADM-3A terminal to either a CDC 6600 or CDC 6400 computer

at LBL for storage and analysis. This system thus provides both dedicated real time data acquisition capability and large mainframe computational power.

C. Gases and Flow System

All of the gases used in this study were supplied by the Lawrence Berkeley Laboratory. The suppliers' specifications for maximum impurity concentrations in these gases are listed in Table 1. Extra pure helium was flowed through a Matheson moisture and particulate filter, and optionally through a 6 to 12 mesh silica gel trap at liquid nitrogen temperature, prior to use as a carrier gas. Distilled water of 99.9 percent purity was stored in a glass saturator and vacuum degassed to remove any volatile impurities. Ozone was prepared from high dry oxygen, which was purified by passing through a quartz tube containing copper turnings at 900 K to oxidize hydrocarbon impurities to CO_2 and H_2O, through a column containing pellets of 5 percent palladium on alumina heated to 620 K to oxidize hydrogen, and finally through columns of ascarite and P_2O_5 on glass beads to remove the CO_2 and H_2O, respectively. The purified oxygen went through an Ozone Research and Equipment Company ozonator, which converts approximately 5 percent of the oxygen to ozone. From there it passed through a high capacity glass trap containing 6 to 12 mesh silica gel held at 196 K by a dry-ice isopropanol slush bath to collect the ozone. To further purify the ozone, helium is flowed through the trap at 68 Torr with a flow rate of 3.7 standard liters/min to remove residual oxygen. At dry ice temperature the partial pressure of ozone is about 10 Torr.

Table 1
Typical Gas Impurity Levels[a]

	High Dry Oxygen	Extra Pure Helium
N_2	400 ppm	5.0 ppm
O_2	99.6 pct min	5.0 ppm
He	---	99.995 pct min
H_2O	1.5 ppm	1.5 ppm
CO_2	10 ppm	0.1 ppm
Ar	3000 ppm	0.1 ppm
Ne	---	14 ppm
THC[b]	12.5 ppm	1 ppm

[a] As quoted by supplier

[b] Total hydrocarbons as CH_4

A complete discussion of separation of ozone from oxygen by absorption on silica gel and the precautions required has been presented by Cook.[60]

The manifold for preparing the gas mixtures was constructed using Pyrex tubing. All the stopcocks were Kontes 0-4 mm high vacuum stopcocks with teflon bores and Viton O-rings. Connections between different sections of the manifold were made with stainless steel Cajon Ultra-Torr fittings. The helium carrier gas first passed through a Manostat Predictability flowmeter to measure total gas flow rate. Calibration of this flowmeter by timing the period for a gas flow from it to fill a calibrated volume agreed very well with the calibration predicted from the flowmeter literature formulas. The carrier stream was then split into three parallel flow circuits, each one with either a size S or M Nupro stainless steel needle valve at the upstream end to drop the pressure and regulate the carrier flow through the circuit. Each circuit has a saturator which is either in series with the flow or bypassed, controlled by a set of three stopcocks. One saturator is for ozone as described earlier, another contains H_2O and the third contains H_2O_2. This allowed independent adjustment of the H_2O and O_3 concentrations entering the cell. The ozone saturator is kept at 196 K with a dry ice-isopropanol slush. The other two saturators are mounted in 4 liter dewars containing 1:1 ethylene glycol/water solution which is cooled by a coil in the bottom of the dewar through which methanol at 0°C is flowed from a Neslab RTE 4 refrigerator. The solution temperatures are controlled by proportional controllers which

drive heater coils mounted next to the cooling coils. Uniform temperature is achieved by bubbling air through the solution from a disperser tube underneath the coils to obtain mixing, and measured with an alcohol thermometer.

The gases enter and exit the cell through two identical disperser tubes running along the top and bottom of the cell. They are 3/8" thin wall pyrex tubes with 1 cm long stainless steel capillary tubes protruding through the side every 3". Since the pressure drop across the capillary is at least 10 times the pressure drop along the length of the tube, uniform chemical flow in and out of the cell is assured. Also, the turbulence caused by the flow in process keeps the reaction cell contents well mixed. Exhaust gas passes through 6 feet of 3/4" copper tube heated to 100° C to destroy most of the remaining ozone, through a liquid nitrogen cooled trap to collect the residual O_3 and H_2O, and then to a Kinney KC-5 mechanical pump. With a helium flow rate of 3.66 standard liters/min through the system, the pump maintains the cell pressure at 68 Torr.

III. EXPERIMENTAL PROCEDURE AND DATA

A. Ultraviolet Absorption Cross Sections

Ultraviolet absorption cross sections are required in this study for modeling the photolytic decomposition mechanisms as well as for monitoring O_3 concentration. At the photolysis wavelength of 2537 Å, both O_3 and H_2O_2 are known to absorb radiation and dissociate, and their absorption spectra have been measured previously.[61-64] The spectra of these two molecules are shown in Fig. 9. The only other species which absorbs near this wavelength is HO_2, whose UV spectrum has a maximum at 2100 Å and a weak tail extending into the photolysis wavelength region.[49,65,66] Photolysis products for HO_2 have never been measured, but have been predicted in a theoretical investigation to be O + OH.[67] Since the chemical destruction rate for HO_2 is calculated to be over two orders of magnitude larger than the photolytic rate, photolysis of this species can be ignored. At the monitoring wavelength of 3150 Å, again only O_3 and H_2O_2 absorb. Since the value of the H_2O_2 cross section is only 5 percent of that for O_3 and the H_2O_2 concentration is at least two orders of magnitude smaller than the O_3 concentration, H_2O_2 never interferes with the measurement of O_3 concentration by UV absorption at 3150 Å.

The choice of 3150 Å as the monitoring wavelength for O_3 was determined by consideration of the accuracy of concentration measurement by absorption as a function of transmittance. The optimum accuracy is obtained when T = 37 percent, and degrades by a factor of

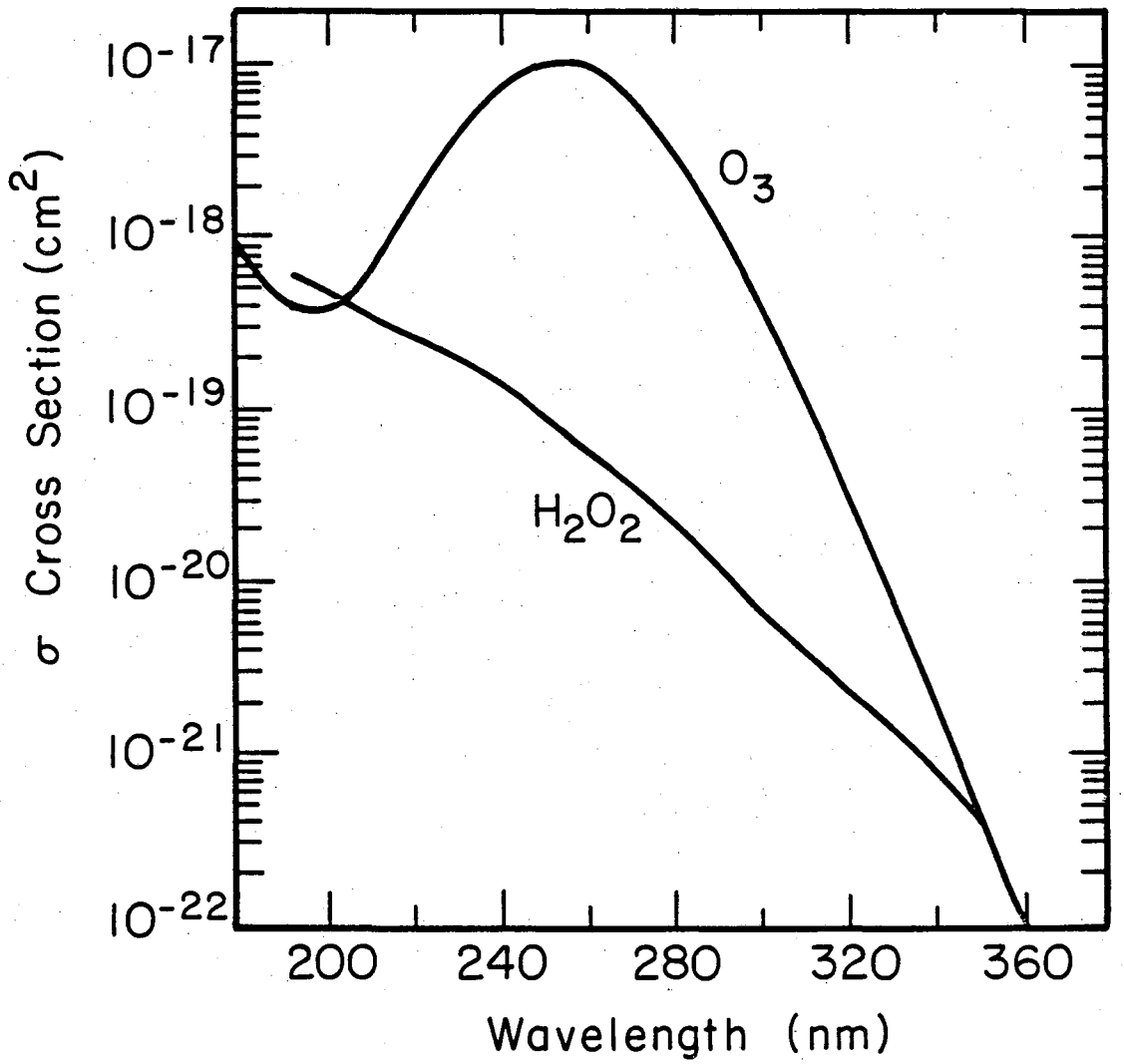

Fig. 9. Ultraviolet absorption spectra of O_3 and H_2O_2.

two at T = 6 percent and T = 80 percent (see reference 68, Table 4-4). For the O_3 concentrations anticipated (1.5 - 15 x 10^{15} molecules/cm^3) and the pathlength used (2962 cm), keeping the transmittance in the 6-80 percent range required that the cross section be 5 x 10^{-20} cm^2/molecule, which is the value for O_3 at 3150 Å. The problem with using this wavelength is that the O_3 spectrum is structured in this region, so that wavelength calibration errors and differences in spectral resolution from earlier cross section measurements may mean use of their results in this study is inappropriate. Also the table of published absorption coefficients[69] uses irregular wavelength intervals, so a listing at every 1 Å is useful. Since the spectrum of O_3 at 3100 Å does not exhibit the same bothersome features as it does at 3150 Å, the previous result at 3100 Å was used to measure absolute O_3 concentration in this investigation.

The reaction cell and optical train described earlier were used as a single beam spectrometer for the measurement of the O_3 absorption cross sections. The D_2 lamp provided the required ultraviolet radiation, which made 16 passes through the cell to give a total absorption pathlength of 2962 cm. The monochromator was operated with the 1200 line/mm grating, and entrance and exit slits set at 200 microns, to give a spectral resolution (full width at half maximum) of 1.67 Å. The EMI 9783B PMT detected the probe beam, and its output went to the 1800 Hz lockin for demodulation. The demodulator was operated with a preconversion gain of ten and a 0.5 second output time constant. The results were recorded by the PDP 8/E at 0.3 seconds/point in sets of 1024 points. The monochromator wavelength readout

was calibrated with the 2536.5, 3125.7 and 3131.7 Å Hg lines which are produced by the photolysis lamps and get scattered into the optical path. Cell temperature was 293 K throughout the measurement.

Helium was flowed through the cell at 3.66 standard liters/minute at a pressure of 67.6 Torr. Incident beam intensity $I_0(\lambda)$ was measured both with wavelength fixed at 3100 Å and while the wavelength was scanned from 3100 to 3203.3 Å at a rate of 20 Å/minute. Next, O_3 was added to the flow stream from the saturator and the flows adjusted until its steady state concentration was about 3×10^{15} molecules/cm^3. The transmitted beam intensity $I(\lambda)$ was then recorded for 5 minutes at 3100 Å, recorded again as the wavelength was scanned from 3100 to 3203.3 Å, and again for 5 minutes at 3100 Å. Analysis of the results at 3100 Å indicated that the steady state concentration of ozone was increasing with time as the ozone absorbed on the silica gel migrated toward the saturator exit. The two data sets of I(3100), when converted to optical density, were found to be accurately described by:

$$O.D. = 1.18021 - .28363\ e^{-(3.1598E-4)t} \qquad (49)$$

where t is time in seconds starting at the time the first I(3100) data point was recorded. This expression, combined with the value of $\sigma(3100) = 1.028 \times 10^{-19}$ cm^2/molecule derived from reference 69 and the pathlength $l = 2962$ cm, allowed calculation of the O_3 concentration at the exact time each $I(\lambda)$ data point was recorded, called for

convenience $O_3(\lambda)$. The absorption cross section σ at each wavelength was then calculated from the expression:

$$\sigma(\lambda) = [O_3(\lambda)l]^{-1} \log_e(I_o(\lambda)/I(\lambda)] \quad . \tag{50}$$

The resultant spectrum is shown in Fig. 10, along with the values measured by Inn and Tanaka.[69] The agreement is very good, especially near 3150 Å. Table 2 lists the measured cross sections at every 1 Å from 3100 to 3201 Å.

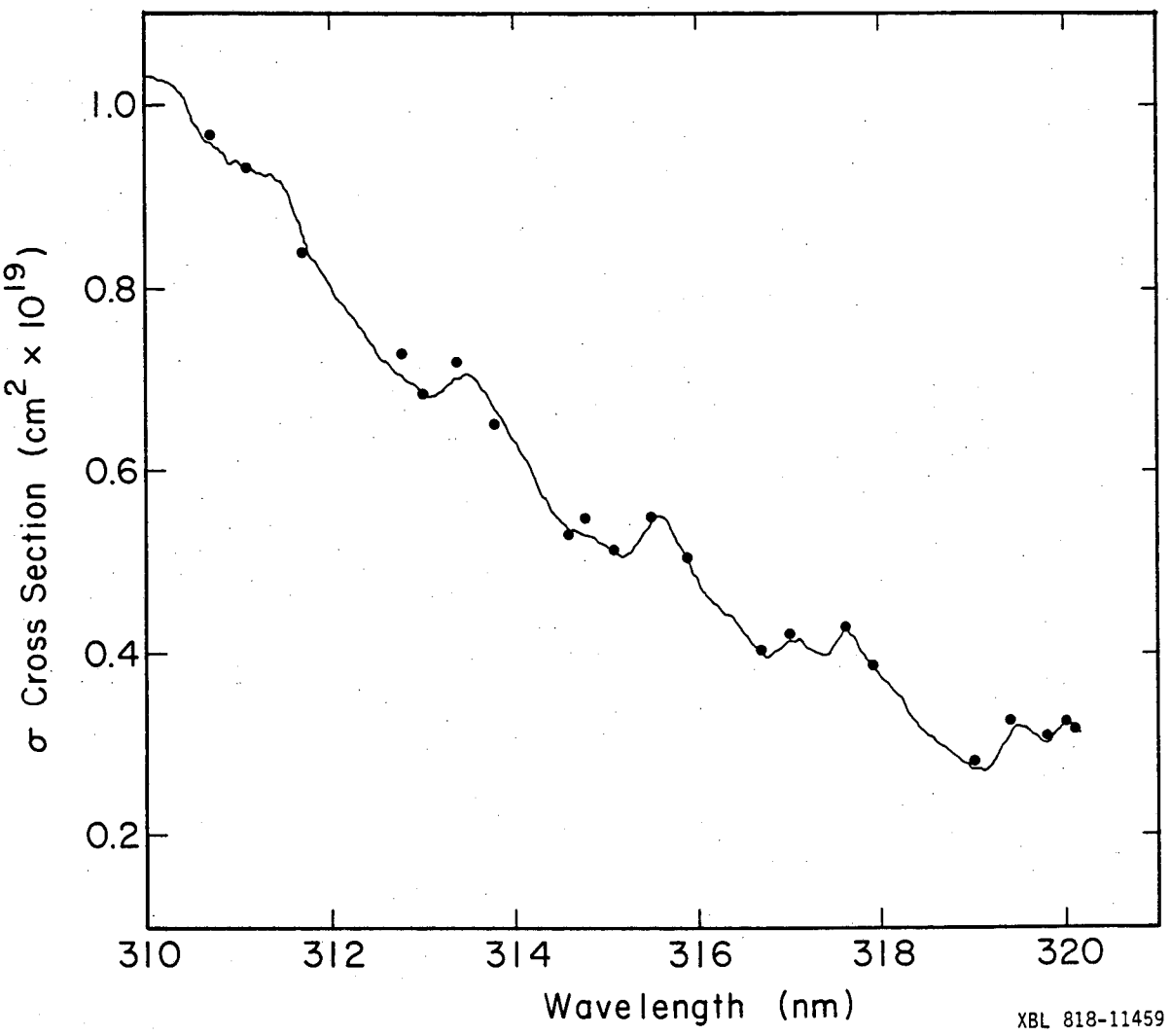

Fig. 10. Ultraviolet absorption spectrum of O_3 in the Huggins band region (solid line is the result of this study, dots are from ref. 69).

Table 2
Absorption cross sections (cm^2/molecule, base e) for ozone averaged over each Å.

λ(Å)	$10^{20}\sigma$	λ(Å)	$10^{20}\sigma$	λ(Å	$10^{20}\sigma$
3100	10.31	3134	7.02	3168	3.97
3101	10.28	3135	7.06	3169	4.05
3102	10.26	3136	7.00	3170	4.13
3103	10.22	3137	6.86	3171	4.15
3104	10.10	3138	6.70	3172	4.09
3105	9.89	3139	6.55	3173	4.03
3106	9.70	3140	6.36	3174	4.00
3107	9.57	3141	6.20	3175	4.09
3108	9.51	3142	6.01	3176	4.24
3109	9.40	3143	5.78	3177	4.20
3110	9.37	3144	5.63	3178	4.05
3111	9.31	3145	5.49	3179	3.90
3112	9.26	3146	5.41	3180	3.77
3113	9.22	3147	5.36	3181	3.67
3114	9.21	3148	5.30	3182	3.55
3115	9.13	3149	5.27	3183	3.40
3116	8.94	3150	5.20	3184	3.24
3117	8.67	3151	5.12	3185	3.13
3118	8.38	3152	5.08	3186	3.06
3119	8.23	3153	5.14	3187	2.97
3120	8.06	3154	5.27	3188	2.91
3121	7.89	3155	5.43	3189	2.82
3122	7.77	3156	5.51	3190	2.75
3123	7.64	3157	5.43	3191	2.72
3124	7.51	3158	5.23	3192	2.77
3125	7.36	3159	5.04	3193	2.93
3126	7.21	3160	4.83	3194	3.09
3127	7.12	3161	4.67	3195	3.21
3128	7.04	3162	4.57	3196	3.17
3129	6.97	3163	4.47	3197	3.08
3130	6.91	3164	4.40	3198	3.02
3131	6.82	3165	4.26	3199	3.12
3132	6.85	3166	4.14	3200	3.22
3133	6.95	3167	4.04	3201	3.20

III. EXPERIMENTAL PROCEDURE AND DATA

B. Laser Mode Selection

At any given operating temperature and current, the output from a laser diode generally consists of several different frequencies, or modes, each one with a bandwidth of ~3 x 10^{-4} cm^{-1} (10 MHz), spaced about 1-2 cm^{-1} apart. Because of this a monochromator is required to select just the one mode desired. The monochormator produces several undesirable effects, including sloping baselines in direct absorption studies and large baseline amplitudes in derivative studies, because of its slit function. Lasers operating in the 4-12 micron region usually have some operating region where they will either emit single-mode[43] or with at least 95 percent of their output power in one mode[45] and so can be used without a monochromator in the optical train. In the 3-4 micron region, however, laser diodes are notoriously bad as far as mode characteristics,[70] and this diode proved no exception. Therefore a mode selection monochromator was used at all times in this study.

The first step in finding diode operating conditions which give a desired output frequency is to determine the section of temperature and current "operating space" for which the diode emits. The monochromator is set to zeroth order to pass all radiation, the temperature is set to the minimum the refrigerator is capable of, and the diode current is then scanned upward by the LCM ramp generator and the detector/demodulator output simultaneously recorded on the X-Y recorder. The scan proceeds in steps of ~0.2 A, the maximum range of

the ramp generator, until the specified maximum allowable diode current is reached. The temperature is then increased by 1 or 2 K, and the current scan from threshold to maximum repeated. Steps in temperature continue upward until no emission is detected at any current. For the particular diode used, the threshold current increased with temperature.

The next step is to determine which regions of "operating space" produced a desired frequency. The manufacturer's test results give the frequency range over which the diode has been observed to emit, so determination of the wavelength region to search is straightforward. The diode temperature is set to the minimum at which laser action was previously observed, and the current to the minimum which produces emission at this temperature. Holding these fixed, the monochromator is scanned over the wavelength region where laser output is expected and the resulting mode spectrum recorded. The monochromator slits are adjusted if necessary so that each mode is resolved (i.e., the signal goes almost to zero between peaks). Now the current is set to the maximum at which emission was observed at this temperature and the wavelength again scanned. This is repeated for the minimum and maximum currents at every temperature investigated previously. Inspection of these results reveal over what temperature range a particular wavelength will be emitted, and for any temperature in that range the approximate current range as well. Two typical mode spectra are shown in Fig. 11 for a diode temperature of 17.0 K and diode currents of 1.150 and 1.750 A. This shows both the complexity of the mode

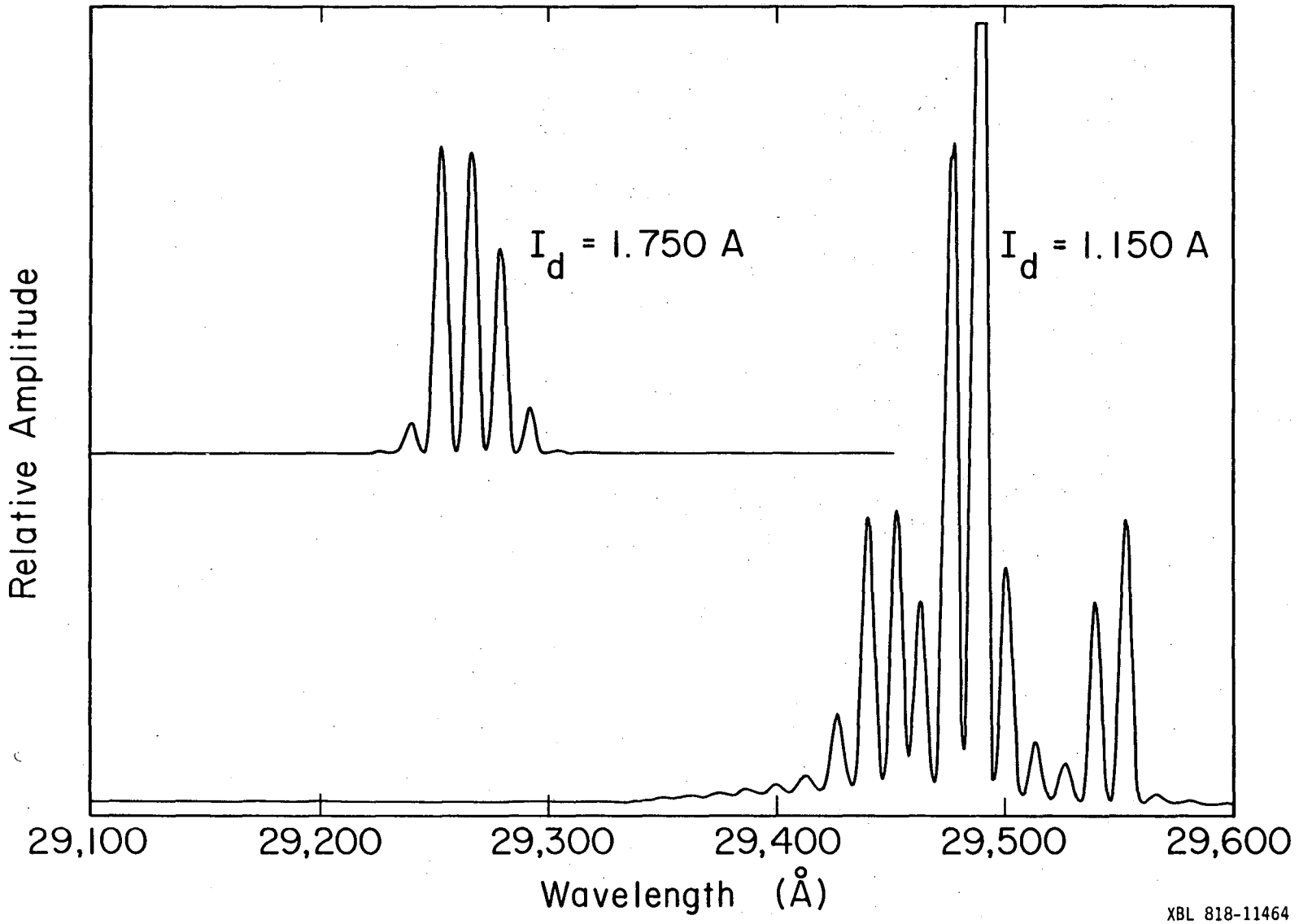

Fig. 11. Observed diode output mode structure for operation at fixed diode temperature T_d=17.0 K and diode currents I_d=1.15A and 1.75A.

structure and the characteristic decrease in laser wavelength (increase in frequency) with increasing laser current. This is the same behavior that is observed with increasing temperature.

To select a mode for a particular frequency, the monochromator is first set to the corresponding wavelength. To insure wavelength accuracy, eight Ne lines between 7000 and 7500 Å were observed in fourth order with the monochromator to check the readout calibration between 28,000 and 30,000 Å. The diode temperature is set to the middle of the range determined for this wavelength, and the current is scanned over its entire range. During the scan the result is recorded on the X-Y recorder and the "raw" detector signal is observed on an oscilloscope which is sweep triggered by the tuning fork chopper reference signal. Observation of the current range where emission occurred at this temperature helps narrow down the range to search at the next temperature, as the limits of this range decrease slowly and predictably with increasing temperature. The recorded spectrum shows whether or not the modes are being resolved, and whether obvious mode breaks (sudden large step function changes in intensity with laser current) are occurring for a particular mode. Observation of the oscilloscope trace as a mode is being scanned reveals whether it has undesirable high frequency intensity oscillations, usually characterized by a low average signal with large narrow spikes on top of it. If a mode passes these two tests, it is marked down for later consideration. The temperature is now increased about 1 K and the current scan repeated, usually over a reduced range. The temperature

is incrementally increased until no more laser output is observed at this wavelength. The temperature is then reset to just below the first temperature investigated and temperature incremented downward until laser output again vanishes. This process uncovers all possible "good" laser modes for this wavelength. If many good, strong modes are found initially, covering this entire temperature range is not necessary. Figure 12 shows a typical diode tuning curve; diode temperature is 18.2 K, monochromator is set at 29,215 Å (3432 cm^{-1}), and slits are 200 microns (6.66 Å/0.78 cm^{-1} FWHM). Varying the current from 1.80 to 2.00 A tunes three separate modes through the monochromator's bandpass, with each one resolved from the next. If H_2O absorptions A and B were not present, the nearly triangular slit function of the monochromator would be observed. Since the mode at 1.90 A is strongest, it was chosen for later studies in the 3422 cm^{-1} region.

Subtle mode breaks and hops can be detected several ways. One way is observation of the trace produced when a mode is scanned with the etalon in the beam. The resulting etalon trace should be a smooth curve with no discontinuities, roughly sinusoidal but with sharper peaks and broader valleys, and even spacing between peaks. An example of a good trace is shown in the next section, Fig. 13. Another method to detect subtle mode breaks is observation of the derivative signal. Generally each mode tunes at a slightly different rate ($d\nu/dI$), so if one mode starts up at the expense of another while total intensity is nearly constant, a discontinuity in the first derivative will still be observed. An example of a good first derivative trace is shown in Fig. 14.

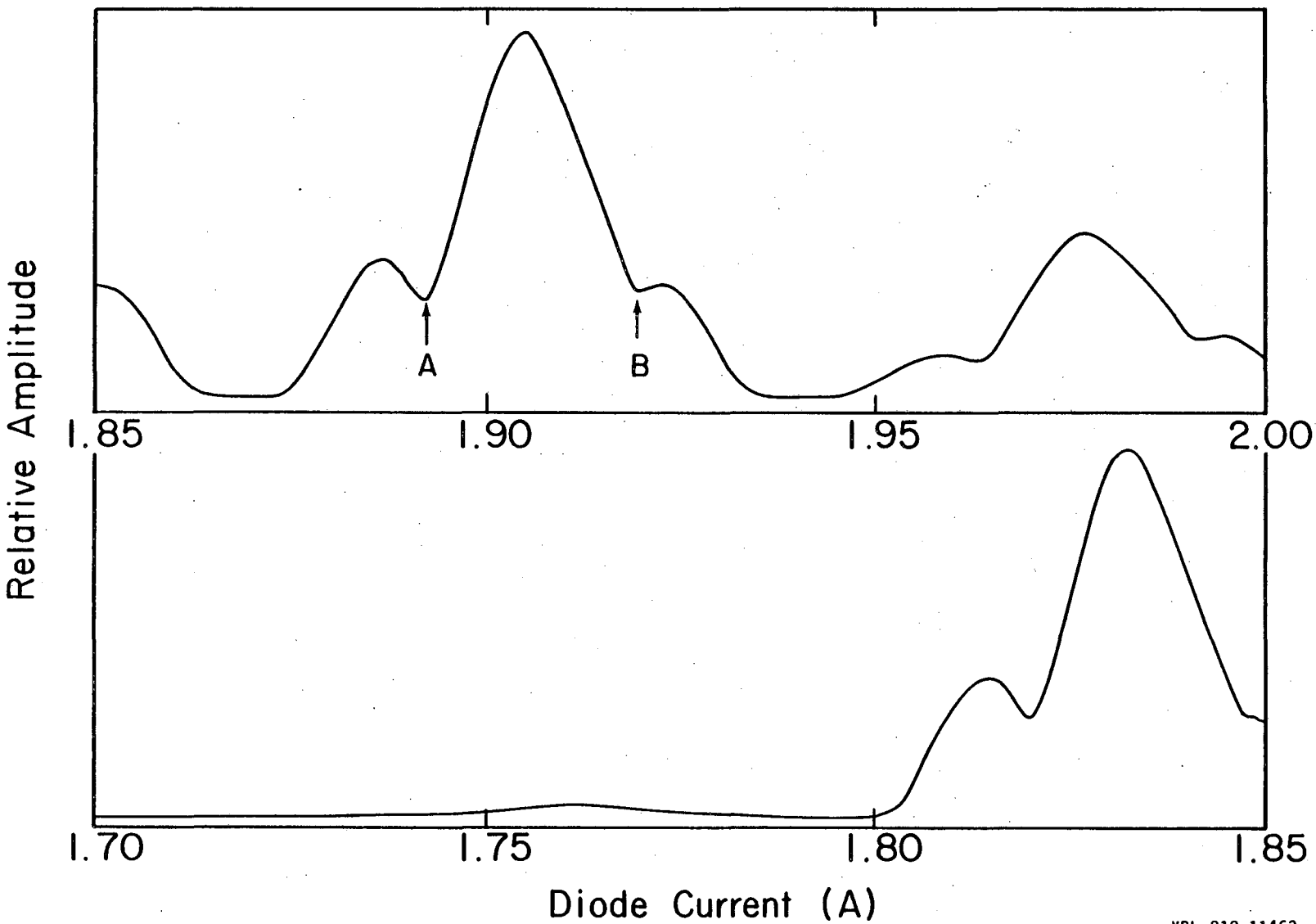

XBL 818-11463

Fig. 12. Diode tuning curve at T_d = 18.2 K for λ = 29,215Å (ν = 3422 cm^{-1})
Peak A = 3421.739 cm^{-1} H_2O line
Peak B = 3422.333/3422.369 cm^{-1} H_2O lines

As an added complication, after three to five weeks of low temperature operation enough oxygen, nitrogen and water vapor leak into the vacuum dewar and condense on the diode to impair its performance. The diode assembly must then be brought up to room temperature and the vacuum jacket pumped down to 10^{-2} Torr or better. When the diode is again recooled, the mode behavior has generally shifted, so at least part of the process described above must be repeated. As a result of this, a large portion of the effort to measure hydroxyl radical absorptions was expended in laser mode selection.

C. H_2O Determination

Both the HO_2-$O_2(^1\Delta)$ study and the OH absorption study required quantitative knowledge of the water vapor concentration in order to model the chemical system. The decision on exactly what H_2O concentration to use was based on several considerations:

1) H_2O must effectively compete with O_3 for the $O(^1D)$ produced in the photolysis of O_3,
2) high H_2O concentrations require complete modeling of the water dependence of the $HO_2 + HO_2$ disproportionation reaction,
3) water vapor condenses in the liquid nitrogen trap in front of the mechanical pump and forms a fluffy ice plug which eventually limits the conductance of the pumping system.

After careful consideration and experimentation it was decided that 2 Torr of H_2O would be optimal. This H_2O concentration results in

>85 percent of the $O(^1D)$ reacting with water under all conditions explored in the HO_2-$O_2(^1\Delta)$ study and >95 percent reacting under the conditions of the OH absorption study. Interpretation of the results of Hamilton and Lii[71] on the water dependence of the HO_2 disproportionation rate constant indicates it should only be a 20 percent effect with 2 Torr of water present, which is within the experimental uncertainty of the measured dry rate constant. Therefore, this effect does not need to be considered in detail. Experimentation with the ice plug problem showed that with an H_2O steady state pressure of 2 Torr, the trap could go 30–40 minutes before cell pressure started to increase due to severely reduced conductance of the trap. During the HO_2-$O_2(^1\Delta)$ experiment series this meant the flow had to be stopped halfway through and the trap cleared. For the OH absorption study the trap was reversed, so that the ice formed on the large diameter outer tube of the trap rather than inside the smaller inner tube, and in this configuration maximum flow time was never reached.

As described earlier, the flow manifold contained a section with three parallel flow circuits for independent adjustment of O_3, H_2O and total flow rate. Throughout these studies the total carrier gas flow rate was kept constant at 3.66 standard liters/minute. When the flow rate through the H_2O saturator bypass circuit was 0.80 liters/minute and the saturator bath was controlled at 293.0 K, diverting the flow through the saturator resulted in the cell pressure increasing by 2.1 Torr, which was due to the H_2O partial pressure.

Since this was a very reproducible change, this saturator temperature and flow rate were settled on as the standard conditions and used throughout the OH absorption study and half the HO_2-$O_2(^1\Delta)$ study.

To accurately measure the H_2O concentration under the standard flow conditions, high resolution spectroscopy with the diode laser was employed. Early observation of H_2O lines indicated that their linewidths were generally 1.5 times their doppler width of 0.010 cm^{-1}. To get a peak absorption of about 50 percent required an H_2O absorption with a line intensity of 7×10^{-23} cm/molecule. A search of the best compilation to date of calculated H_2O vibration-rotation line parameters[72] uncovered a ν_1 transition at 3406.675 cm^{-1} with the right intensity and for which the intensity had been experimentally determined previously.[73] The monochromator was set as closely as possible to the wavelength corresponding to the line, and a good laser mode located, as described earlier. Water was flowed into the cell under standard conditions, and the monochromator setting finely tuned until the nearly flat top of the slit function was centered on the H_2O line. The laser was then scanned over the absorption line two separate times and the absorption profiles recorded on the X-Y recorder. The cell was then pumped out and an etalon trace made for frequency calibration. These traces are shown in Fig. 13. Values of I and I_o were read off the graph paper for each small division and converted to optical density. The frequency spacing between these points was calculated by comparison with the spacing of the etalon fringes on the graph paper, since the fringes

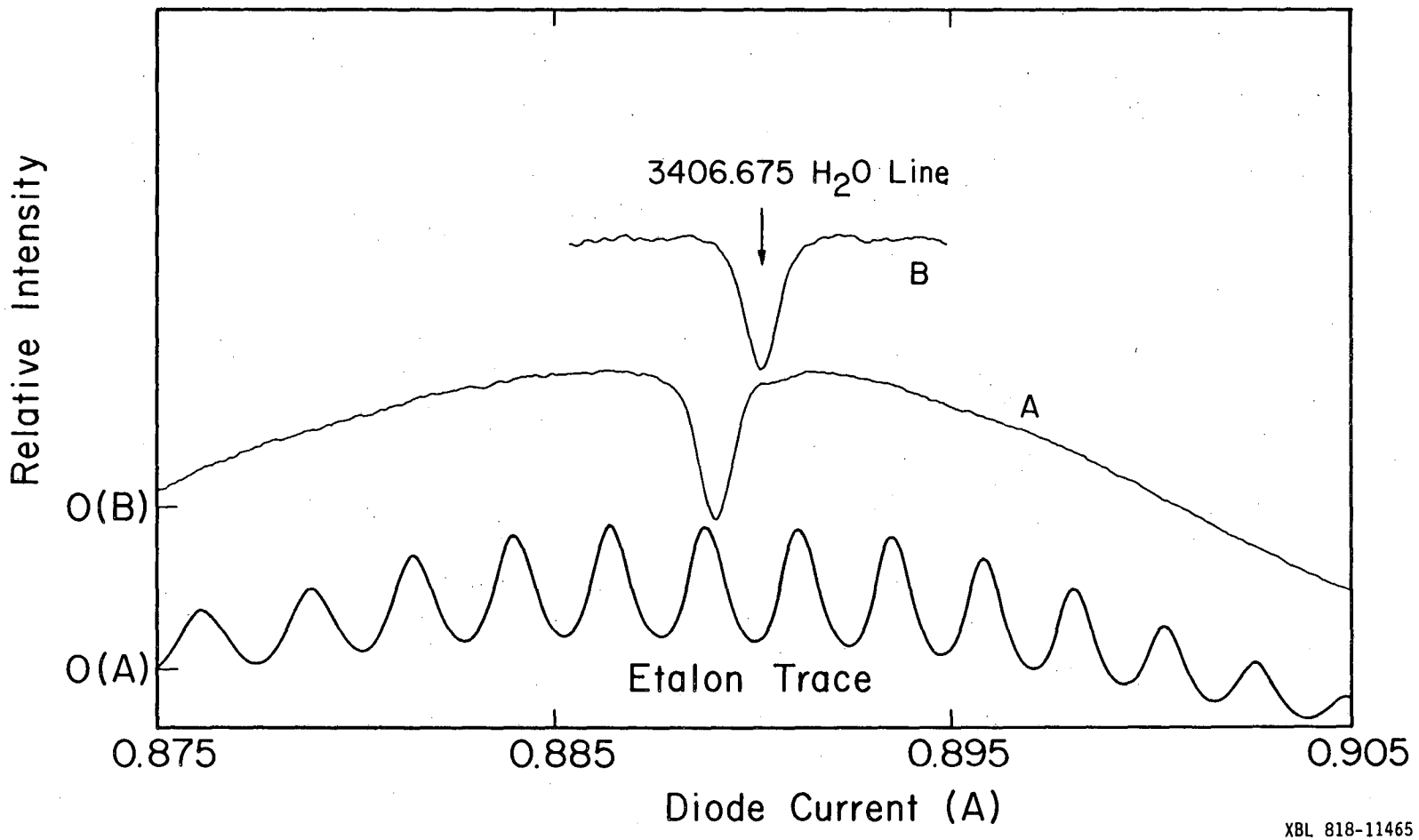

Fig. 13. Absorption profile measurements of the 3406.675 cm^{-1} H_2O transition. Trace A is the result of the first (broad) scan over the H_2O line. Trace B is the result of the second (narrow) scan over the H_2O line. (Note the separate baseline for the two scans).

are known to be 0.0486 cm^{-1} apart. Each optical density profile was then numerically integrated to yield an average integrated optical density of 0.0139 cm^{-1}. This was converted to H_2O concentration by the relation:

$$n_{H_2O} = \frac{\int_{line} O.D.(\nu)d\nu}{lS} \tag{51}$$

where n_{H_2O} is the number density of water molecules, l is the absorption pathlength (2962 cm) and S is the line intensity for this transition (6.90×10^{-23} cm/molecule). The water concentration is 6.80×10^{16} molecules/cm^3, which at 293 K corresponds to 2.06 Torr. This is in very good agreement with the pressure rises observed upon addition of H_2O to the carrier stream, which were always between 2.0 and 2.1 Torr.

The HO_2-$O_2(^1\Delta)$ study required a second water concentration about one tenth the standard one in order to vary HO_2 concentration at fixed photolysis intensity. This was achieved by using the calibrated flowmeter to change the flow through the H_2O saturator from 0.800 to 0.080 liters/minute while keeping total flow constant. Cell pressure rise was measured with the Baratron gauge at maximum resolution and found to be 0.21 Torr. For standard flow conditions the high resolution pressure measurements gave 2.07 Torr. While the gauge is not as accurate as the resolution here, the relative pressure measurements are probably good to ±10 percent. Thus, in the HO_2-$O_2(^1\Delta)$ experiment analysis the low water concentration was taken to be 6.8×10^{15} molecules/cm^3.

D. Steady State Photolysis of O_3-H_2O

A series of measurements of the change in steady state ozone upon addition of water to a UV irradiated ozone system were made, under varying UV intensities and H_2O concentrations, in order to determine the HO_2-$O_2(^1\Delta)$ quenching rate constant. The reaction cell and optical train described in Section II-B and shown in Fig. 3 were employed, using the D_2 lamp as the probe beam source and a 2962 cm cell pathlength. The 1200 line/mm grating was installed in the monochromator, which was set to 3150 Å with 1.67 Å resolution. The output of the 9783B PMT went to the 1800 Hz carrier lockin, and the lockin's filtered output (0.3 second time constant) was sent to the data acquisition computer, which sampled it every 147 milliseconds in sets of 1024 or 2048 points. This is nearly identical to the setup used to measure O_3 cross sections.

The total flow rate of the helium carrier gas was 3.66 standard liters/minute throughout the experiment. The helium flow rate was kept at 0.28 liters/minute through the ozone saturator and either 0.80 or 0.08 liters/minute through the H_2O saturator. With the H_2O saturator at 293.0 K, these two flow rates gave the "standard" and "low" water concentrations (68 and 6.8 x 10^{15} molecules/cm^3), respectively, as discussed in Section III-C. The O_3 concentration in the absence of photolysis was between 1.0-1.5 x 10^{16} molecules/cm^3. Total pressure with just helium was 67.5 Torr.

Measurements of incident beam intensity $I_o(3150)$ were made several times at the beginning of the series, about midway through,

and after completion, so that its value at intermediate times could be interpolated. The measurements were all made with the carrier gas flowing. Several measurements were made with low and standard water concentrations present, as I_o increases 1.4 percent and 1.8 percent, respectively, over the dry value under these conditions, presumably due to formation of a water layer on the windows and mirrors which reduces scattering of light out of the beam. Also, profiles were recorded of I_o changing as the water was first turned on and first turned off, to correct for this effect in the O_3 observations described later.

The experimental series consisted of ten experiments; five different light intensities and two water concentrations at each intensity. The range of light intensities ($2.5\text{-}15 \times 10^{14}$ photons/cm^2 sec) had been chosen earlier to maximize sensitivity to the effect of $HO_2\text{-}O_2(^1\Delta)$ quenching on the system, and span roughly a factor of 5 range. These intensities were achieved by setting the Hg lamp currents at 4, 8, 12, 16, or 20 milliamperes, and will be referred to for convenience as intensity 1 to 5. Actual photon flux at each intensity was determined by dry O_3 actinometry.

Each experiment consisted of the following sequence of measurements. Photolysis lamps are adjusted to the desired intensity, and when O_3 steady state is achieved its concentration was measured. Another measurement sequence was then started, and after about 15 seconds the helium flow through the H_2O flow circuit bypass was diverted through the saturator, and the O_3 transient observed as

conditions went from dry to wet steady state. A third sequence measured about 15 seconds of the wet O_3, and then the water saturator was bypassed again and O_3 observed as the cell dried out. After the cell was completely dry, the O_3 steady state concentration was again measured. For each intensity the two experiments with low and standard H_2O concentrations were grouped together, and the steady state O_3 concentration with the photolysis lamps off measured both before and after each of these groups. These five light intensity groups were performed in random sequence. The steady state O_3 results are listed in Table 3. The transient O_3 curves obtained are shown in Figs. 29-38 of Section IV.

Table 3
Observed Steady State Ozone Concentrations during Experiments 1-10

Observation Time (Seconds)	$[O_3]$ (10^{15} molecules/cm^3)	$[H_2O]$	Relative Photolysis Intensity	Experiment Number
-75 - 75	14.72	0.0	0	
345 - 495	4.863	0.0	5	1
585 - 600	4.889	0.0	5	1
735 - 885	5.471	68.0	5	1
1005 - 1020	5.529	68.0	5	1
1425 - 1575	4.994	0.0	5	1
1725 - 1875	5.093	0.0	5	2
1965 - 1980	5.098	0.0	5	2
2115 - 2265	5.388	6.8	5	2
2445 - 2460	5.415	6.8	5	2
2805 - 2955	5.118	0.0	5	2
3315 - 3465	15.64	0.0	0	
3705 - 3855	12.37	0.0	1	3
3945 - 3960	12.38	0.0	1	3
4095 - 4245	11.77	6.8	1	3
4365 - 4380	11.71	6.8	1	3
4725 - 4875	12.28	0.0	1	3
5085 - 5235	12.08	0.0	1	4
5325 - 5340	12.01	0.0	1	4
5475 - 5625	10.71	68.0	1	4
5745 - 5760	10.64	68.0	1	4
6225 - 6375	11.64	0.0	1	4
6585 - 6735	14.57	0.0	0	
7035 - 7185	8.561	0.0	2	5
7305 - 7320	8.484	0.0	2	5
7455 - 7605	8.102	68.0	2	5
7725 - 7740	8.060	68.0	2	5
8085 - 8235	8.211	0.0	2	5
8385 - 8535	8.164	0.0	2	6
8625 - 8640	8.060	0.0	2	6
8775 - 8925	7.892	6.8	2	6
9045 - 9060	7.824	6.8	2	6
9405 - 9555	7.685	0.0	2	6

Table 3 (Continued)

Observation Time (Seconds)	$[O_3]$ (10^{15} molecules/cm^3)	$[H_2O]$	Relative Photolysis Intensity	Experiment Number
9765 - 9915	12.86	0.0	0	
10425 - 10575	12.38	0.0	0	
10785 - 10935	4.483	0.0	4	7
11025 - 11040	4.454	0.0	4	7
11175 - 11325	4.755	6.8	4	7
11445 - 11460	4.731	6.8	4	7
11805 - 11955	4.295	0.0	4	7
12105 - 12255	4.217	0.0	4	8
12345 - 12360	4.182	0.0	4	8
12495 - 12645	4.666	68.0	4	8
12765 - 12780	4.633	68.0	4	8
13185 - 13335	3.971	0.0	4	8
13665 - 13815	10.81	0.0	0	
14085 - 14235	4.538	0.0	3	9
14325 - 14340	4.513	0.0	3	9
14475 - 14625	4.907	68.0	3	9
14745 - 14760	4.883	68.0	3	9
15105 - 15255	4.372	0.0	3	9
15405 - 15555	4.282	0.0	3	10
15645 - 15660	4.237	0.0	3	10
15795 - 15945	4.501	6.8	3	10
16065 - 16080	4.458	6.8	3	10
16425 - 16575	3.992	0.0	3	10
16845 - 16995	9.036	0.0	0	

Addition of H_2O to the system started immediately after the second O_3 measurement in each experiment and stopped after the fourth measurement. The third and fifth measurements were taken after steady state was reached for the wet and dry conditions, respectively.

E. OH Modulation Experiments

Measurements of OH vibration-rotation line intensities were carried out in the apparatus shown in Fig. 3. The D_2 lamp was used to monitor O_3 in the ultraviolet and the diode laser employed for OH absorption measurements in the infrared. The cell pathlength was kept at 2962 cm throughout this investigation. The 1200 line/mm grating was used for the O_3 measurements of 3150 Å and the 300 line/mm grating used for the high resolution work near 2.95 microns. The monochromator slits were set at 200 microns, which gave resolutions of 1.67 Å and 6.66 Å in the UV and IR, respectively.

The four chemical modulation frequencies employed were 7.8125, 15.625, 31.25 and 62.5 Hz. The modulated photolysis lamp intensity was observed both with the photodiode monitor directly and with the PMT/monochromator set to detect scattered 2537 Å radiation, and the phase shifts of the lamps with respect to the Ithaco "chemical" lockin and the ratio of A.C. to D.C. intensity measured. Both detection systems gave the same $A.C._{peak}/D.C.$ ratio of 0.65 at all frequencies. The lamp phase shifts measured by the photodiode were larger than those measured by the PMT, due to the photodiodes slower response time; so, the PMT phase shifts were selected for use in the later analysis. The phase shift and attentuation factor of the 1800 Hz carrier demodulator were measured for the four modulation frequencies with the modulation standard described earlier. For the experiments where modulation signals were measured off of the D.C. carrier, the phase shift and attenuation factor of the IR detector preamplifier's

5 Hz high pass filter were calculated for each frequency. All the phase and attenuation data described are shown in Table 4.

Helium carrier gas flows through each flow circuit were kept constant throughout this investigation. In standard liters/minute they are: total-3.66, H_2O-0.80, O_3-0.28. These conditions give a cell pressure with no O_3 or H_2O added of 67.5 ± 0.5 Torr, an H_2O concentration (when present) of 6.8×10^{16} molecules/cm^3, and an O_3 concentration in the absence of photolysis of ~1.5×10^{15} molecules/cm^3. For all the run sequences the steady state O_3 concentration was measured with the lamps off, with the lamps on and the H_2O off, and with the lamps and H_2O on. For run sequence 2 these three quantities were measured after the sequence as well. These measurements are required later to calculate the absolute OH concentration modulation amplitude.

Four vibration-rotation transitions were investigated. In the nomenclature of Maillard, Chauville and Mantz[17] (see Section IV-B, Fig. 39) they are:

P(4.5) 1-	3407.6069 cm^{-1}
P(4.5) 1+	3407.9890 cm^{-1}
P(3.5) 2-	3421.9360 cm^{-1}
P(3.5) 2+	3422.0123 cm^{-1}

The intensity of the first one, P(4.5) 1-, was measured very carefully, and the intensities of the other three measured relative to it. Run

Table 4
Measured Phase Shifts and Attenuation Factors
for Modulation System Components

Frequency (Hz)	Lamp[a] ϕ	IR Preamp ϕ	IR Preamp Attn.	1800 Hz lock in ϕ	1800 Hz lock in Attn.
7.8125	-177.47°	-32.62°	.842	-18.57°	1.001
15.625	-178.94°	-17.74°	.952	-36.70°	.947
31.25	-178.40°	- 9.09°	.987	-70.09°	.781
62.5	-179.39°	- 4.57°	.997	-122.58°	.448

a Photolysis light phase as measured by Ithaco "chemical" lock in amplifier.

sequence 1 investigated the P(4.5) 1- and 1+ lines in the 3407.75 cm^{-1} region. The monochromator was set as close as possible to this frequency and a good laser mode located. The monochromator setting was fine tuned so that it straddled the expected positions of the P(4.5) 1+ and 1- lines by using the 3407.826 cm^{-1} H_2O line as an absolute frequency reference and the 0.0486 cm^{-1} fringe spacing of the elaton to measure positions relative to the H_2O line. This particular frequency region has no H_2O lines strong enough to observe in direct absorption; so, the line used had to be located by first derivative detection. This derivative signal is shown in Fig. 14 with the H_2O line marked C, along with the etalon trace. When the chemical conditions were set for OH observation with the lamps flashing at 15.625 Hz, the diode was slowly scanned ($1x10^{-4}$ A/s) over this region, I_o recorded on the X-Y recorder, and the modulation signal components recorded with the data acquisition computer. The resulting modulation amplitude signal is shown in Fig. 14. Peaks A and B come up exactly at the frequencies predicted for the P(4.5) 1- and P(4.5) 1+ OH lines, respectively, indicating that they are hydroxyl radical signals. A second scan at a slower speed ($1x10^{-5}$ A/s) was made in the region near peak A. Modulation signals and I_o were recorded as before. The results are shown in Fig. 15. Particular note should be taken of the phase spectrum, which is very flat in the absorption region and random where there is no absorption. The observed absorption profiles were fit to gaussians by a non-linear least squares method, and the results shown in Fig. 16-18. Although

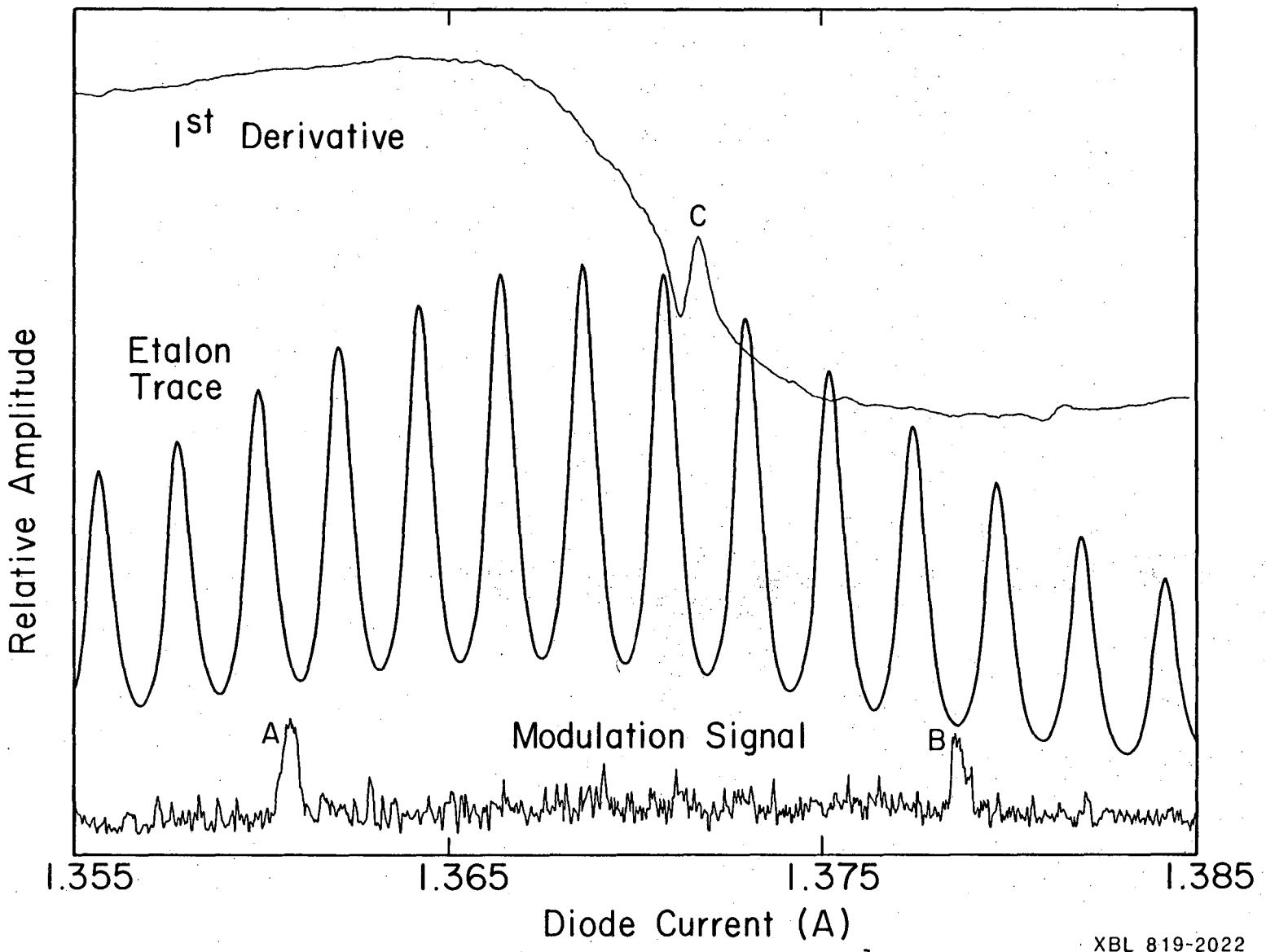

XBL 819-2022

Fig. 14. Laser wavelength calibration near 3407.75 cm^{-1}. A = 3407.607 cm^{-1} OH, B = 3407.989 cm^{-1} OH, C = 3407.826 cm^{-1} H_2O.

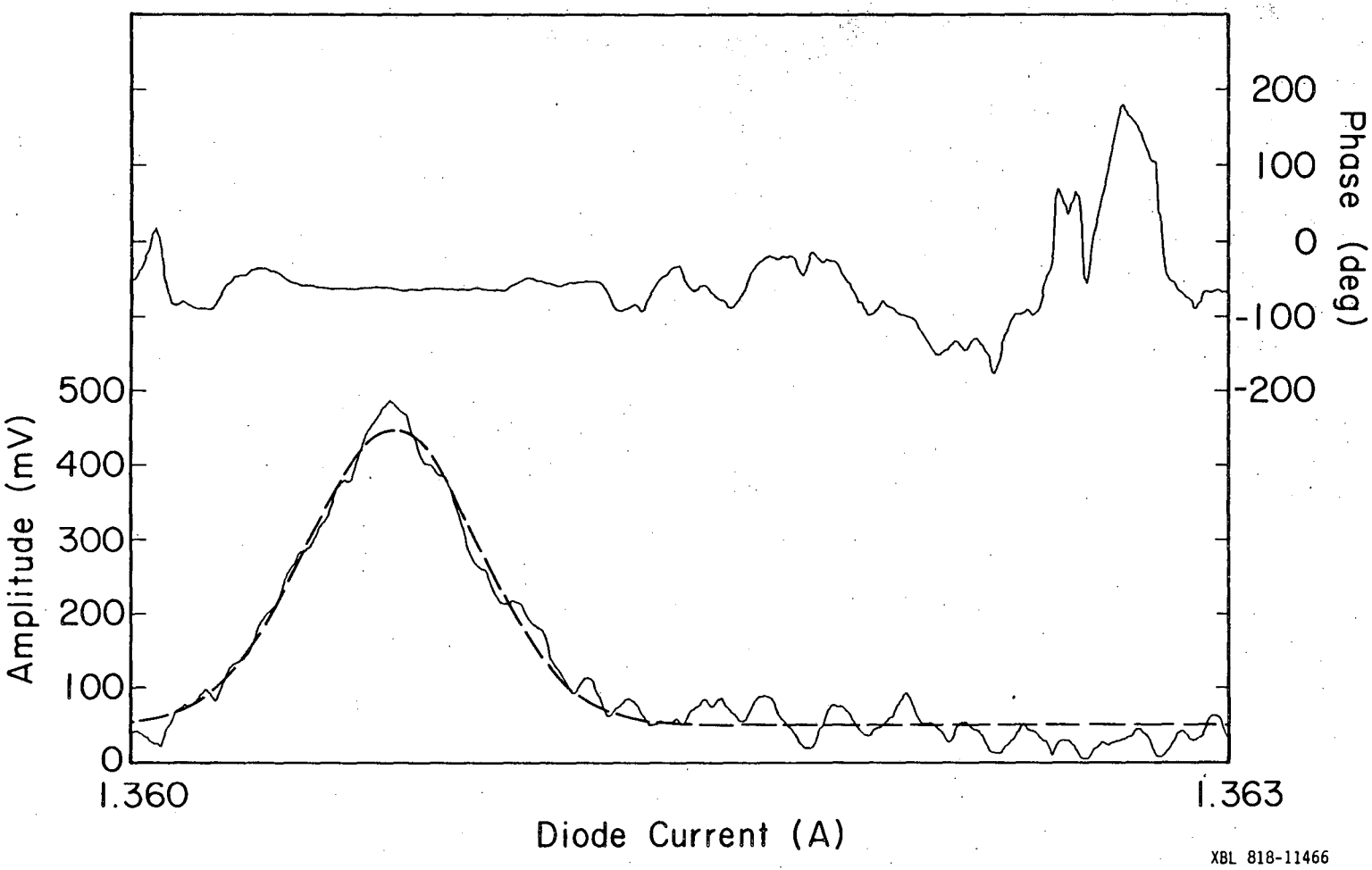

Fig. 15. Modulation phase and amplitude spectrum for the P(4.5) 1- OH transition.

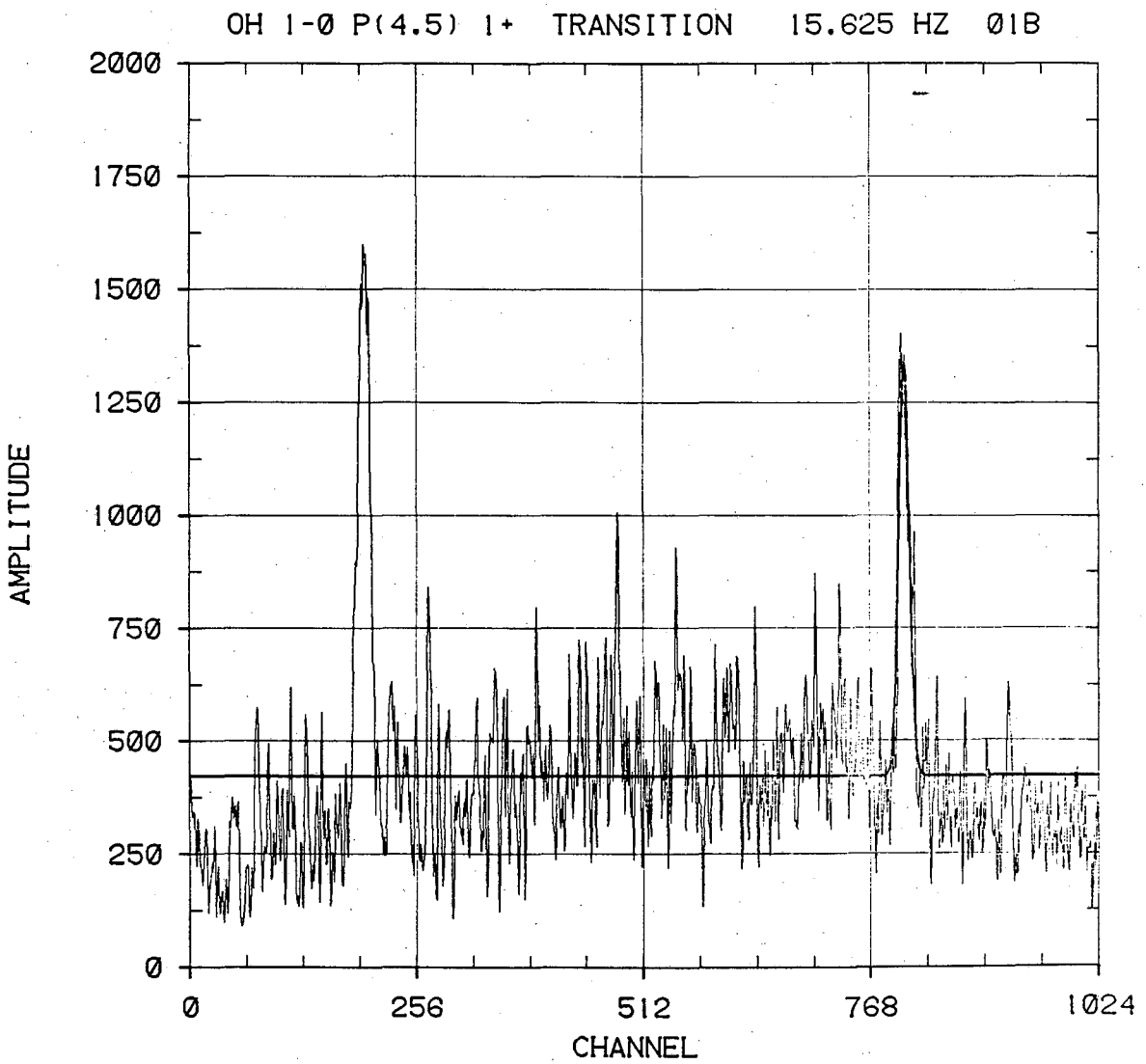

Fig. 16. Gaussian fit to P(4.5) 1+ transition(broad scan). Run 1.

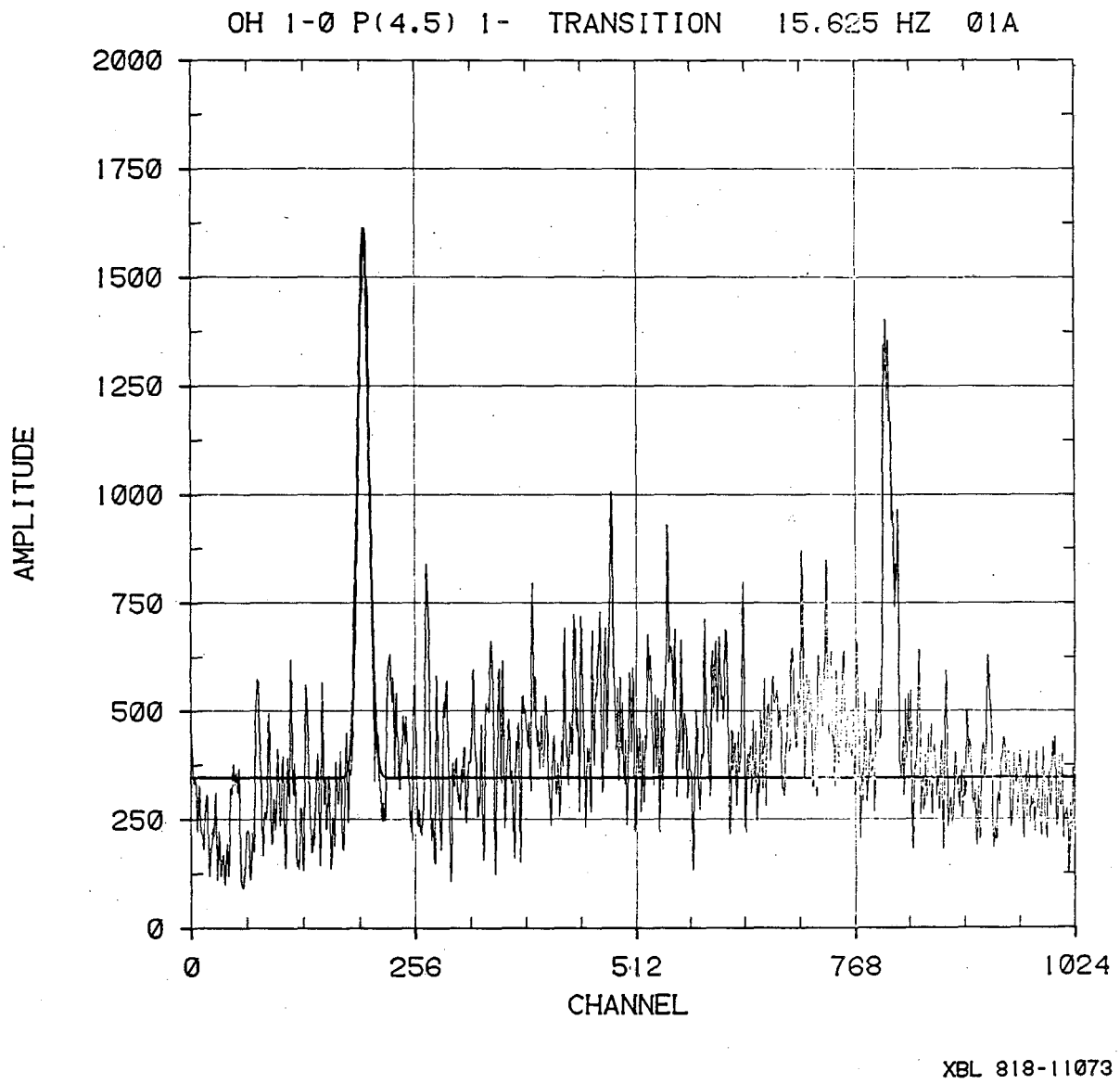

Fig. 17. Gaussian fit to P(4.5) 1- transition (broad scan). Run 1.

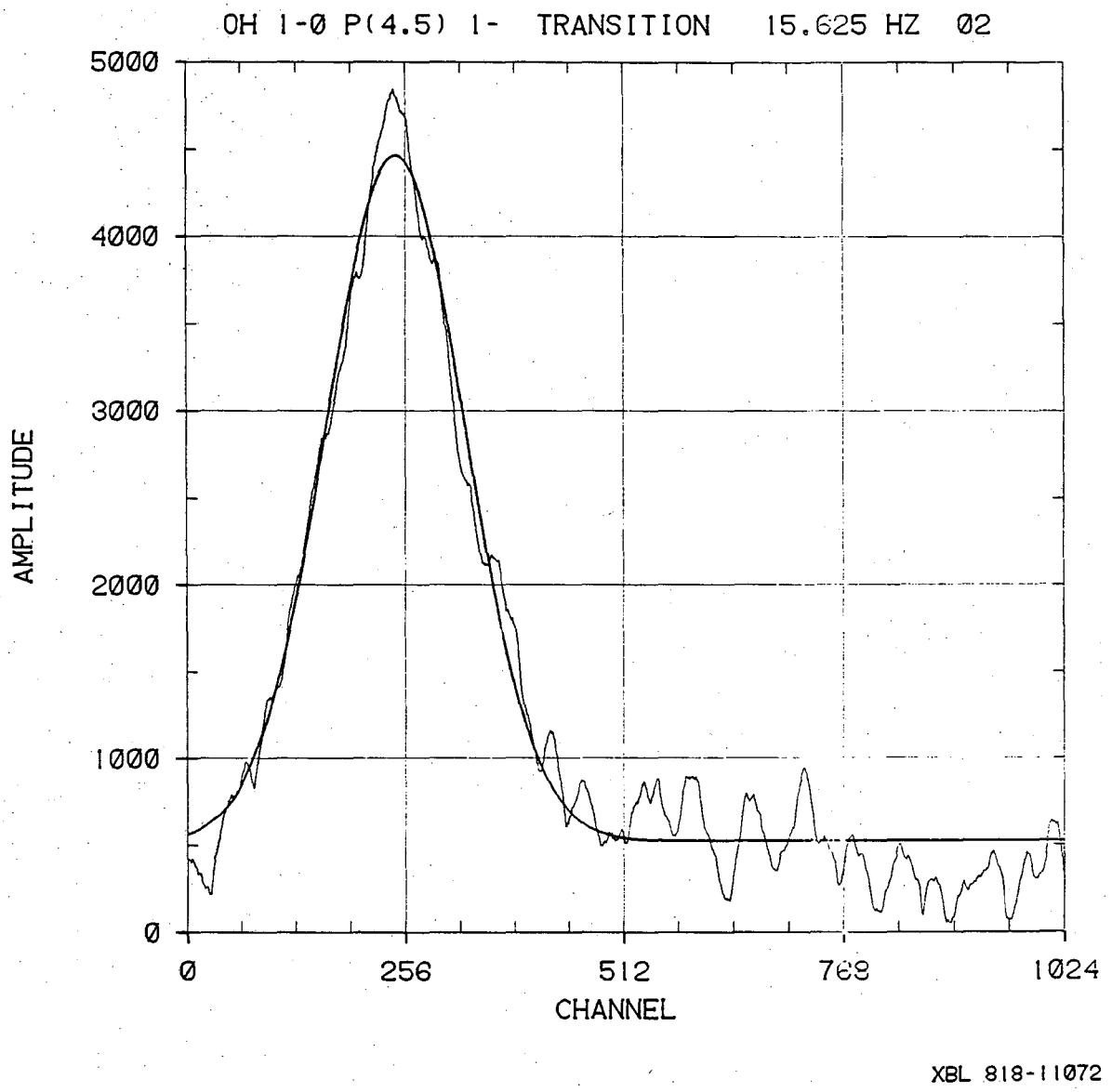

Fig. 18. Gaussian fit to P(4.5) 1- transition (narrow scan). Run 1.

the lineshapes are slightly pressure broadened and should be Voigt profiles, the shapes were not measured well enough to be able to fit that function.

Run sequence 2 investigated the dependence of the P(4.5) 1- signal on flashing frequency. In this sequence the O_3 measurements were performed both at the beginning and end of the sequence. Since the diode had been warmed up to room temperature since run sequence 1, a new laser mode had to be located. This time the H_2O line was located by second derivative detection, as shown in Fig. 19. The 3407.826 cm^{-1} H_2O line is peak B, and peaks A and C are the P(4.5) 1- and 1+ OH lines. A 3.4 mA region near peak A was scanned slowly ($1x10^{-5}$ A/s) while I_o was recorded (5 second time constant) and the modulation signal components recorded (4 second time constant). This was done for all four flashing frequencies, performed in random order. Even with the carrier demodulator time constant set at its minimum, the 62.5 Hz signal is appreciably attenuated. To improve the signal quality the modulation signals on the D.C. carrier were measured by connecting the IR detector directly to the chemical lockin amplifier. Although these measurements give only relative amplitudes (the D.C. carrier amplitude cannot be detected), good phase shift measurements did result. The modulation signals were fit to gaussians and are shown for the 1800 Hz carrier signals in Fig. 20a-d and for the D.C. carrier signals in Figs. 21a-d.

Run sequence 3 investigated the intensity of the P(3.5) 2+ and 2- transitions relative to P(4.5) 1+. In the 3422.0 cm^{-1} region there are several strong H_2O transitions which can be observed in

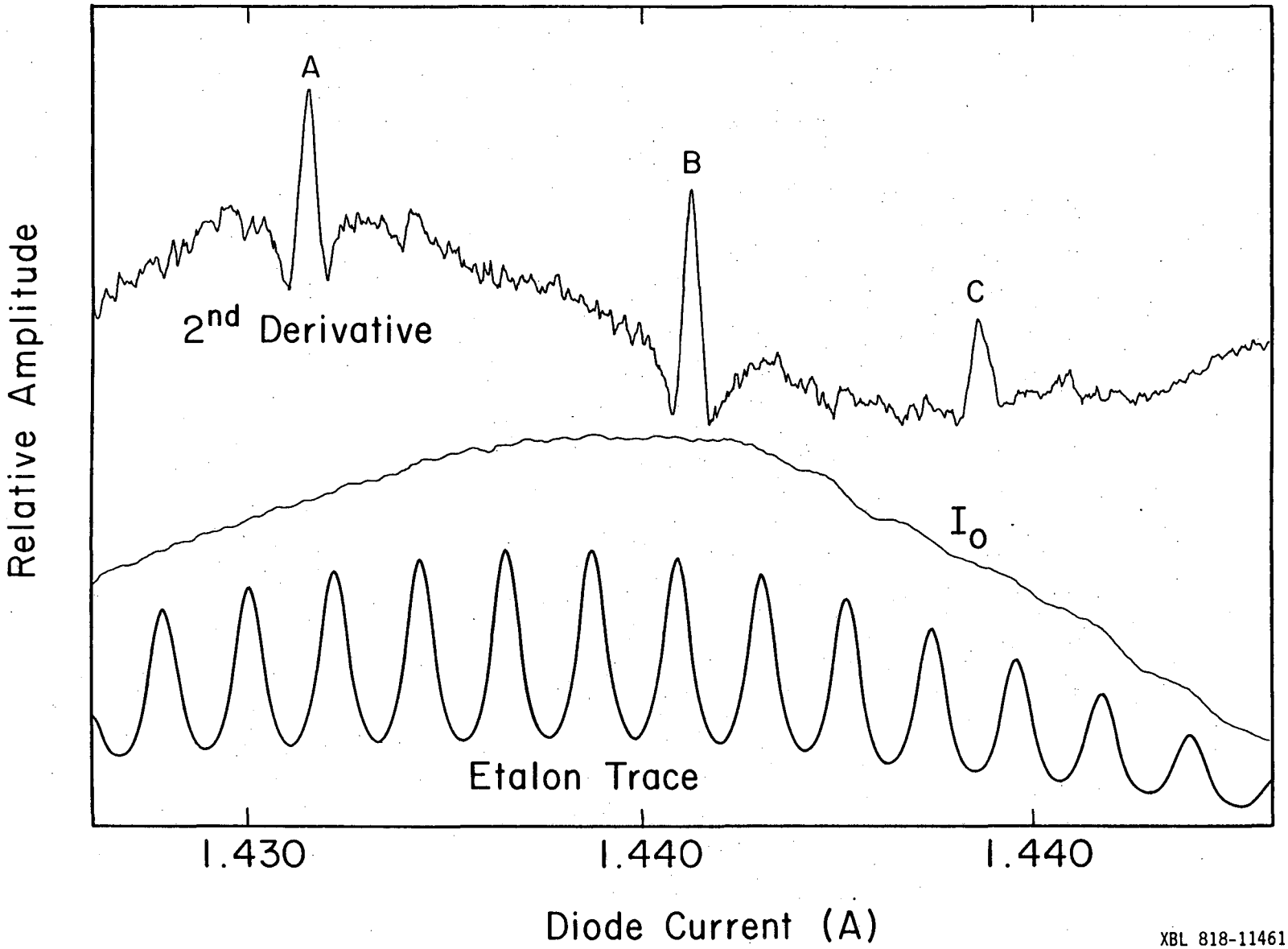

XBL 818-11461

Fig. 19. Laser wavelength calibration near 3407.75 cm^{-1}. A=3407.607 cm^{-1} OH, B=3407.826 cm^{-1} H_2O, C=3407.989 cm^{-1} OH.

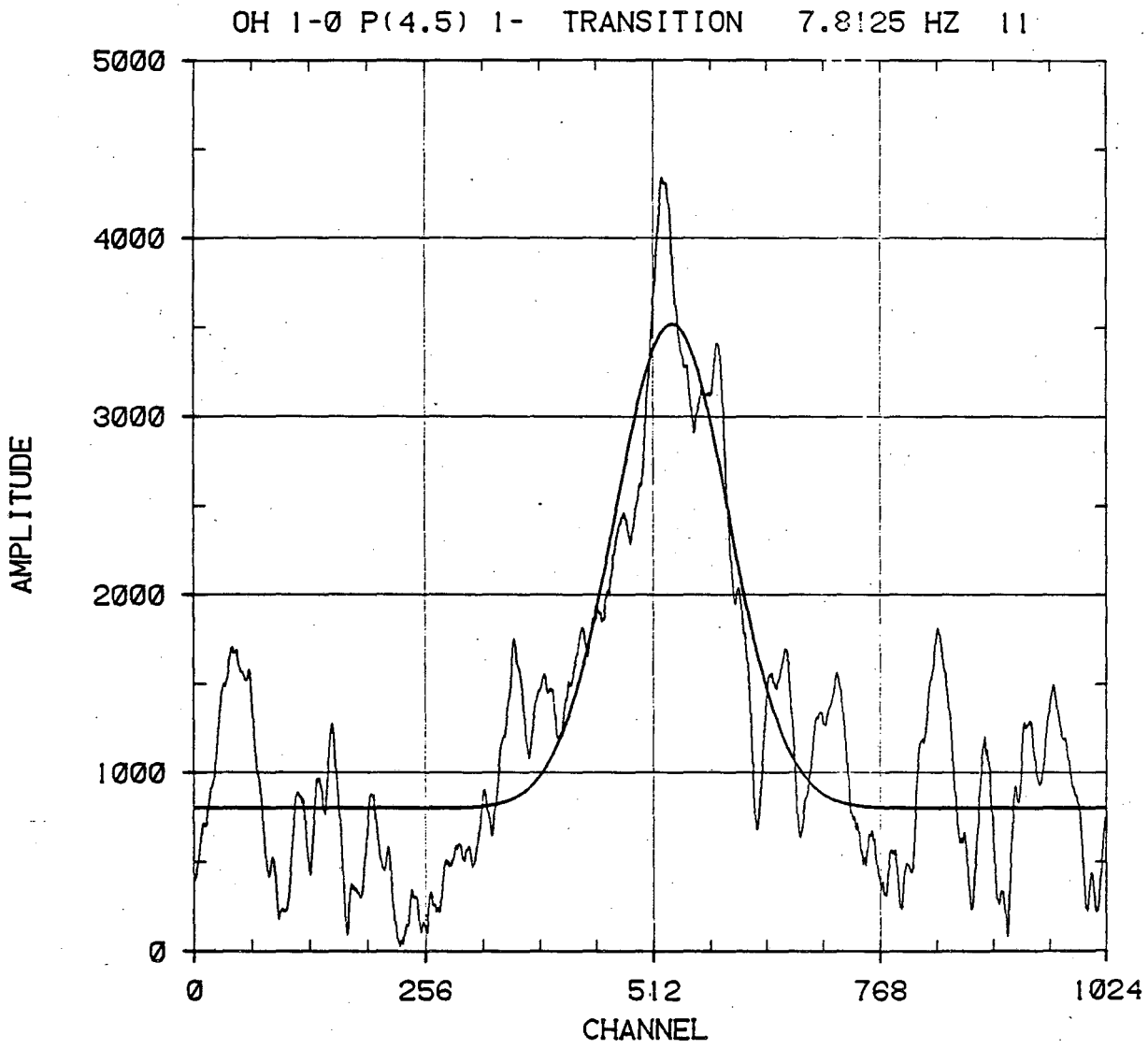

Fig. 20a. Gaussian fit to P(4.5) 1- transition 1800 Hz carrier 7.8 Hz Run 2.

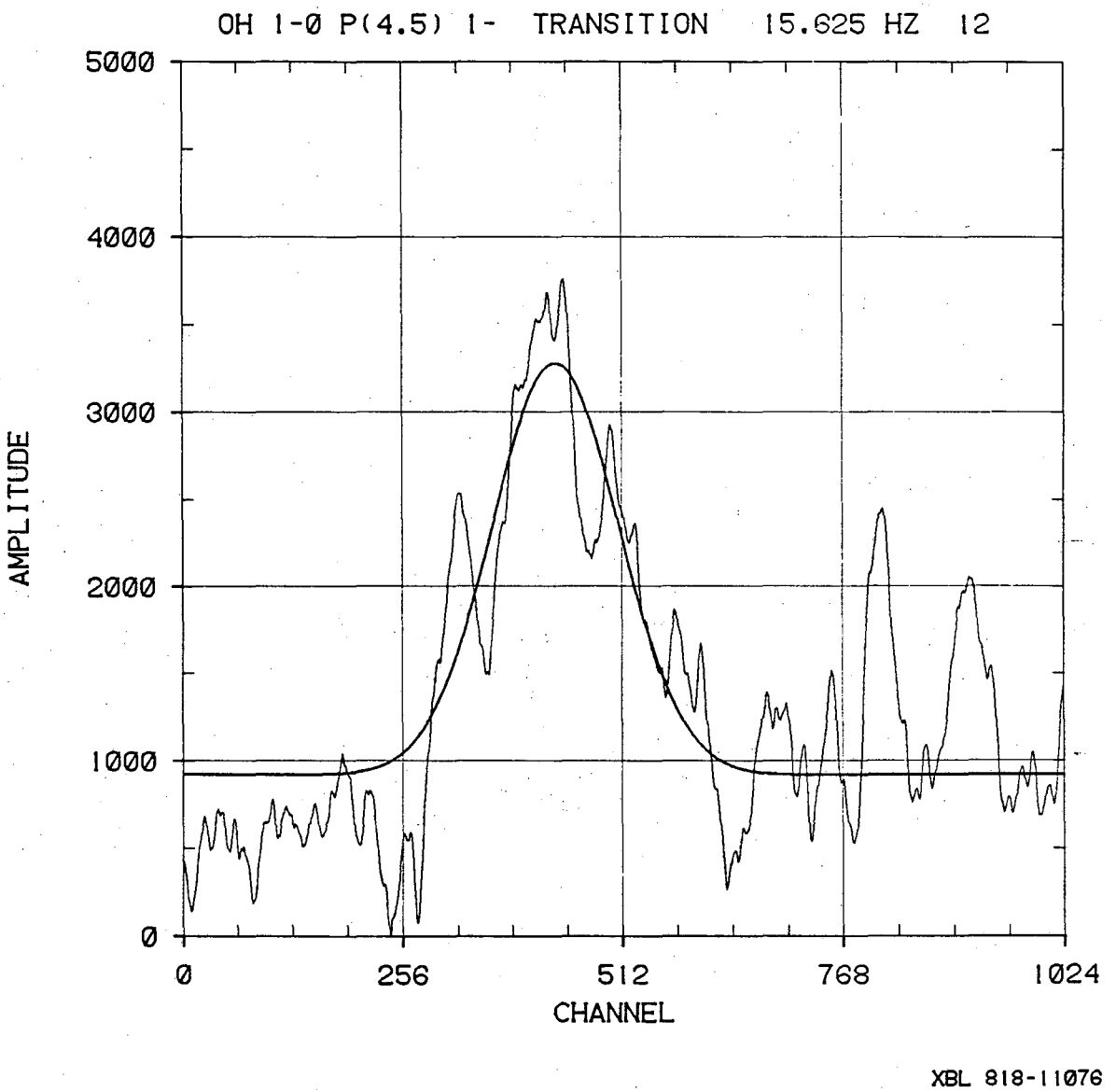

Fig. 20b. Gaussian fit to P(4.5) 1- transition 1800 Hz carrier 15.6 Hz Run 2.

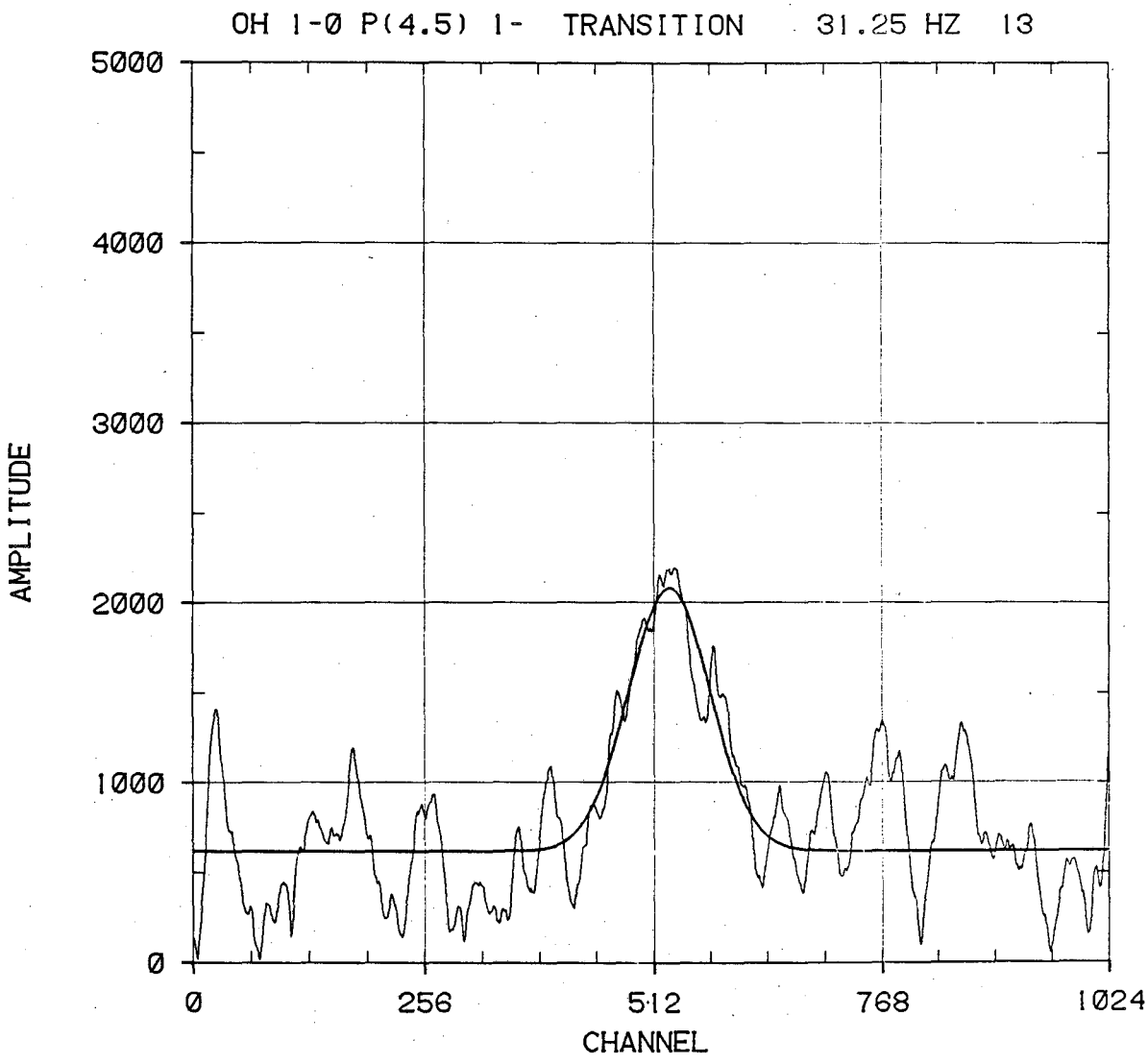

XBL 818-11077

Fig. 20c. Gaussian fit to P(4.5) 1- transition 1800 Hz carrier 31.3 Hz. Run 2.

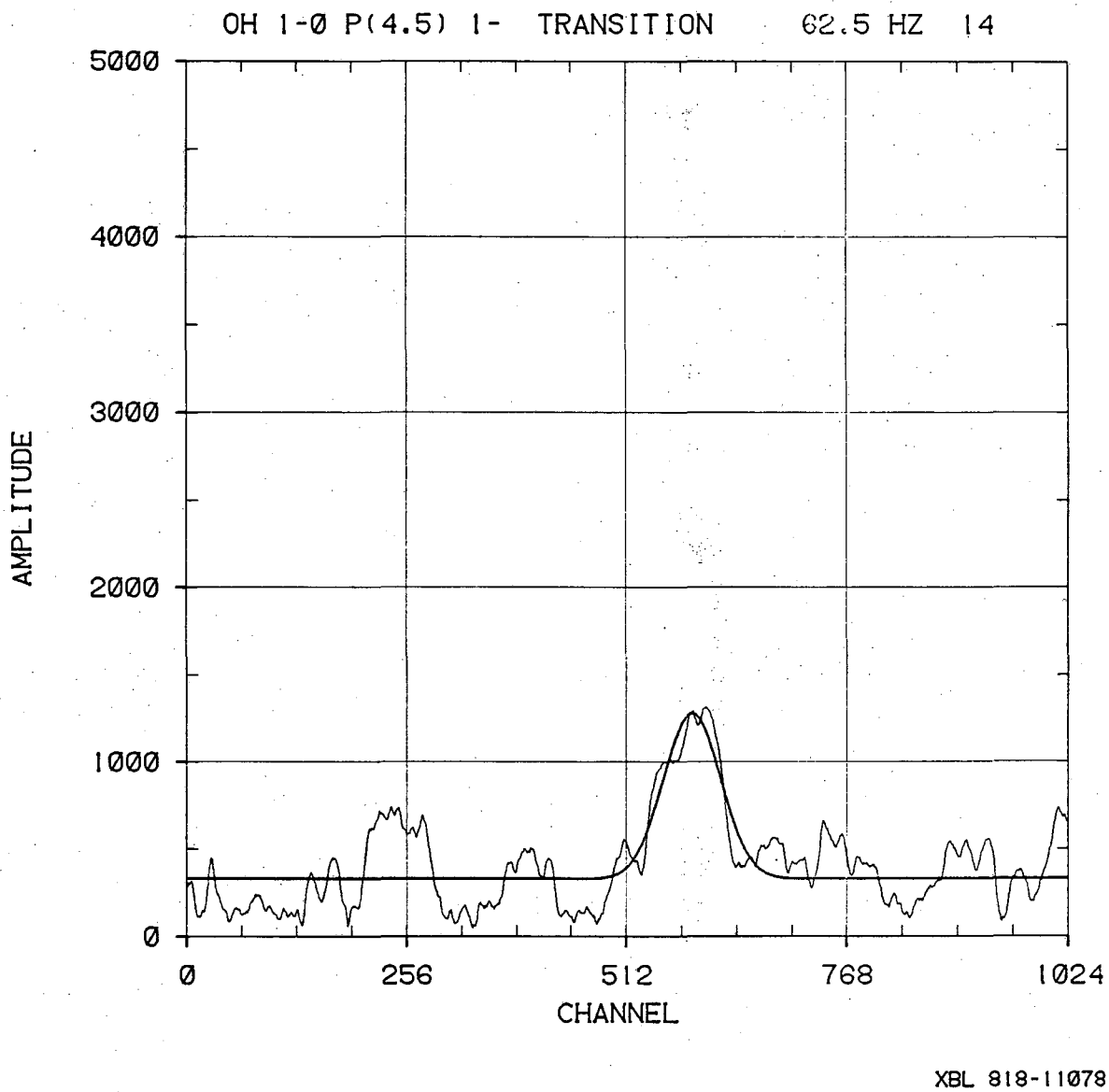

Fig. 20d. Gaussian fit to P(4.5) 1- transition 1800 Hz carrier 62.5 Hz. Run 2.

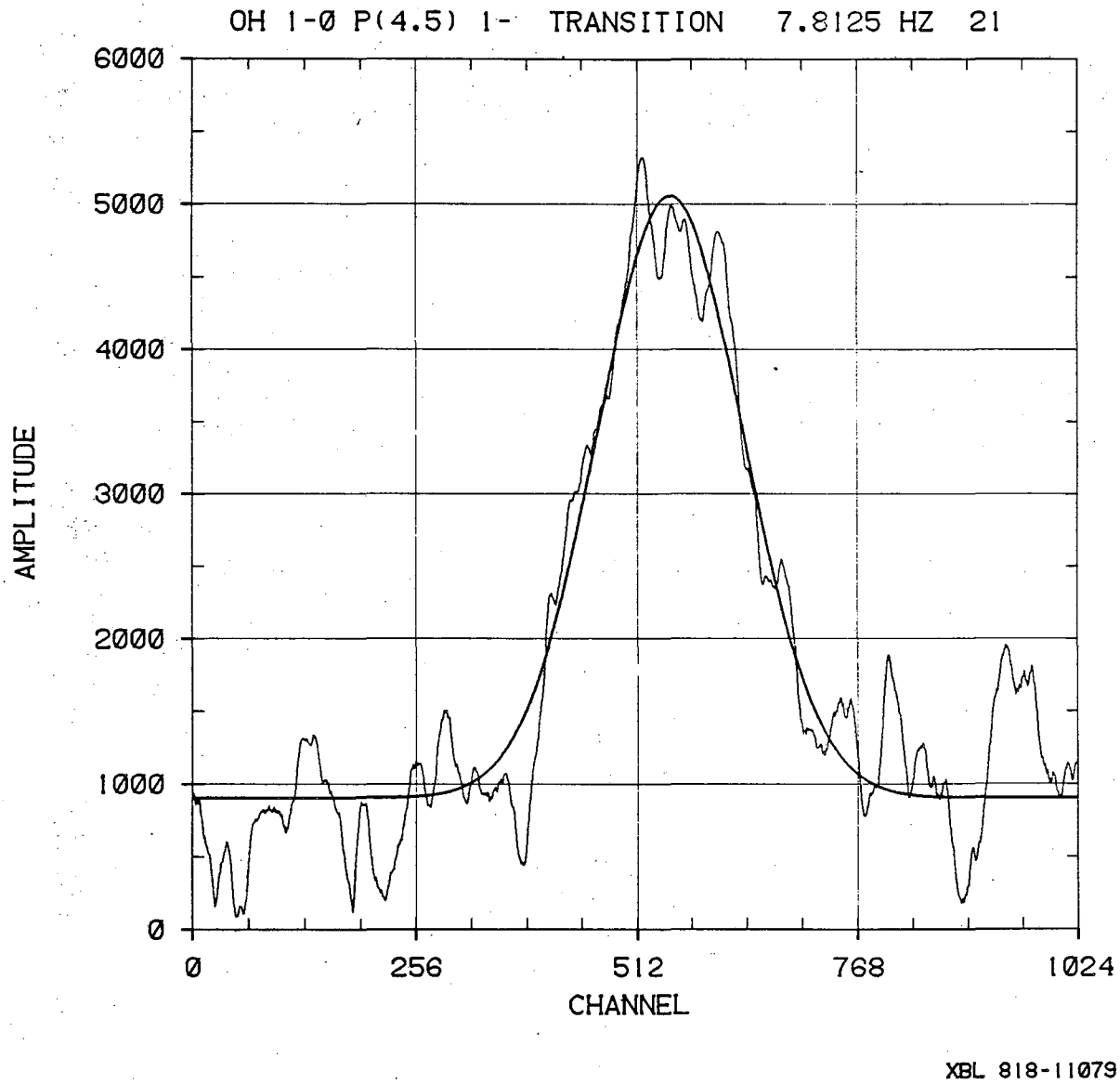

Fig. 21a. Gaussian fit to P(4.5) 1- transiton D.C. carrier 7.8 Hz. Run 2.

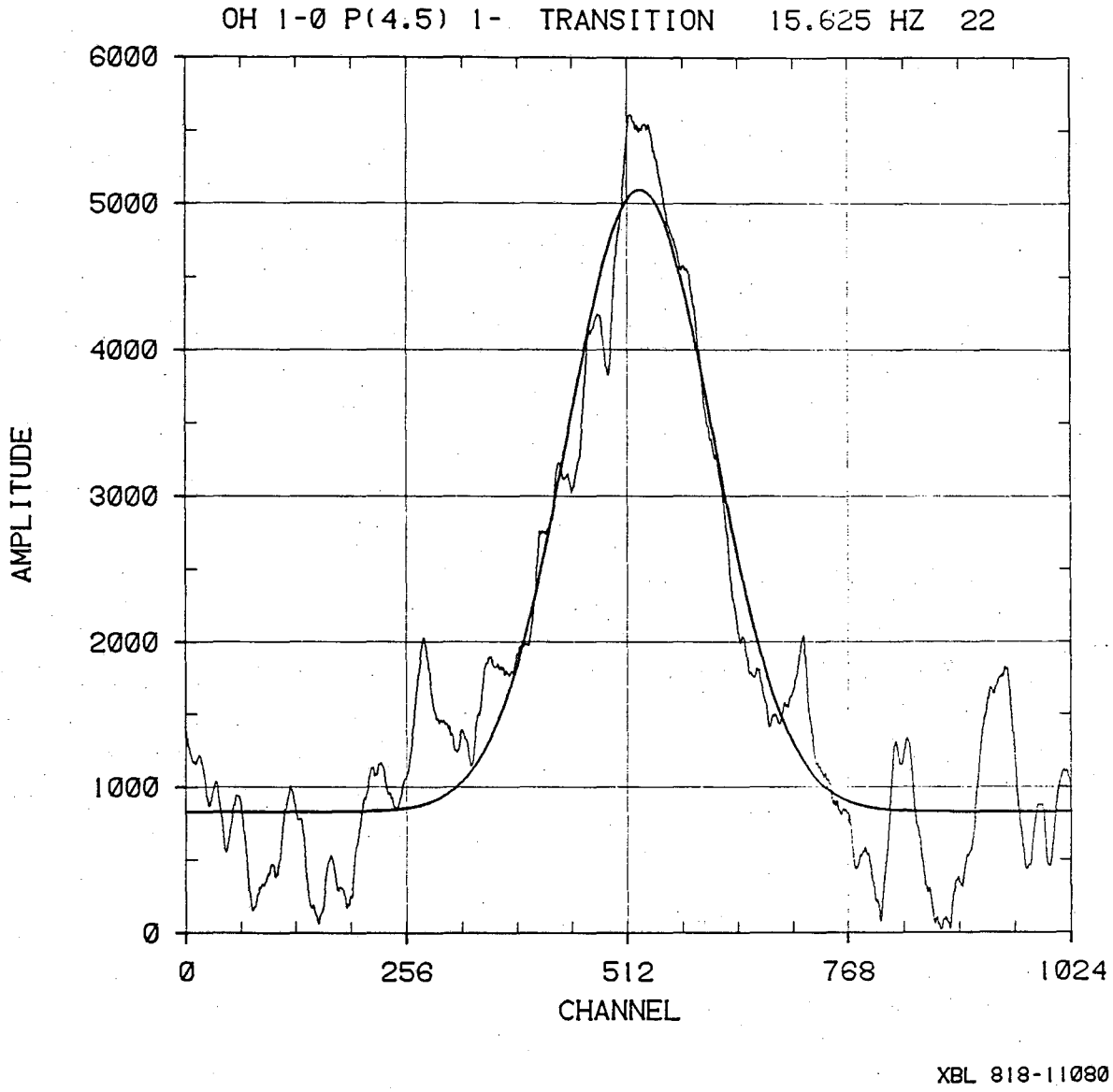

Fig. 21b. Gaussian fit to P(4.5) 1- transiton D.C. carrier 15.6 Hz. Run 2.

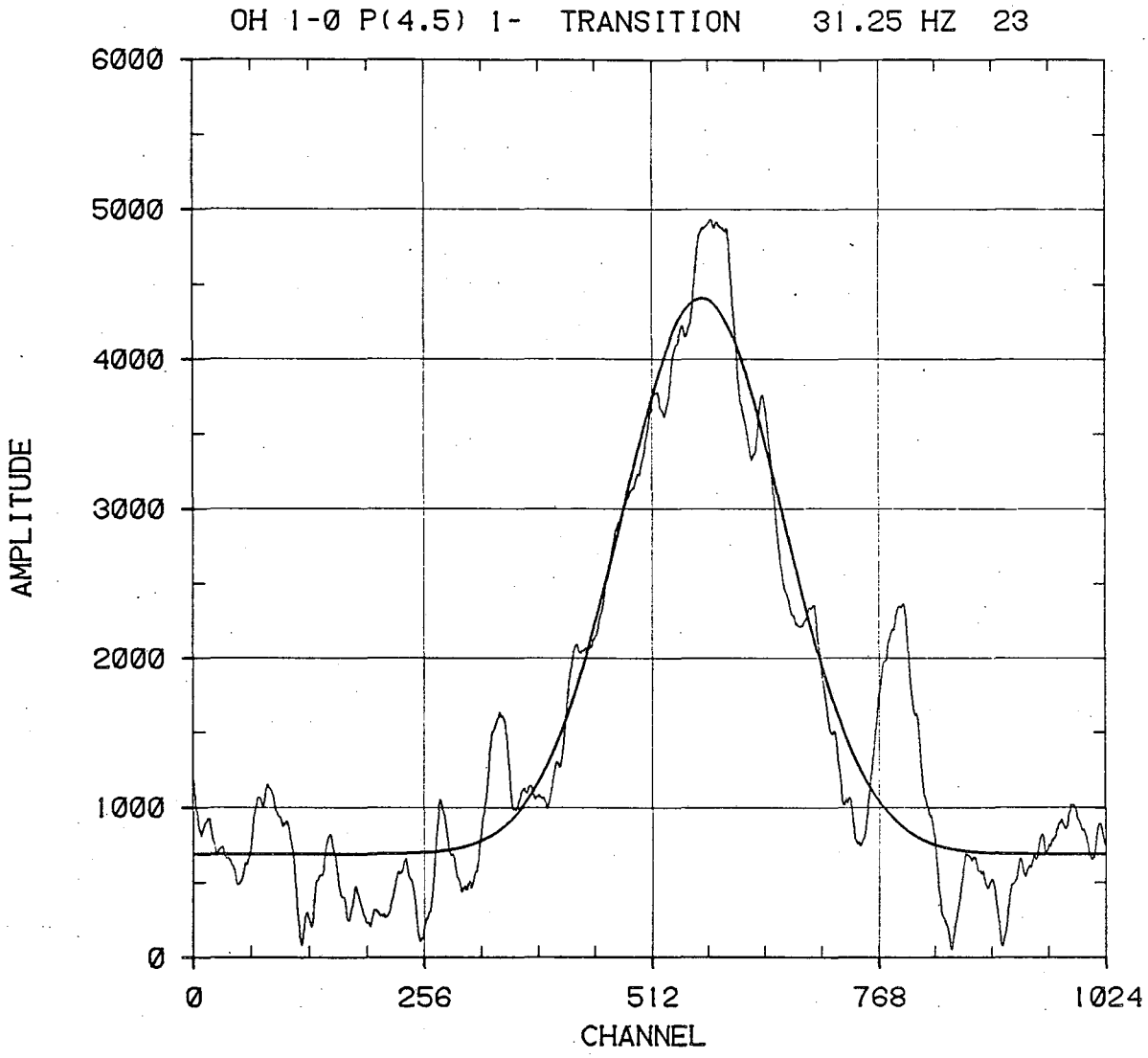

Fig. 21c. Gaussian fit to P(4.5) 1- transition D.C. carrier 31.3 Hz. Run 2.

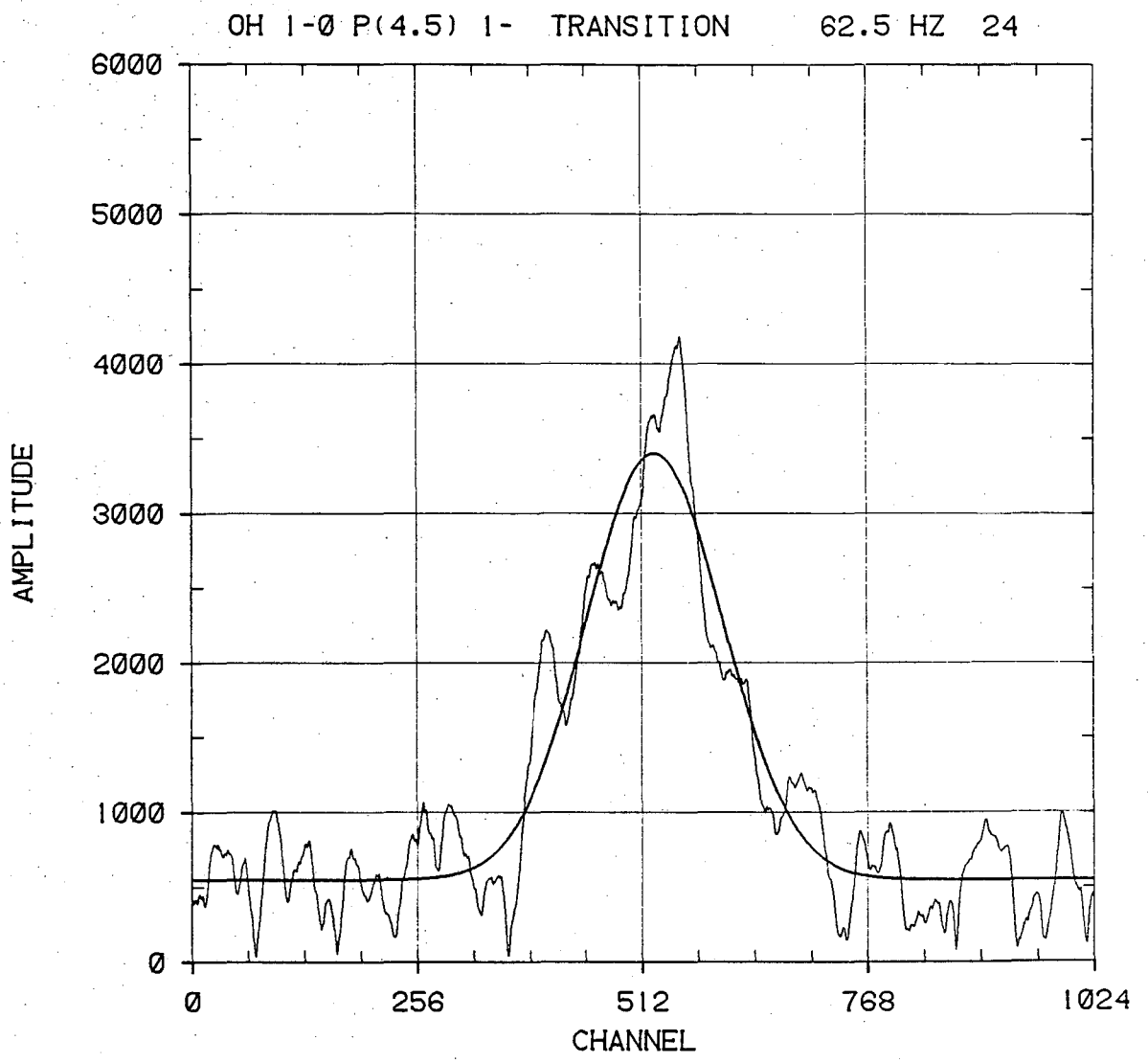

Fig. 21d. Gaussian fit to P(4.5) 1- transition D.C. carrier 62.5 Hz. Run 2.

direct absorption, as well as another one which appears in second derivative. The second derivative trace shown in Fig. 22 contains the following transitions:

A 3421.739 cm^{-1} H_2O

B 3421.936 cm^{-1} OH P(3.5) 2-

C 3422.012 cm^{-1} OH P(3.5) 2+

D 3422.272 cm^{-1} H_2O

E 3422.333 cm^{-1} H_2O

F 3422.369 cm^{-1} H_2O

The transitions A, E and F which are seen in direct absorption are offscale in the derivative trace. A 6.5 mA region overlapping peaks B and C was scanned as before at $1x10^{-5}$ A/s. Fine tuning of the optical path alignment resulted in a doubling of laser intensity through the system; so, the previous scan was repeated. Several hours were then spent in search of a good laser mode for the 3407.75 cm^{-1} region. A mode was found that performed well for the P(4.5) 1+ line, so it was scanned. Several scans were then made of the P(4.5) 1- line, but the results were poor. A second derivative scan of this region revealed that this laser mode had a break right where P(4.5) 1- occurs; so, no more scans were made. The OH transitions observed in this run sequence were fit to gaussians and are shown in Figs. 23-27.

Fig. 22. Laser wavelength calibration near 3422.0 cm^{-1}.

A = 3421.739 cm^{-1} H_2O

B = 3421.936 cm^{-1} OH

C = 3422.012 cm^{-1} OH

D = 3422.272 cm^{-1} H_2O

E = 3422.333 cm^{-1} H_2O

F = 3422.369 cm^{-1} H_2O

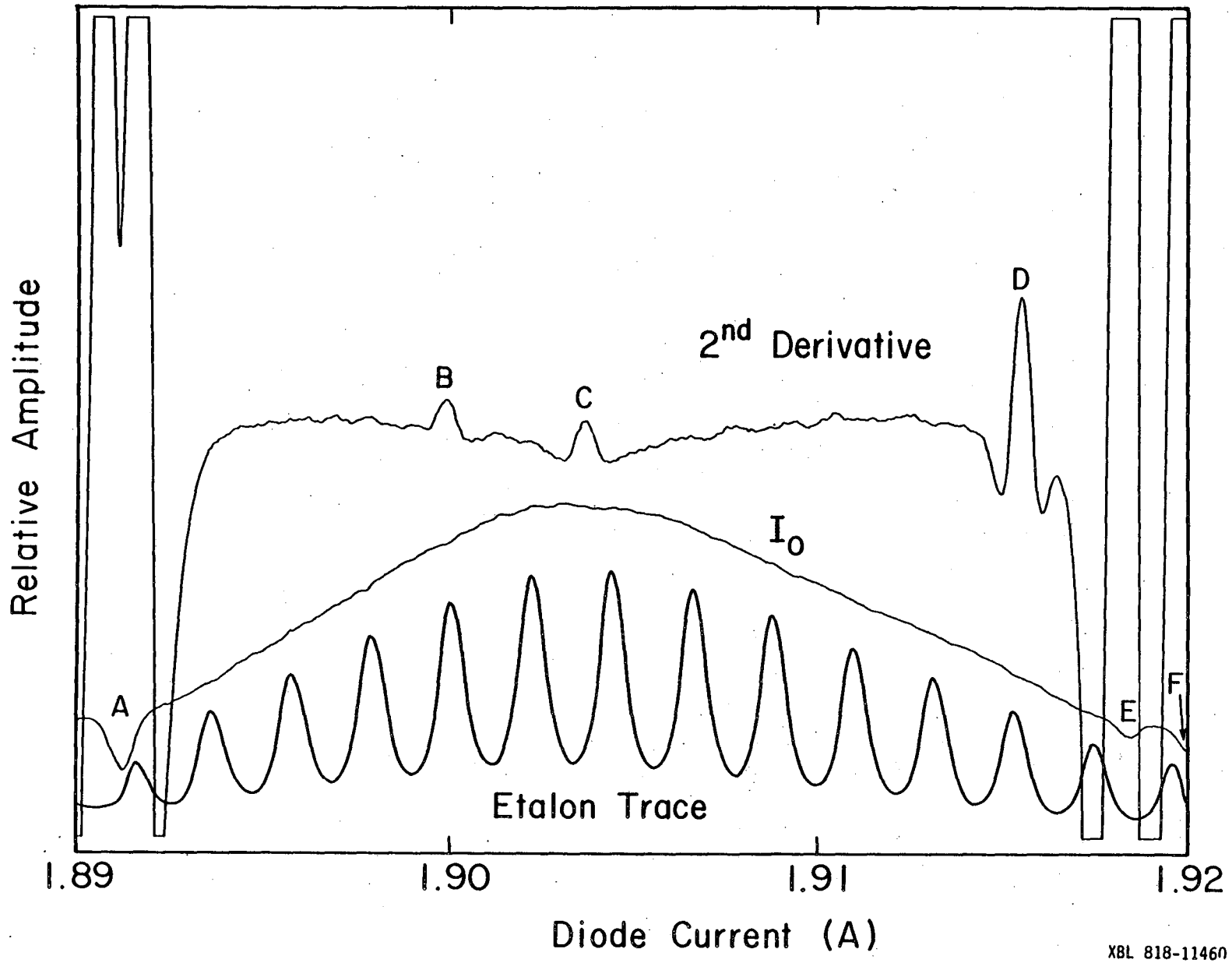

Fig. 22. Laser wavelength calibration near 3422.0 cm^{-1}.

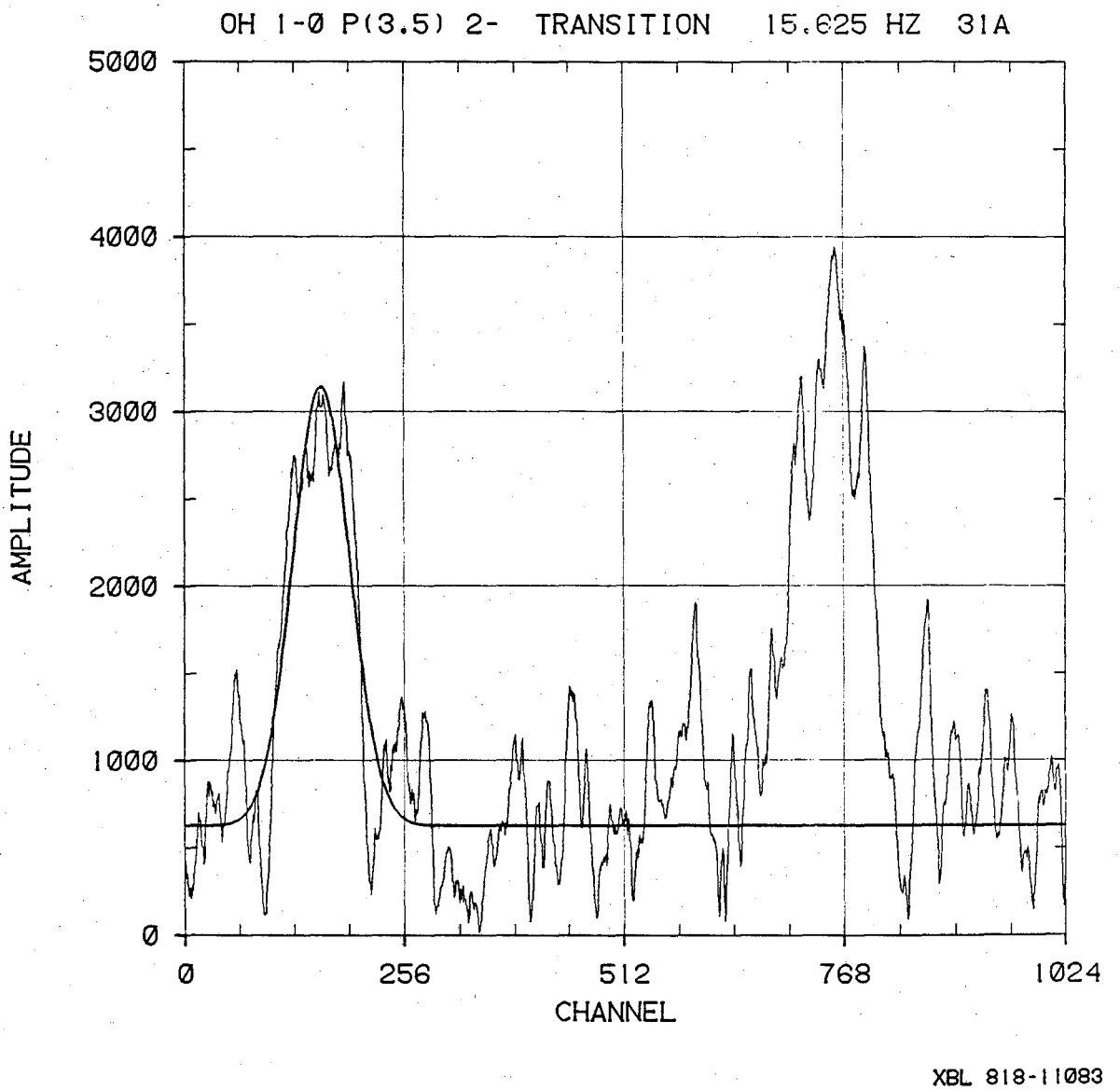

Fig. 23. Gaussian fit to P(3.5) 2- transition scan 1. Run 3.

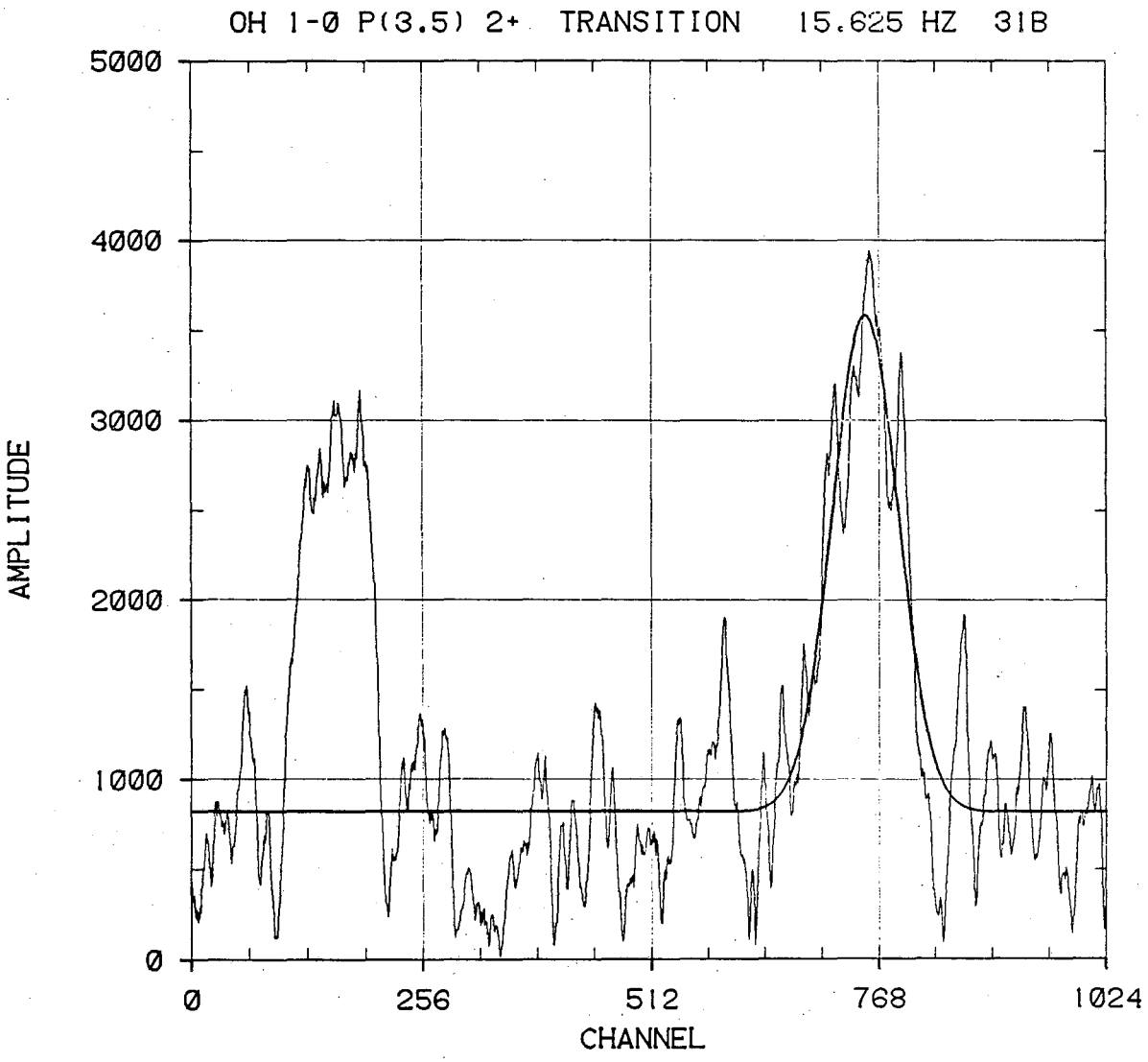

Fig. 24. Gaussian fit to P(3.5) 2+ transition scan 1.

Run 3.

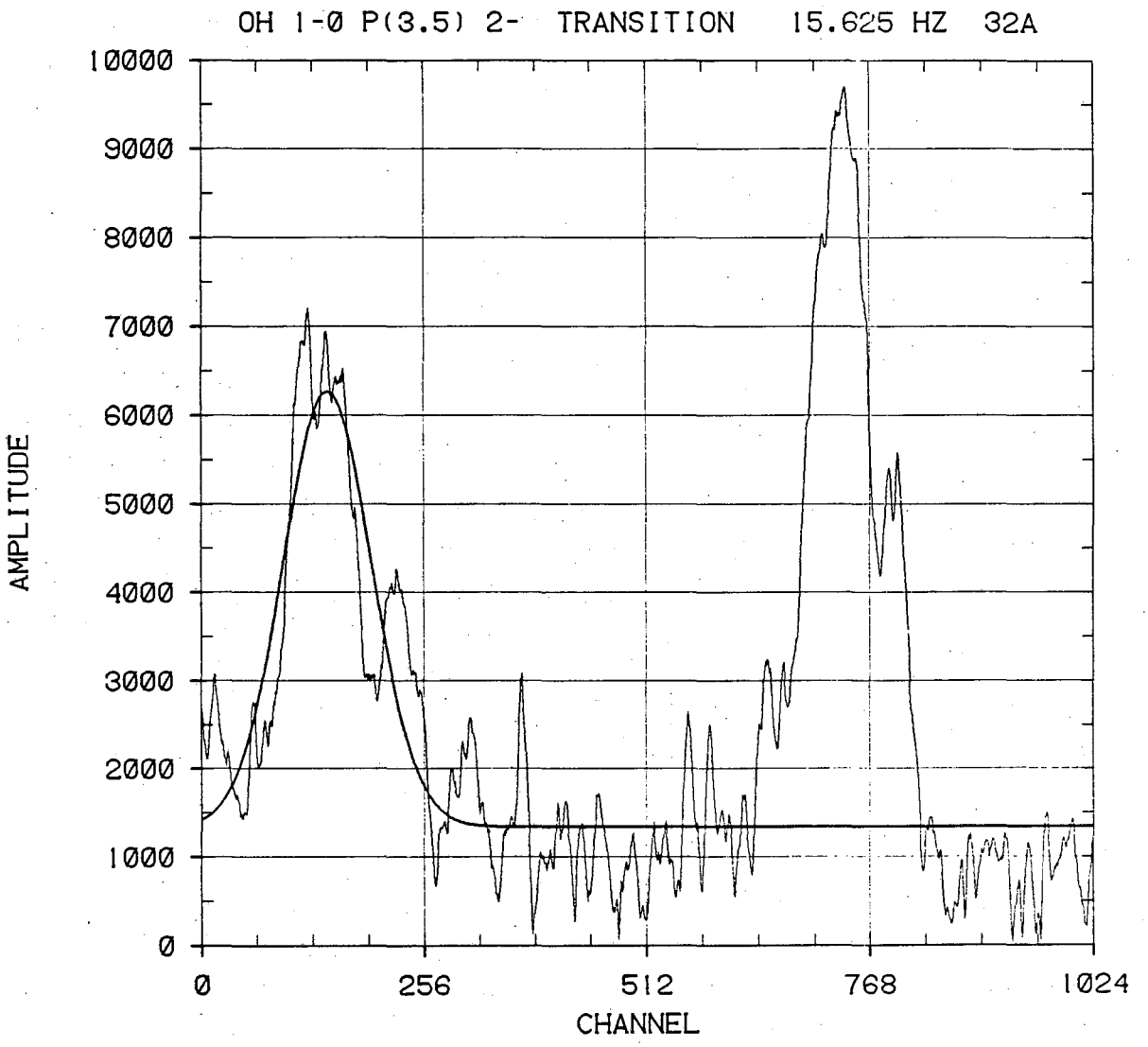

XBL 818-11085

Fig. 25. Gaussian fit to P(3.5) 2- transition scan 2.

Run 3

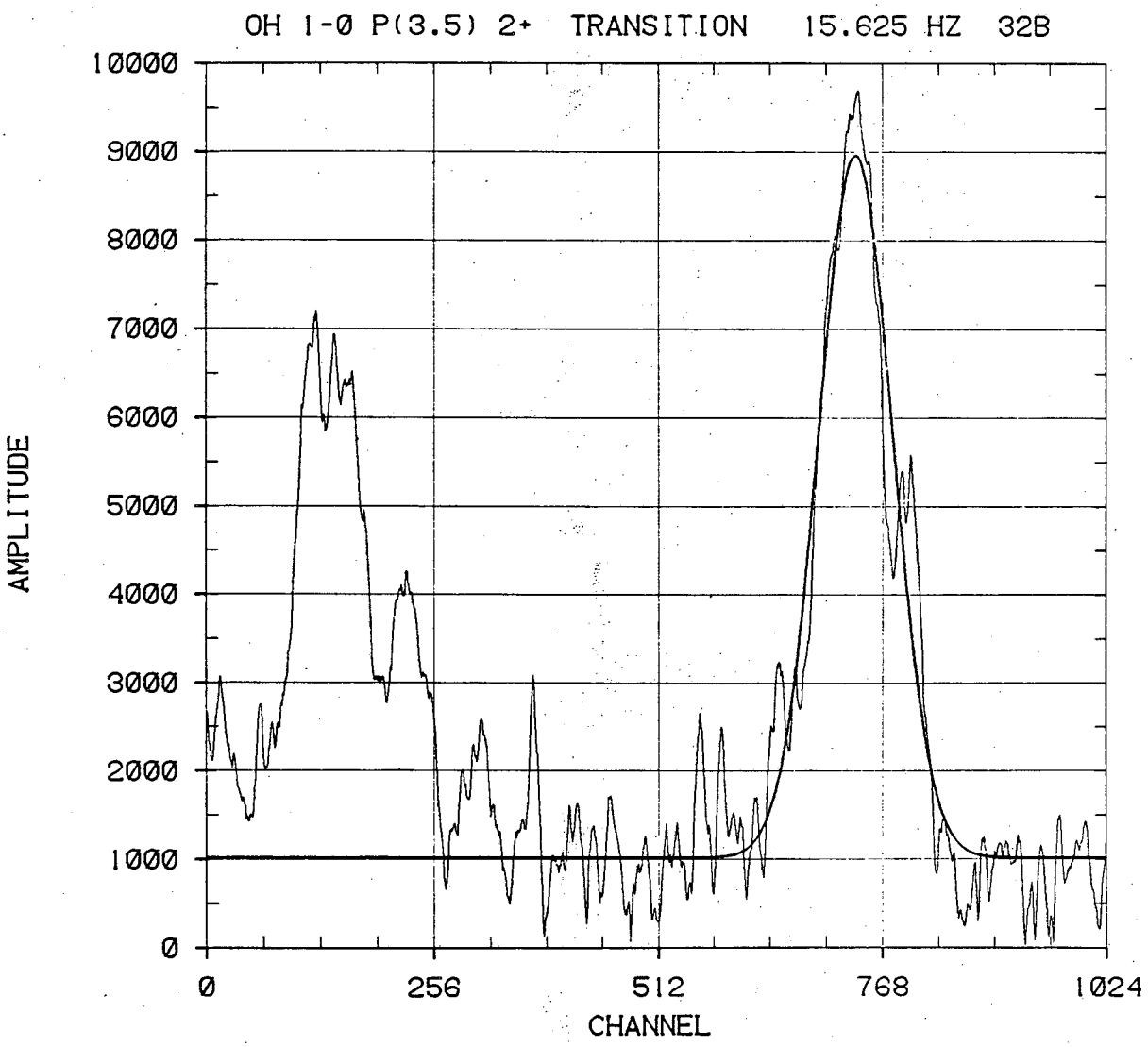

Fig. 26. Gaussian fit to P(3.5) 2+ transition scan 2. Run 3.

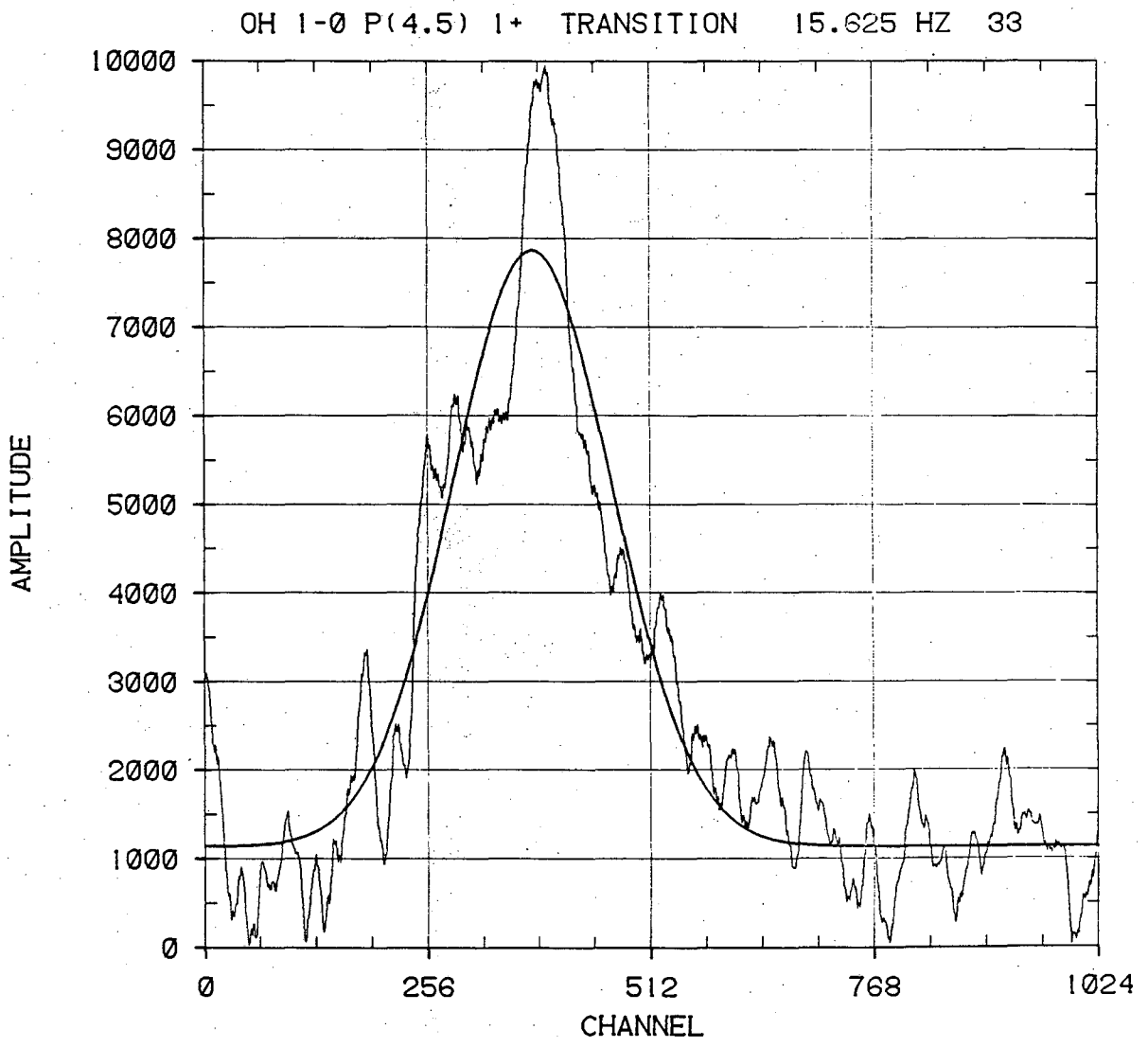

Fig. 27. Gaussian fit to P(4.5) 1+ transition. Run 3.

IV. RESULTS AND DISCUSSION

A. HO_2-O_2 ($^1\Delta$) Energy Transfer Rate

The data obtained in the O_3-H_2O steady state photolysis investigation, described in Section III-D, was analyzed in several steps. Inspection of the O_3 measurements made in the absence of photolysis indicated that the flow rate of O_3 into the cell initially increased, leveled off, and finally decreased with time. The initial increase is attributed to migration of adsorbed O_3 in the trap toward the exit port, while the later decrease is due to overall depletion of O_3 on the silica gel. These dark O_3 measurements were fit to the functional form:

$$[O_3] = K_1(1-K_2e^{-\alpha_2 t})\, e^{-\alpha_1 t} = C_1e^{-\alpha_1 t} - C_2e^{-(\alpha_1+\alpha_2)t} \qquad (52)$$

where t is time in seconds, starting at the midpoint of the time interval during which O_3 was first measured. The fit was very good ($\sigma \cong 0.7$ percent), and the results are listed in Table 5. To obtain this O_3 concentration profile in a flow system with a flow out rate constant k_f requires that the O_3 flow in rate be described by the function:

$$f(O_3) = F_1e^{-\alpha_1 t} - F_2e^{(-\alpha_1+\alpha_2)t} = G_1(1-G_2e^{-\alpha_2 t})\, e^{-\alpha_1 t} \qquad (53)$$

$$G_1 = F_1 = C_1(k_f-\alpha_1)$$

$$F_2 = C_2(k_f-\alpha_1-\alpha_2)$$

$$G_2 = F_2/F_1$$

Table 5
Dark O_3 concentration versus time

$$[O_3] = C_1 e^{-\alpha_1 t} - C_2 e^{-(\alpha_1+\alpha_2)t}$$

$C_1 = 2.362 \times 10^{16}$ molecules/cm^3, $C_2 = 8.904 \times 10^{15}$ molecules/cm^3

$\alpha_1 = 5.552 \times 10^{-5}$ s^{-1} , $\alpha_2 = 1.860 \times 10^{-4}$ s^{-1}

Time (Seconds)	$[O_3]_{exp}$	$[O_3]_{calc}$ (10^{16} molecules/cm^3)	$\Delta[O_3]$ (%)
0	1.472	1.472	0.0
3390	1.564	1.564	0.0
6660	1.457	1.454	-0.2
9840	1.286	1.285	-0.1
10500	1.238	1.248	0.8
13740	1.081	1.069	-1.1
16920	0.904	0.908	0.4

This flow-in function is duplicated in the simulation program by invoking the following pseudo-reactions:

$$\begin{array}{lcll} & \longrightarrow & A & \alpha_2 \\ A & \longrightarrow & & \alpha_2 \\ B & \longrightarrow & & \alpha_1 \\ A + B & \longrightarrow & A + B + O_3 & G_1 \end{array} \qquad (54)$$

By starting at t=0 with $A=(1-G_2)$ and B=1, the pseudo-species A and B develop in time as:

$$A = 1 - G_2 e^{-\alpha_2 t}$$

$$B = e^{-\alpha_1 t}$$

which results in the flow rate for O_3 to exactly follow the required functional form. For the sake of numerical accuracy and efficiency the species A and B were scaled up to about 10^{15} to be comparable to the O_3 concentration. Tests of this mechanism in the numerical simulation program verified that it did produce the correct O_3 behavior.

Simulation of the period of dry O_3 photolysis at the beginning of each experiment allowed determination of the photolysis intensity during that experiment. Initial guesses based on previous work were made for the lamp intensity at each current setting employed, and these values used when the lamps were "turned on" at the appropriate

times in the simulation sequence. The simulation results for each experiment were then averaged over the time interval corresponding to that experimental O_3 measurement and the calculated and observed values compared. Generally the agreement was only good to about 25 percent. If the assumption is made that each absorbed photon destroys a constant number, ϕ, of O_3 molecules under all conditions, the relationship between photolysis intensity I, O_3 cross section σ, steady state O_3 concentration during photolysis $[O_3]$, and in the absence of photolysis $[O_3]_0$ in a flow system with flow out rate constant k_f, is:

$$[O_3]^{-1} = [O_3]_0^{-1} + (\sigma\phi I)/(k_f[O_3]_0) \tag{55}$$

which can be simplified to:

$$[O_3]^{-1} = a + bI. \tag{56}$$

For each experiment the calculated value of $[O_3]$ is now known at I=0 and $I=I_g$, the initial guess value. This information was used to solve for a and b in equation 56, and the value of I corresponding to the O_3 concentration measured in each experiment calculated. These new guesses for I were used in the simulation, and the calculated and experimental results again compared. Since the assumption about ϕ is only approximate, exact agreement does not result. However, in a small region around the correct photolysis intensity for each experiment, equation 56 should describe the system better than it does over

the large intensity range 0 to I_g, so the results from the first two simulation runs were interpolated using equation 56 to yield a better set of values for I. When these values were employed in a simulation sequence, agreement between calculated and experimental O_3 values for all experiments was very good, better than the experimental precision. The photolysis intensities determined by this procedure are listed in Table 6.

The final feature of the data to fit is the change in steady state O_3 upon addition of H_2O to the photochemical system. Earlier investigation of this O_3-H_2O system indicated that the observation, under some conditions, of O_3 increase on addition of H_2O could not be simulated with any reasonable values for the rate constants of the key HO_x reactions without invoking $O_2(^1\Delta)$ quenching by HO_2. Also, the HO_2 concentrations calculated, and hence optimum rate constant, are dependent on the $OH+HO_2$ reaction rate constant, which has been reported[23] to be somewhere in the range $4-20\times10^{-11}$ cm^3/molecule s. Therefore, it was decided to simulate the experiments using a range of values both for the quenching rate constant, k_{49}, and for the $OH+HO_2$ reaction rate constant, k_{24}.

Using the reaction set described in Appendix A, the entire experimental sequence listed in Table 3 was simulated twenty five times, using values for k_{24} of 2,4,8,16 and 32 x 10^{-11} cm^3/molecule s, and for k_{49} of 1,2,4,8 and 16 x 10^{-11} cm^3/molecule s. The simulation results for each experiment and each set of k_{24} and k_{49} values were then averaged over the time interval corresponding

Table 6
Photolysis Intensity Determination

Exp. No.	Time Interval (seconds)	O_3 (10^{15} molecule s/cm^3)	I (10^{14} photons/cm^2 s)
1	345 - 495	4.863	14.17
2	1725 - 1875	5.093	14.17
3	3705 - 3855	12.37	2.23
4	5085 - 5235	12.08	2.15
5	7035 - 7185	8.561	4.86
6	8385 - 8535	8.164	4.69
7	10785 - 10935	4.483	10.94
8	12105 - 12255	4.217	10.71
9	14085 - 14235	4.538	7.82
10	15405 - 15555	4.282	7.53

to the experimental wet O_3 steady state measurement. This time interval (t=150 to 300 seconds, as shown in Figs. 29-38) begins over 120 seconds (2 cell turnover time constants) after H_2O is added, to assure that O_3 steady state has been reached. To determine how well the calculated ozone concentration, $[O_3]_{calc}$, of a simulation sequence using a particular set of k_{24} and k_{49} values compared with the experimental concentrations, $[O_3]_{exp}$, the percent root-mean-square deviation averaged over all ten experiments, PRD, was calculated by the formulas:

$$\text{Percent Deviation (Experiment I)} = PD(I)$$

$$PD(I) = 100 \left([O_3]_{calc}(I) - [O_3]_{exp}(I) \right) / [O_3]_{exp}(I) \qquad (57)$$

$$PRD = \left[(1/10) \sum_{I=1}^{10} PD(I)^2 \right]^{1/2} \qquad (58)$$

The resulting 5 x 5 grid of PRD versus k_{24} and k_{49} was converted to a ten times finer mesh grid (41 x 41) using bicubic spline interpolation. This second grid was used to produce a contour map of PRD versus k_{24} and k_{49}, shown in Fig. 28.

Inspection of Fig. 28 revealed that there is a range of values of k_{24} which are equally capable of describing the experimental results. Since the most recent NASA evaluation of chemical kinetic data[23] suggests considering values as low as 4×10^{-11} and as high as $1\text{-}2 \times 10^{-10}$ cm^3/molecule s for this rate constant, k_{24} values of 4,8 and 16×10^{-11} cm^3/molecule s were chosen for use in evaluating the quenching rate constant k_{49}.

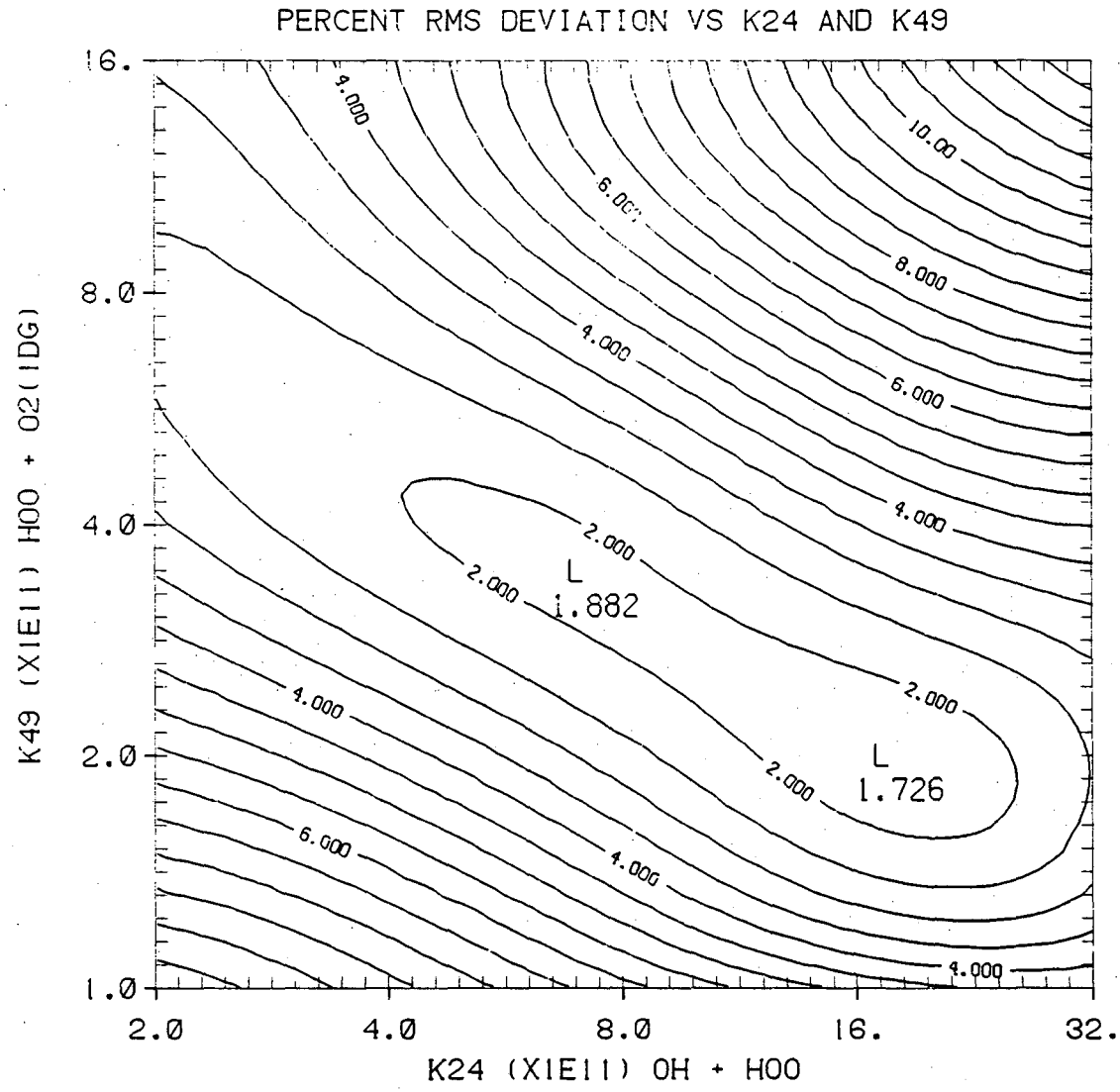

XBL 817-10917

Fig. 28. Contour map of percent rms deviation between calculated and experimental ozone for ten experiments versus rate constants k_{24} and k_{49}.

The optimum k_{49} value of each of the three k_{24} values was initially estimated from the interpolated PRD grid. For each k_{24} value a set of five values of k_{49} spaced $2^{1/2}$ apart and centered around the approximately optimal value, were then selected, simulation sequences run for each of these fifteen sets of rate constants, and the PRDs calculated as before. Cubic spline interpolation of resulting PRD versus k_{49} curves produced the following optimal values of k_{49} for each k_{24}:

$k_{24}(OH+HO_2)$ (cm^3/molecule s)	$k_{49}(HO_2+O_2(^1\Delta))$ (cm^3/molecule s)	PRD (%)
4×10^{-11}	4.4×10^{-11}	2.02
8×10^{-11}	3.0×10^{-11}	1.47
16×10^{-11}	2.4×10^{-11}	1.44

A final set of simulations were run using each of the k_{24} values together with its optimum k_{49} and with the quenching reaction absent ($k_{49} = 0$). The calculated and experimental results are listed for each experiment in Table 7 and shown in Figs. 29a-38c. The curves marked Q were calculated using the optimum quenching rate constant and the curves marked N were calculated with no quenching included. For each experiment the time interval over which the wet steady state O_3 was measured is marked as 150 to 300 in the figures. The "sharp" features which appear between t=15 to t=60 seconds in some of the O_3

Table 7
Wet Steady State Ozone Concentrations

No.	Time Interval (Seconds)	O_3 (10^{15} molecules/cm^3) Measured	Calculated 4.0 (k_{24} in 10^{-11} cm^3/molecule s)	8.0	16.0
1	735 - 885	5.471	5.491	5.522	5.537
2	2115 - 2265	5.388	5.596	5.521	5.450
3	4095 - 4245	11.77	11.34	11.40	11.54
4	5475 - 5625	10.71	10.60	10.74	10.99
5	7455 - 7605	8.102	8.016	8.114	8.293
6	8775 - 8925	7.892	7.831	7.829	7.893
7	11175 - 11325	4.755	4.816	4.765	4.712
8	12495 - 12645	4.666	4.609	4.632	4.643
9	14475 - 14625	4.907	4.808	4.842	4.882
10	15795 - 15945	4.501	4.517	4.487	4.463

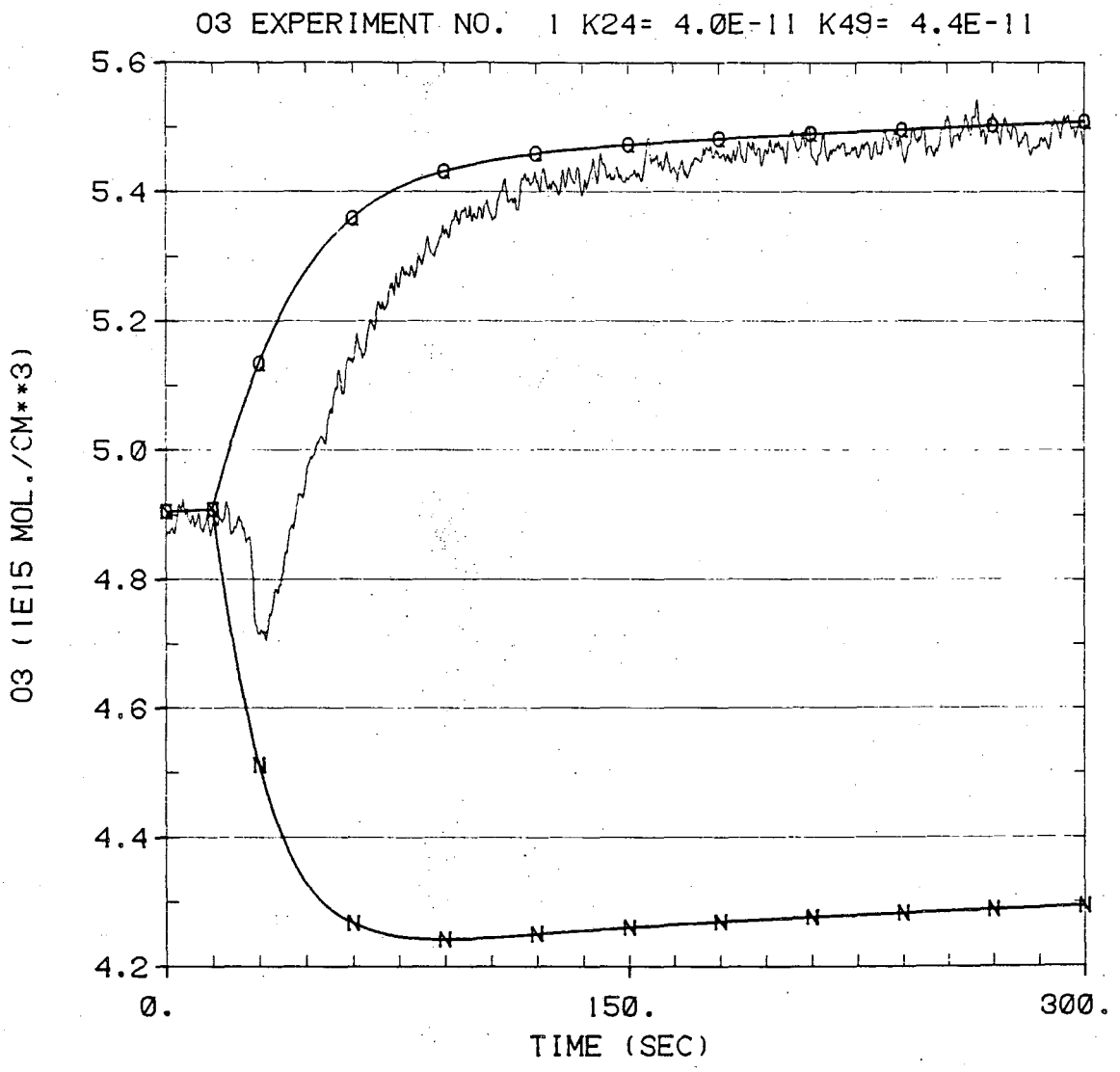

Fig. 29a. Experiment 1 observed and calculated O_3 profiles slow k_{24}.
Curve Q: calculated using optimum k_{49} value (Quenching).
Curve N: calculated using k_{49} = 0 (No quenching).

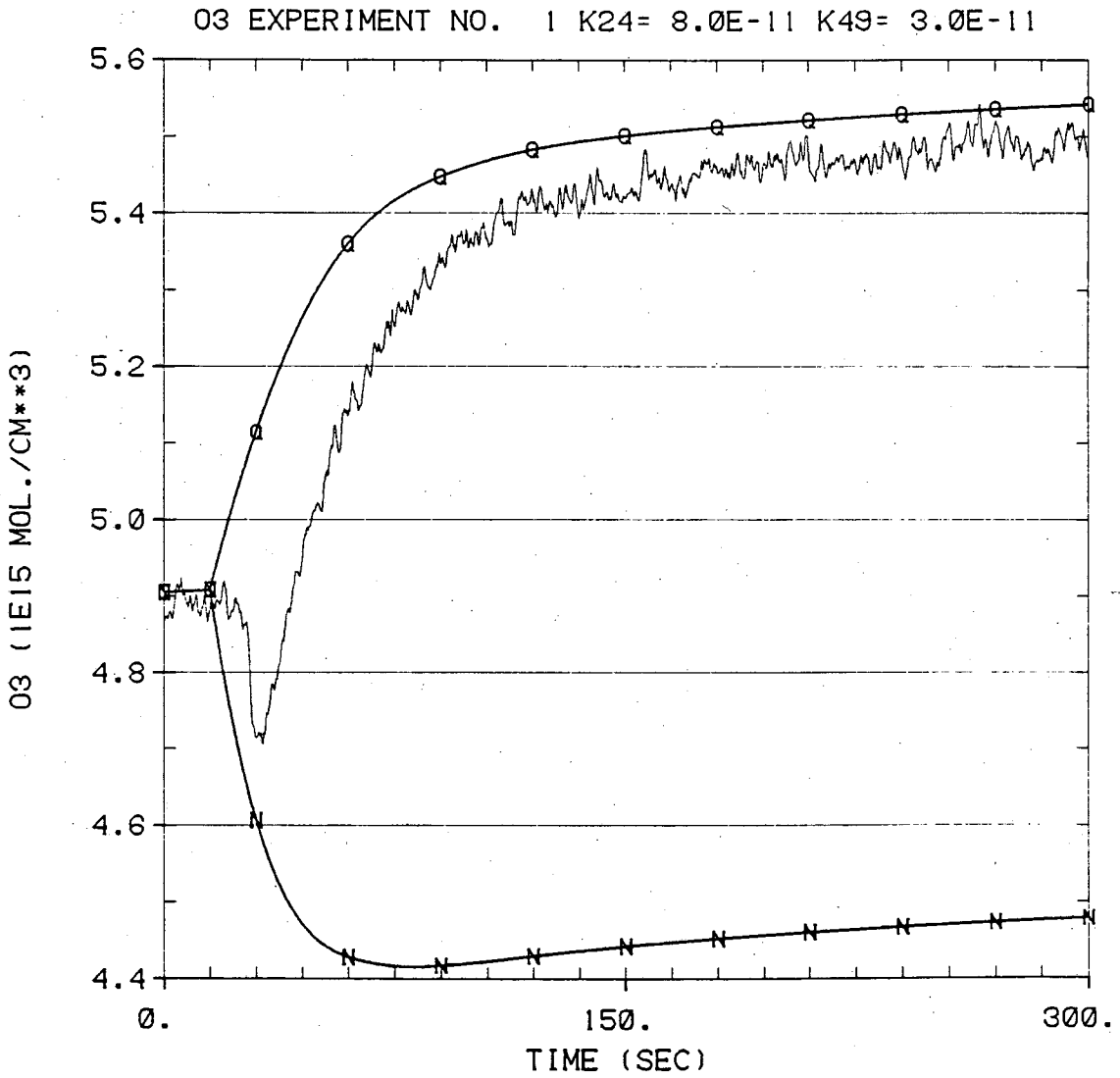

XBL 817-10919

Fig. 29b. Experiment 1 observed and calculated O_3 profiles medium k_{24}.

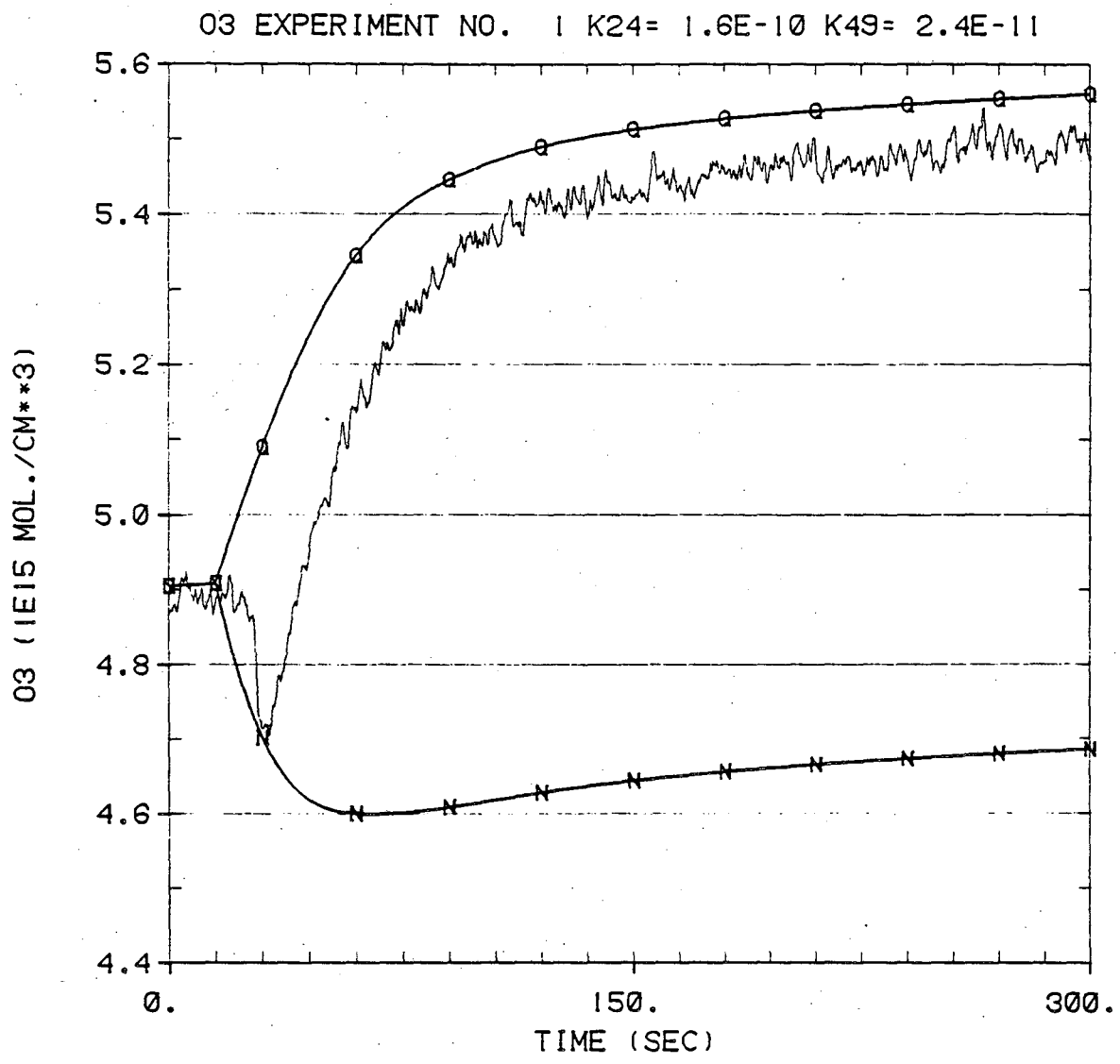

Fig. 29c. Experiment 1 observed and calculated O_3 profiles fast k_{24}.

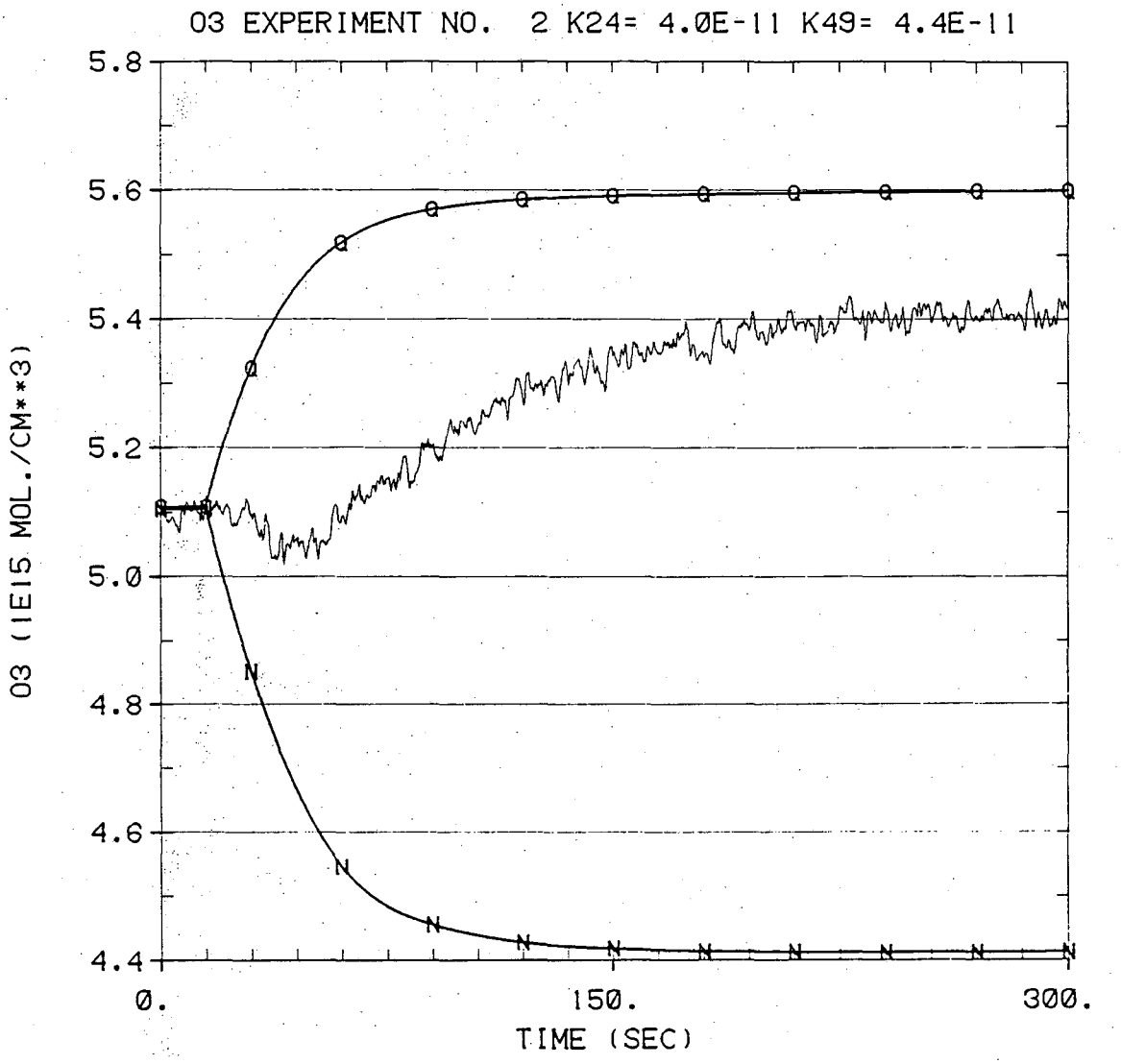

Fig. 30a. Experiment 2 observed and calculated O_3 profiles slow k_{24}.

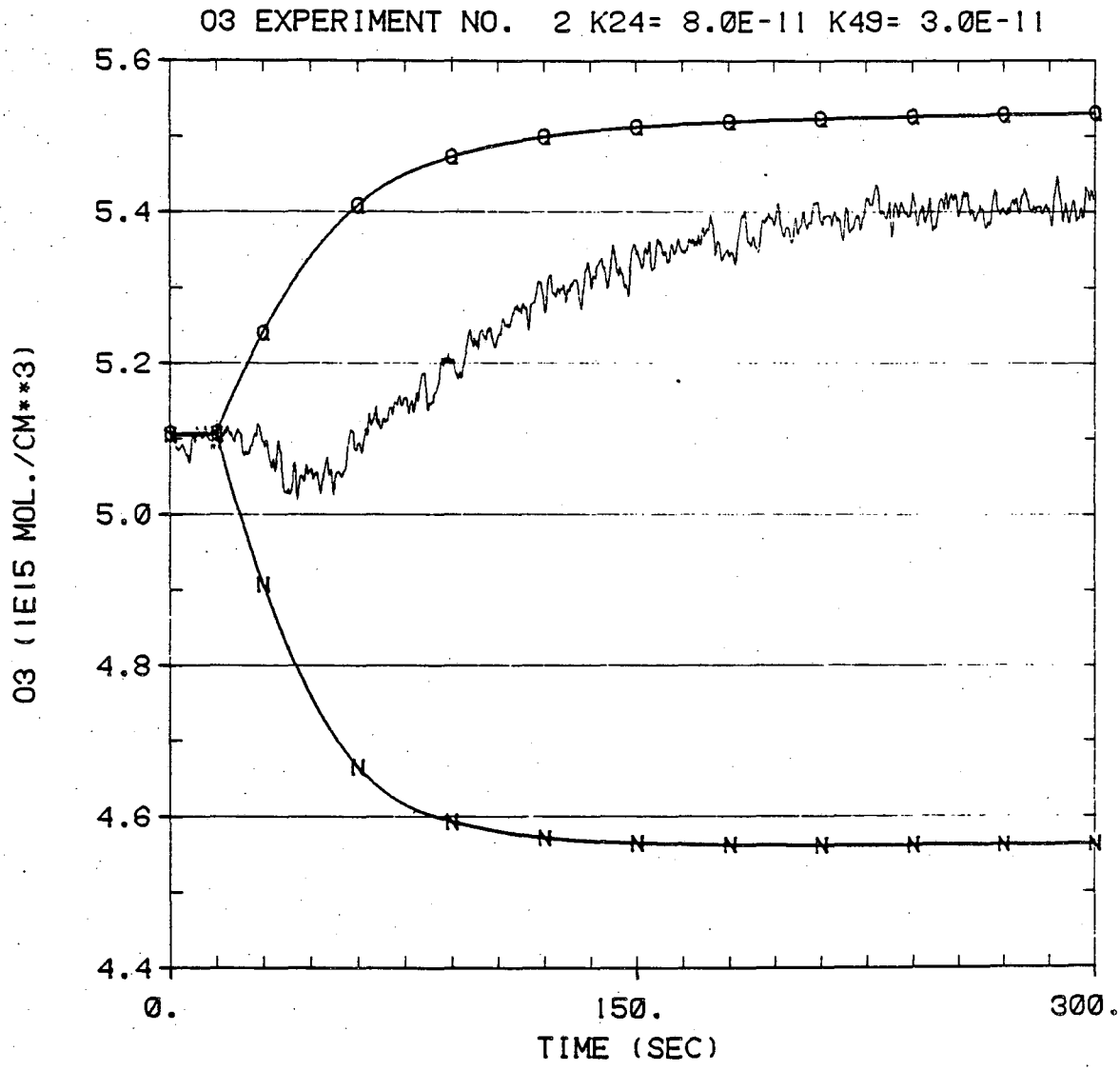

Fig. 30b. Experiment 2 observed and calculated O_3 profiles medium k_{24}.

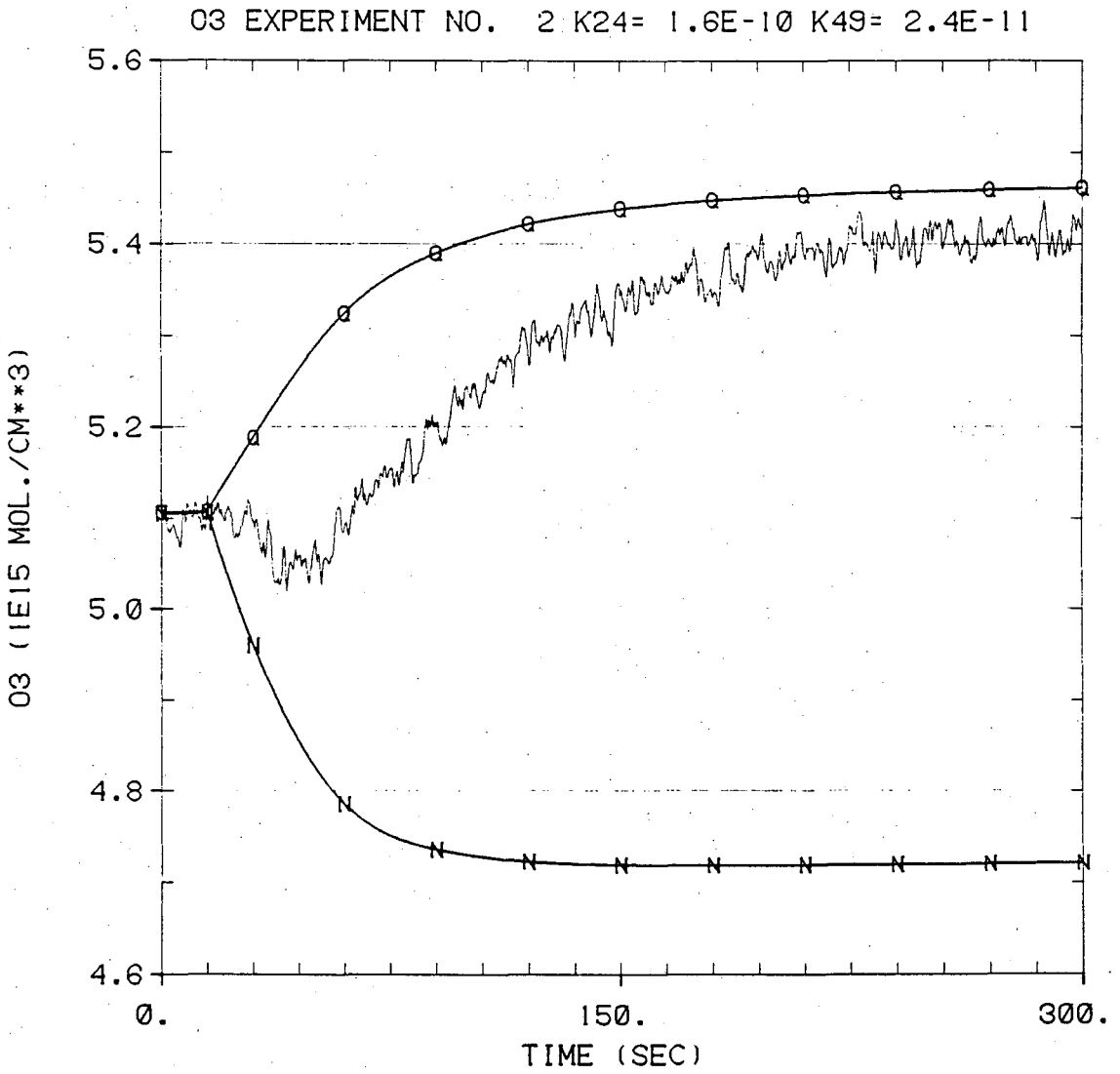

XBL 817-10923

Fig. 30c. Experiment 2 observed and calculated O_3 profiles fast k_{24}.

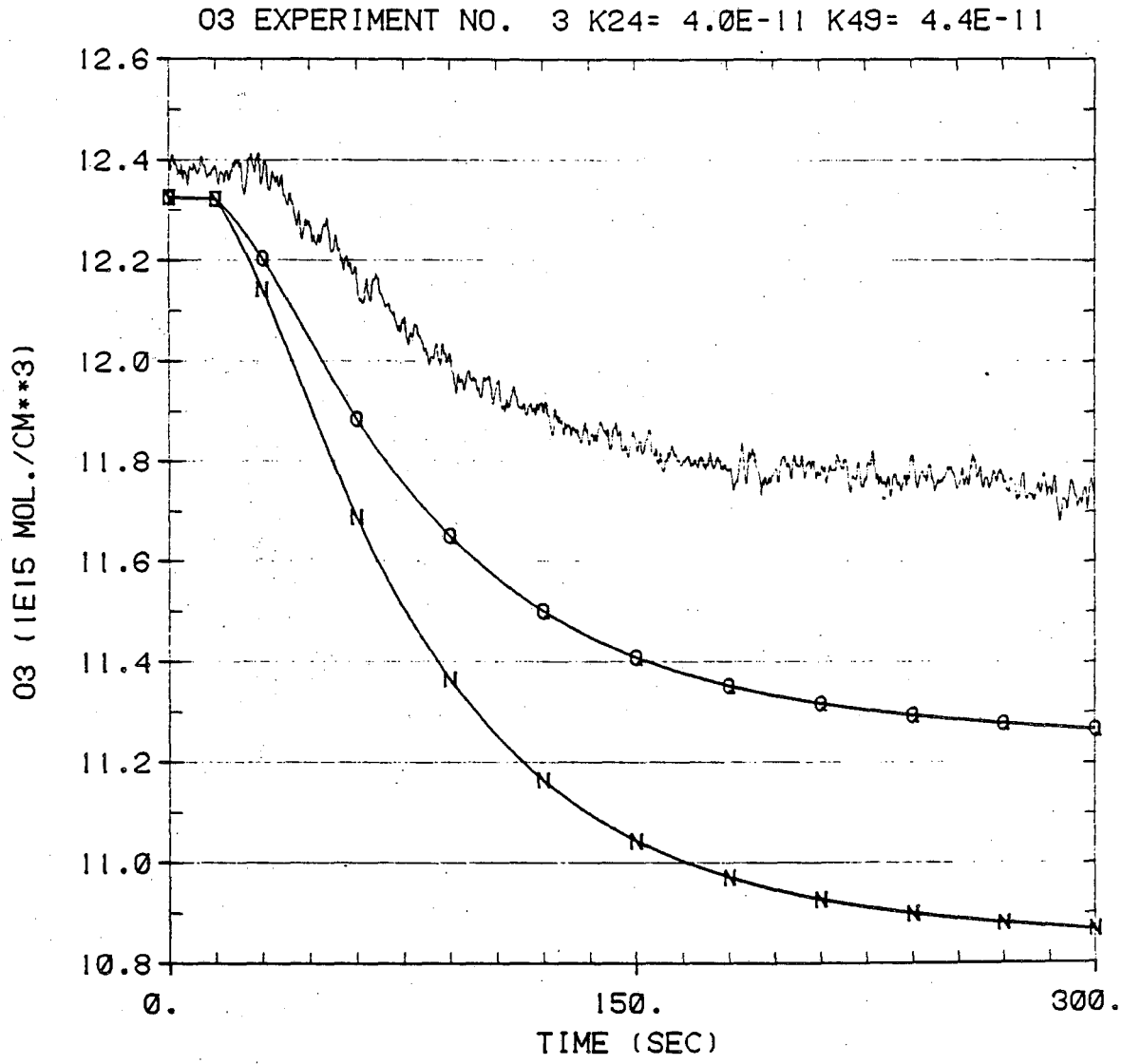

Fig. 31a. Experiment 3 observed and calculated O_3 profiles slow k_{24}.

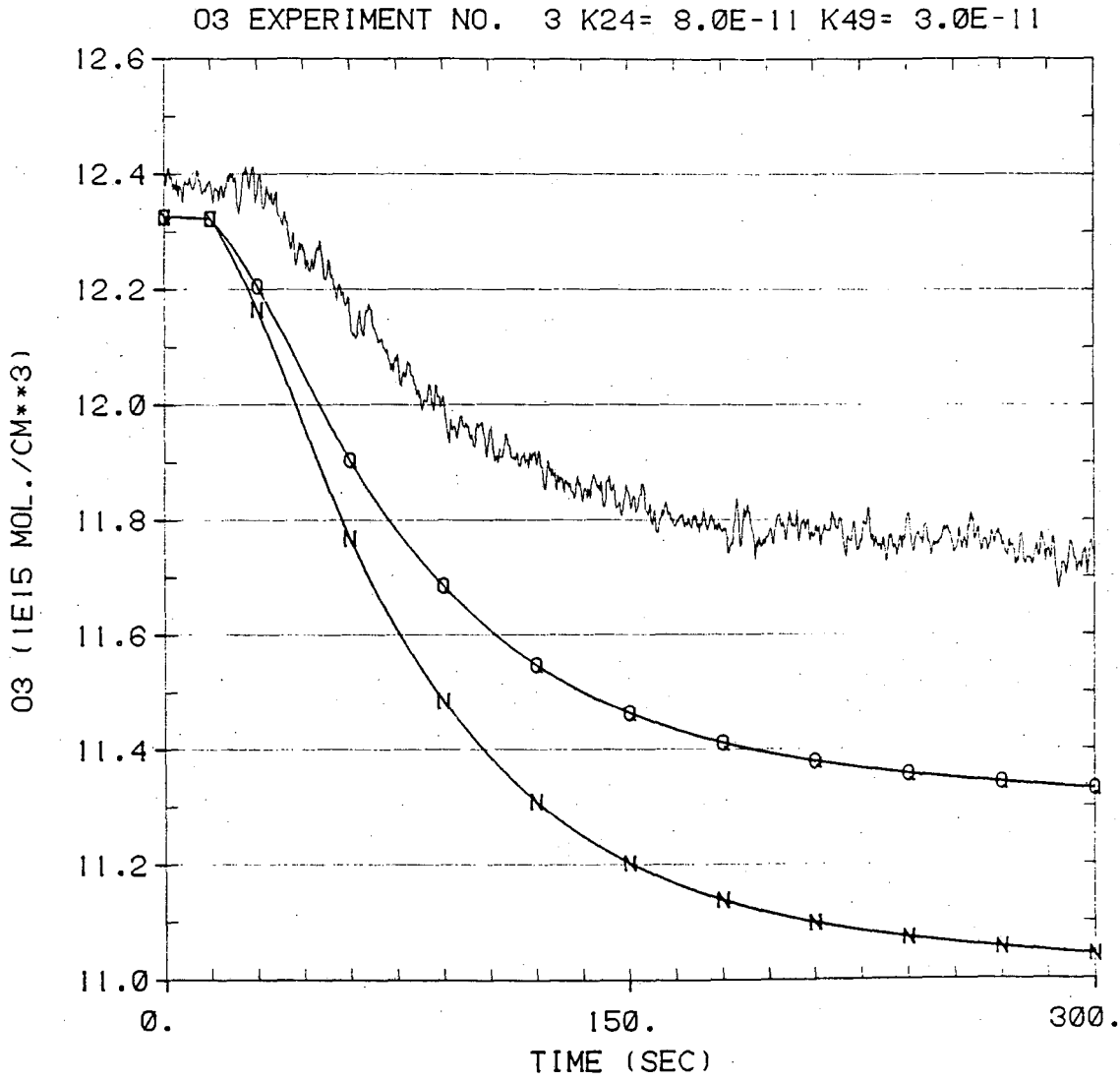

Fig. 31b. Experiment 3 observed and calculated O_3 profiles medium k_{24}.

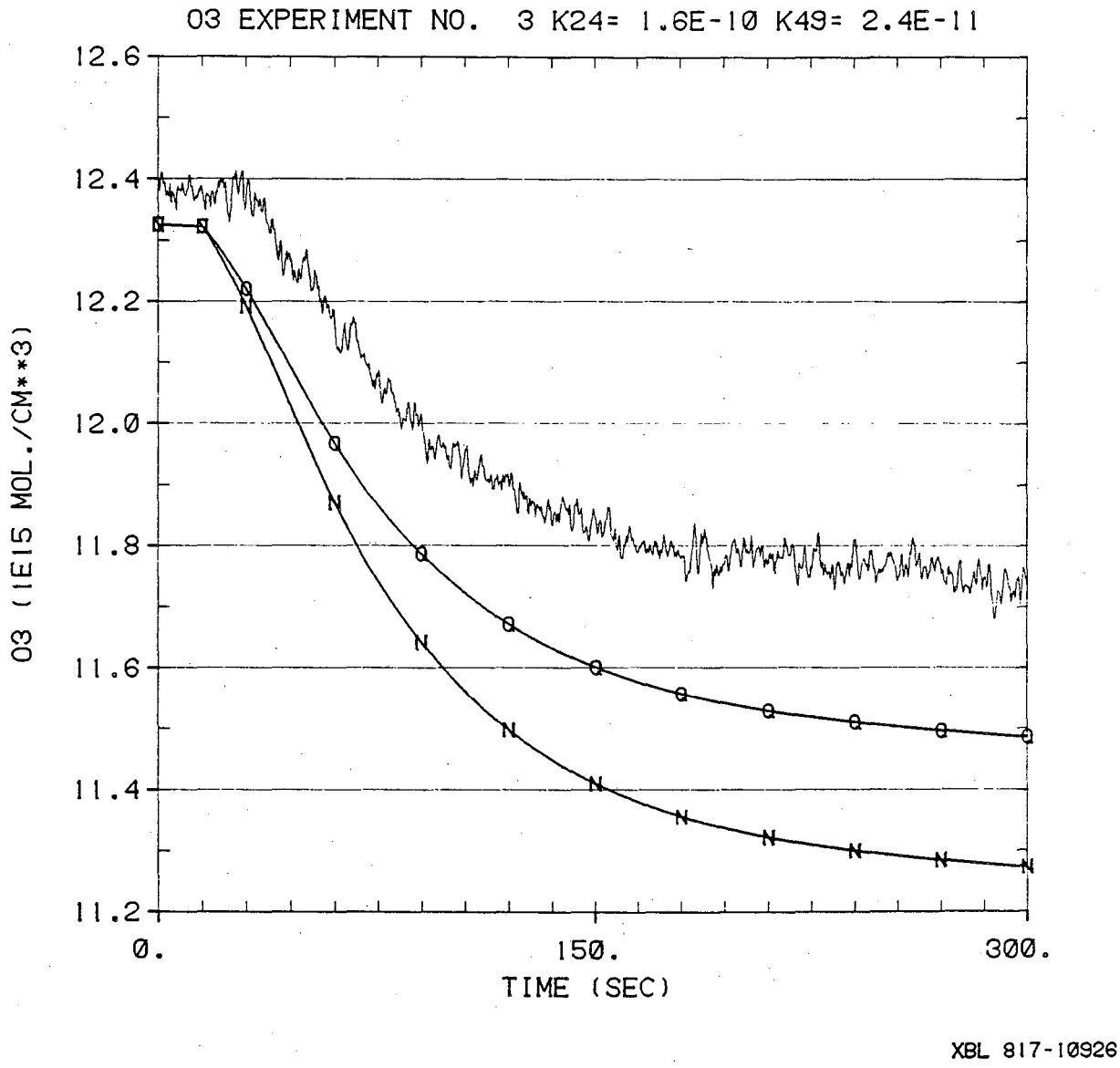

Fig. 31c. Experiment 3 observed and calculated O_3 profiles fast k_{24}.

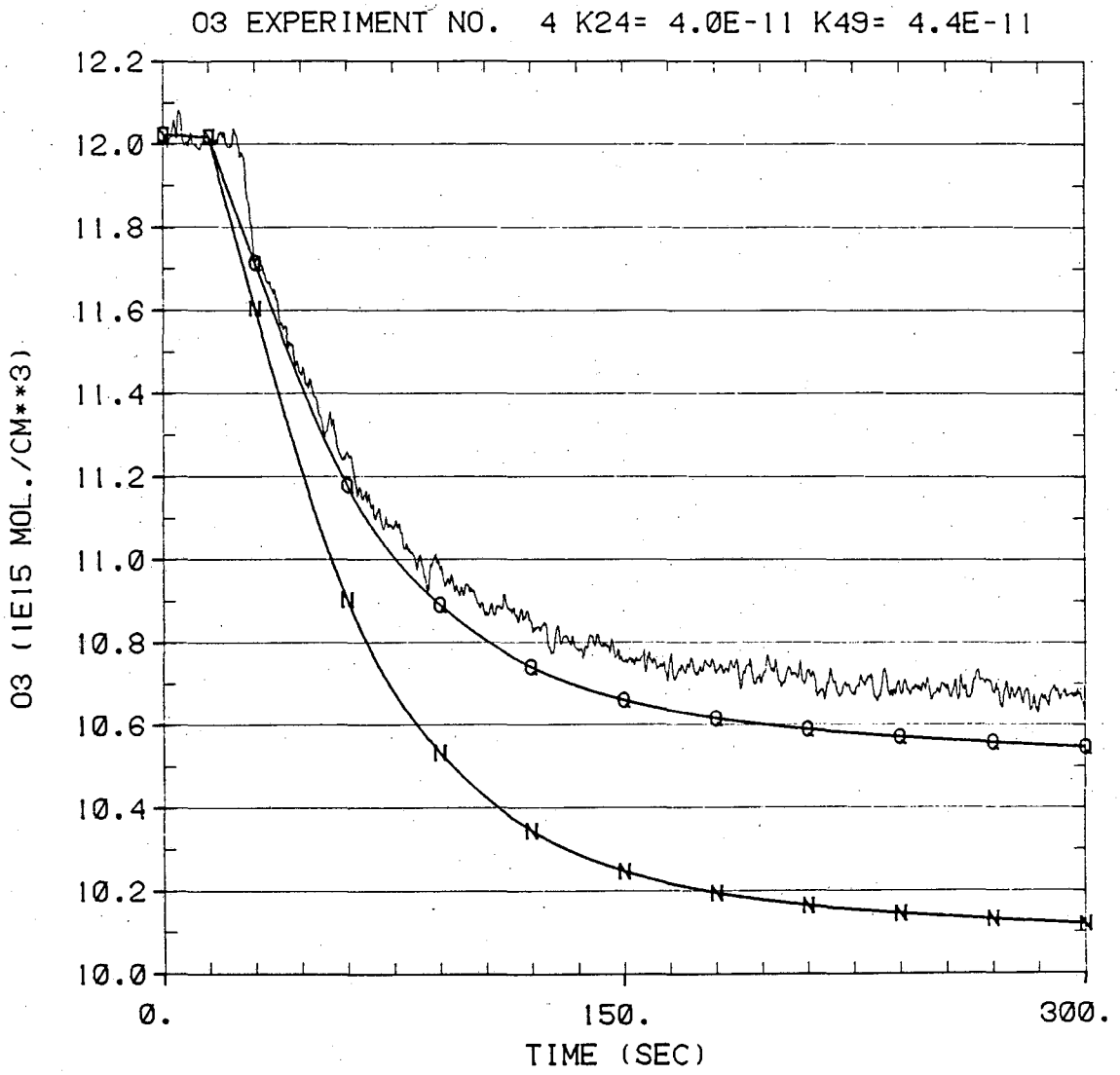

Fig. 32a. Experiment 4 observed and calculated O_3 profiles slow k_{24}.

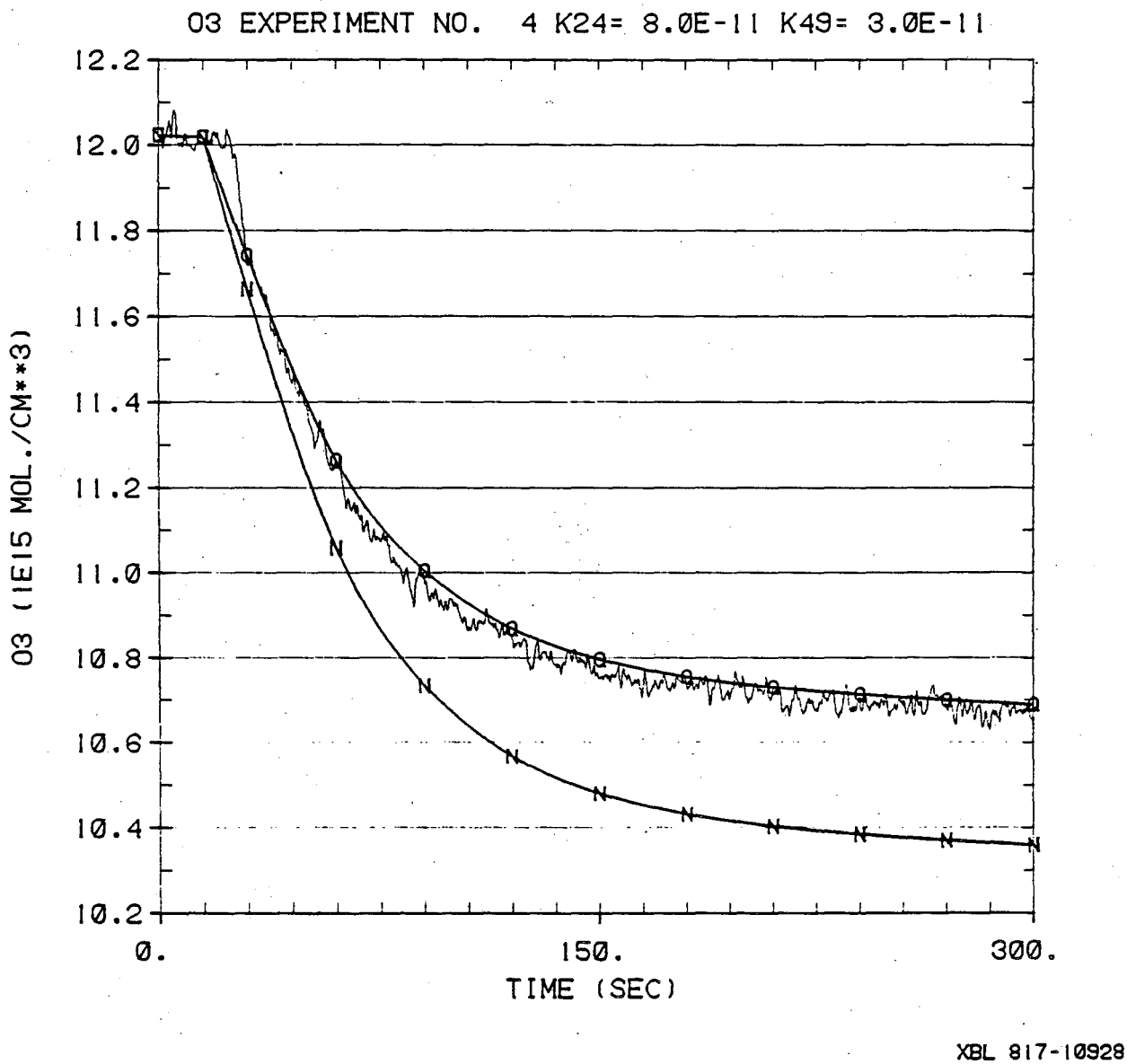

Fig. 32b. Experiment 4 observed and calculated O_3 profiles medium k_{24}.

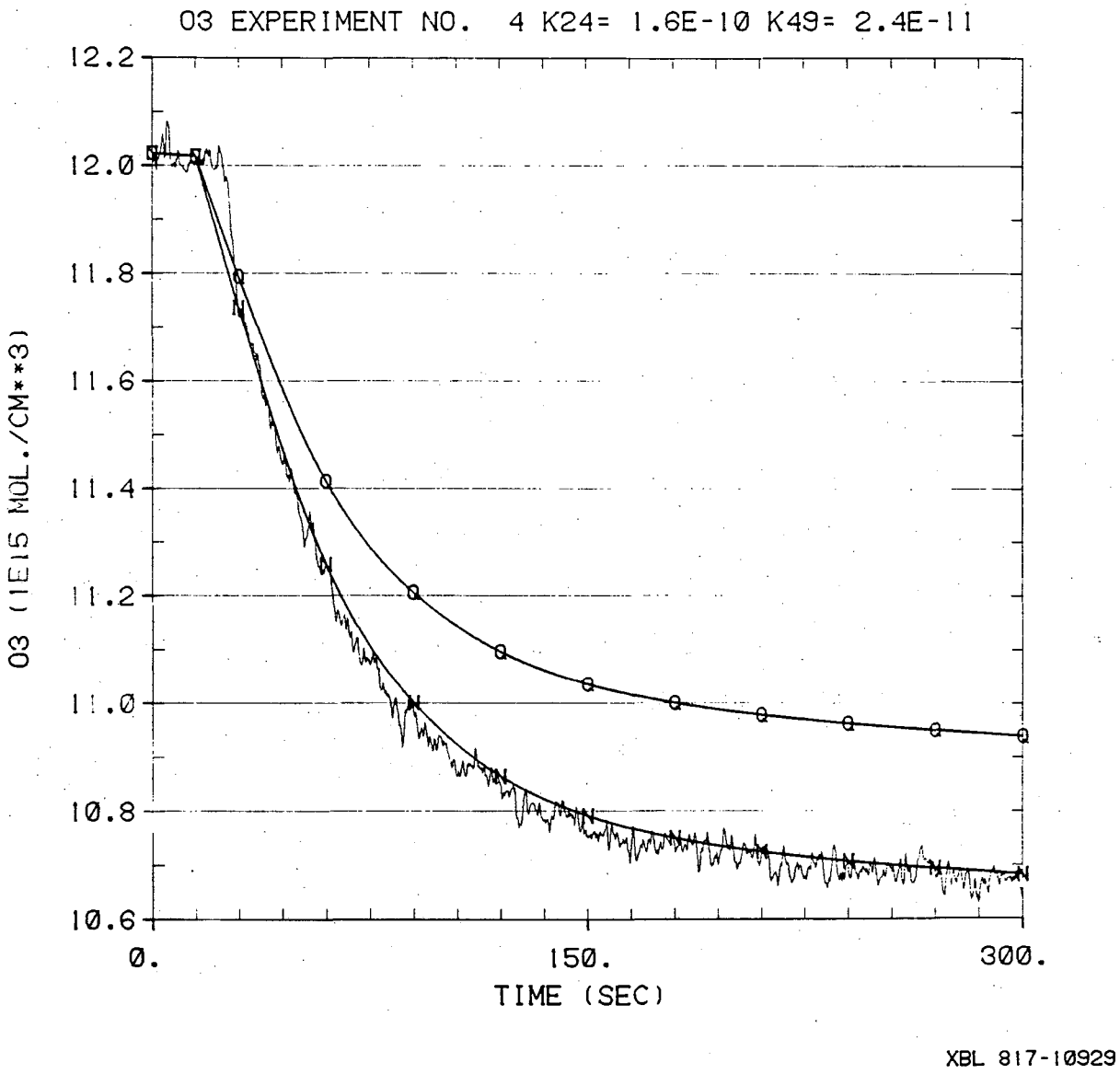

Fig. 32c. Experiment 4 observed and calculated O_3 profiles fast k_{24}.

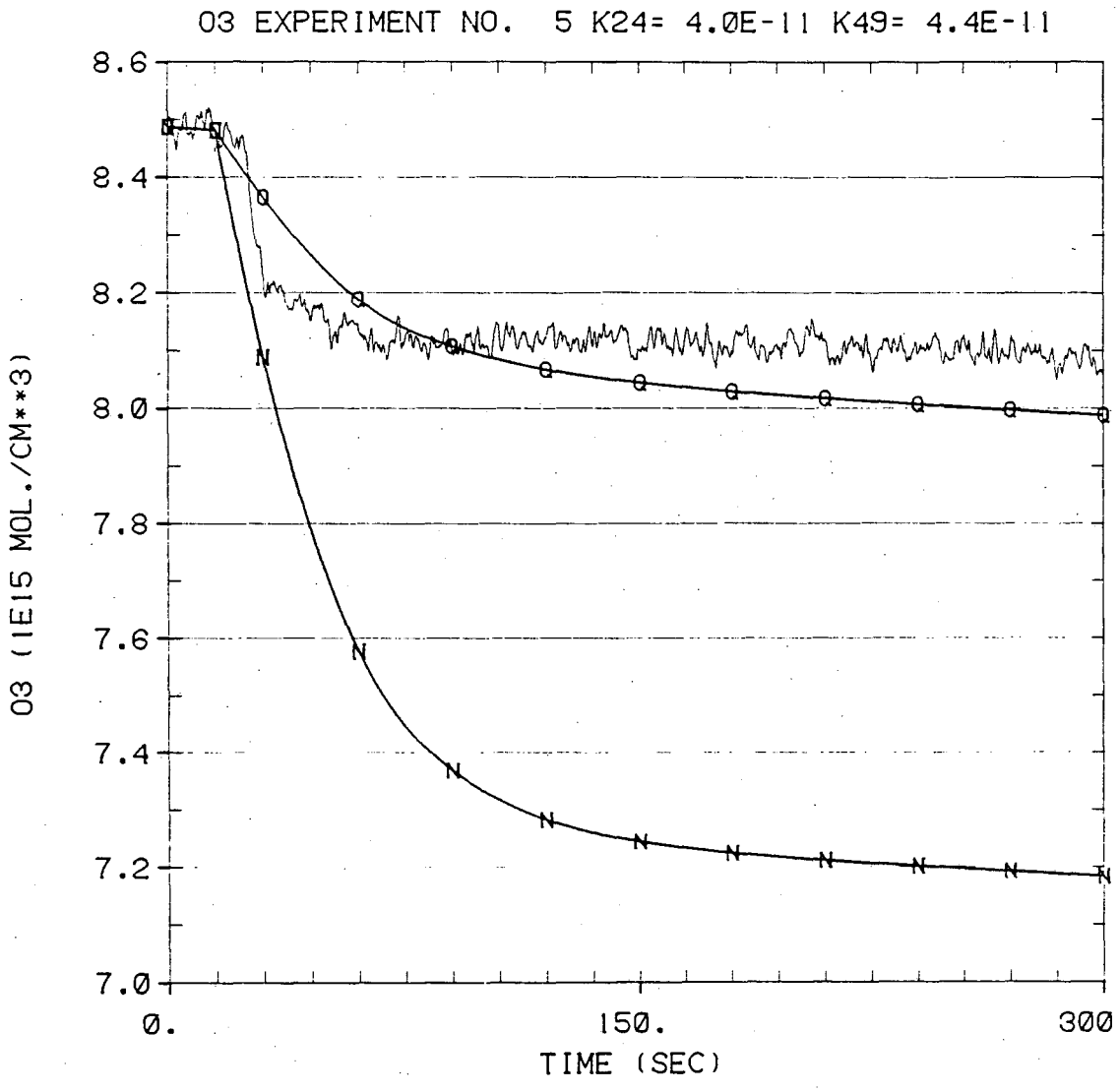

Fig. 33a. Experiment 5 observed and calculated O_3 profiles slow k_{24}.

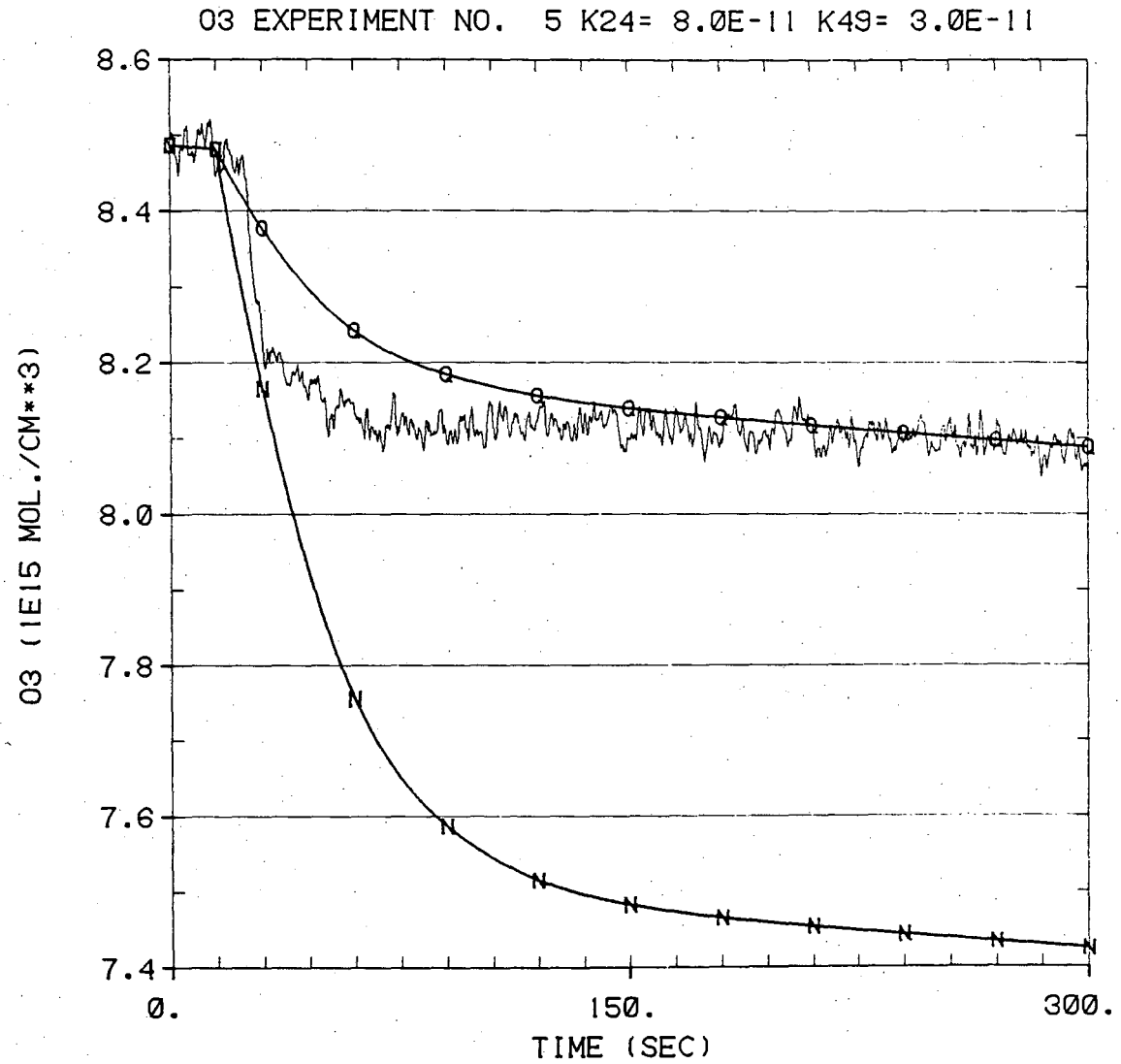

XBL 817-10931

Fig. 33b. Experiment 5 observed and calculated O_3 profiles medium k_{24}.

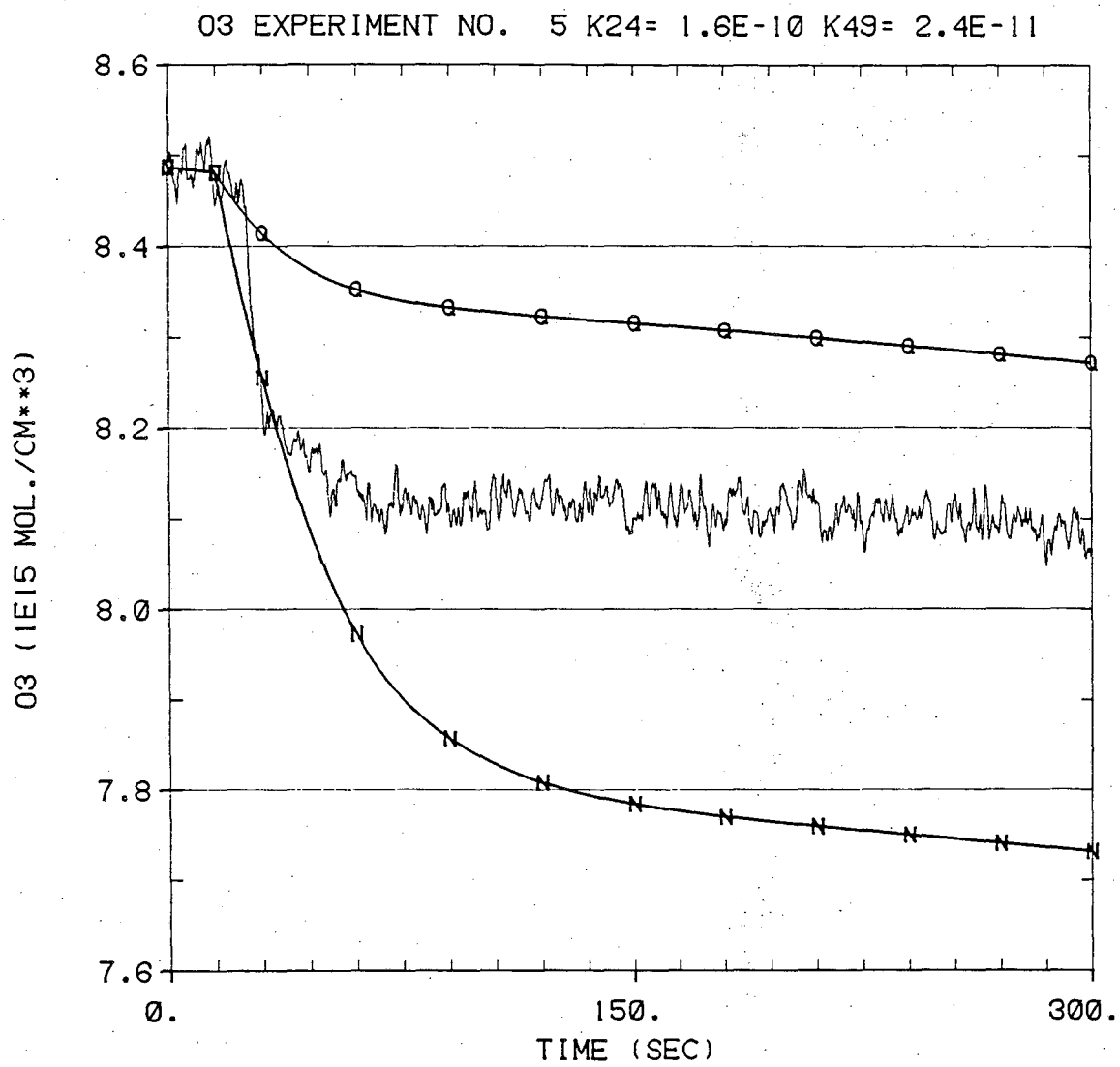

Fig. 33c. Experiment 5 observed and calculated O_3 profiles fast k_{24}.

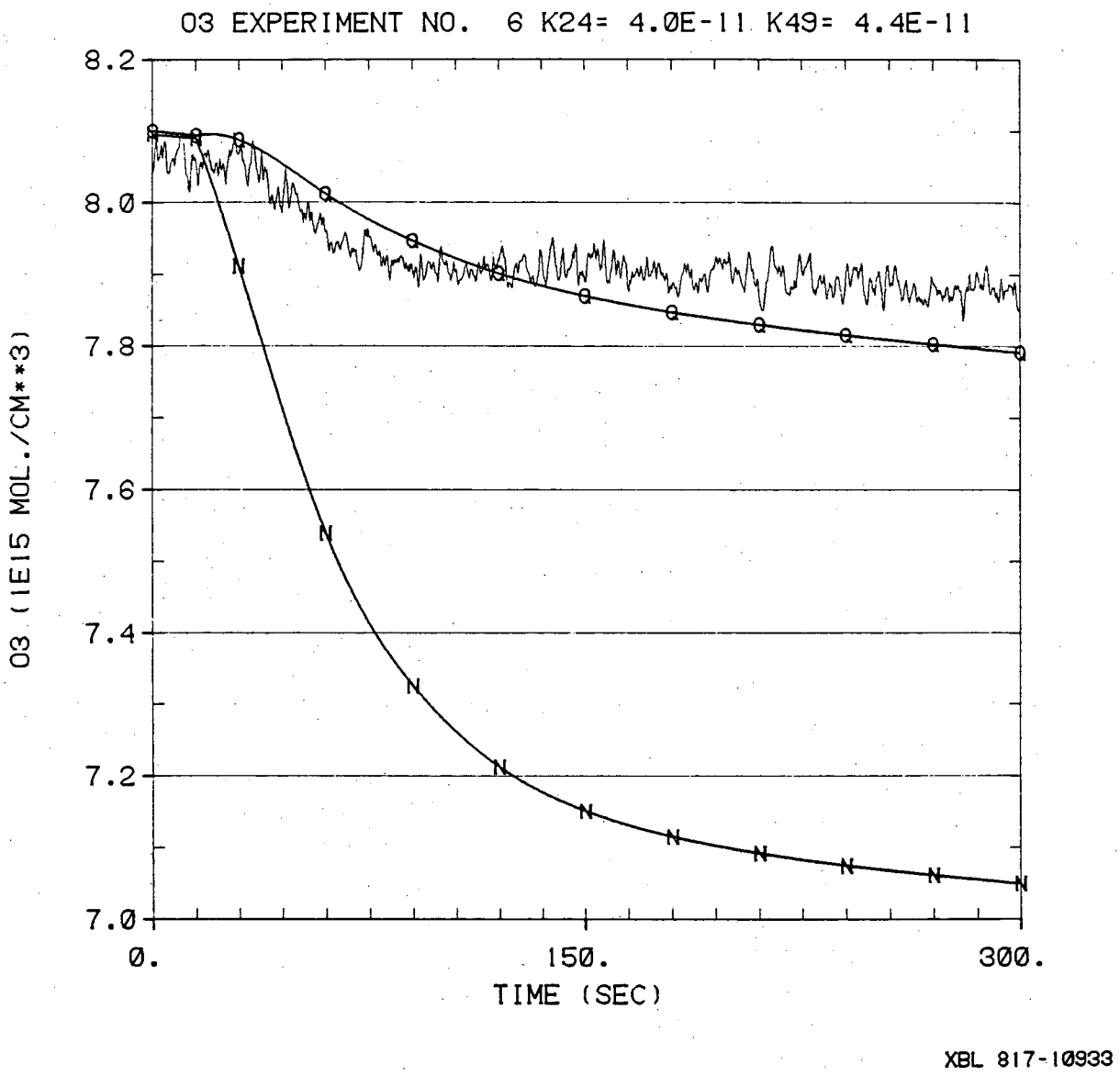

Fig. 34a. Experiment 6 observed and calculated O_3 profiles slow k_{24}.

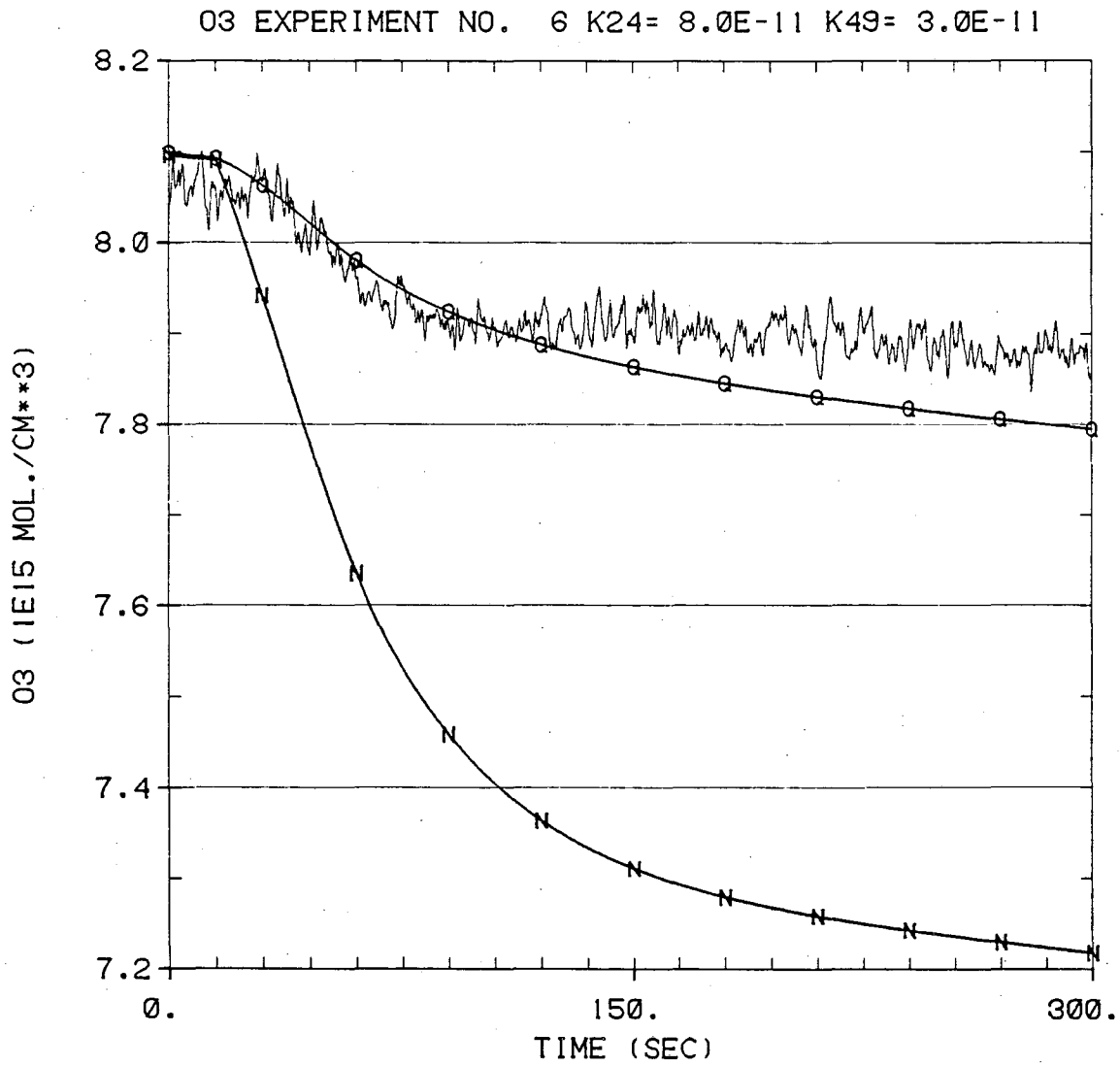

Fig. 34b. Experiment 6 observed and calculated O_3 profiles medium k_{24}.

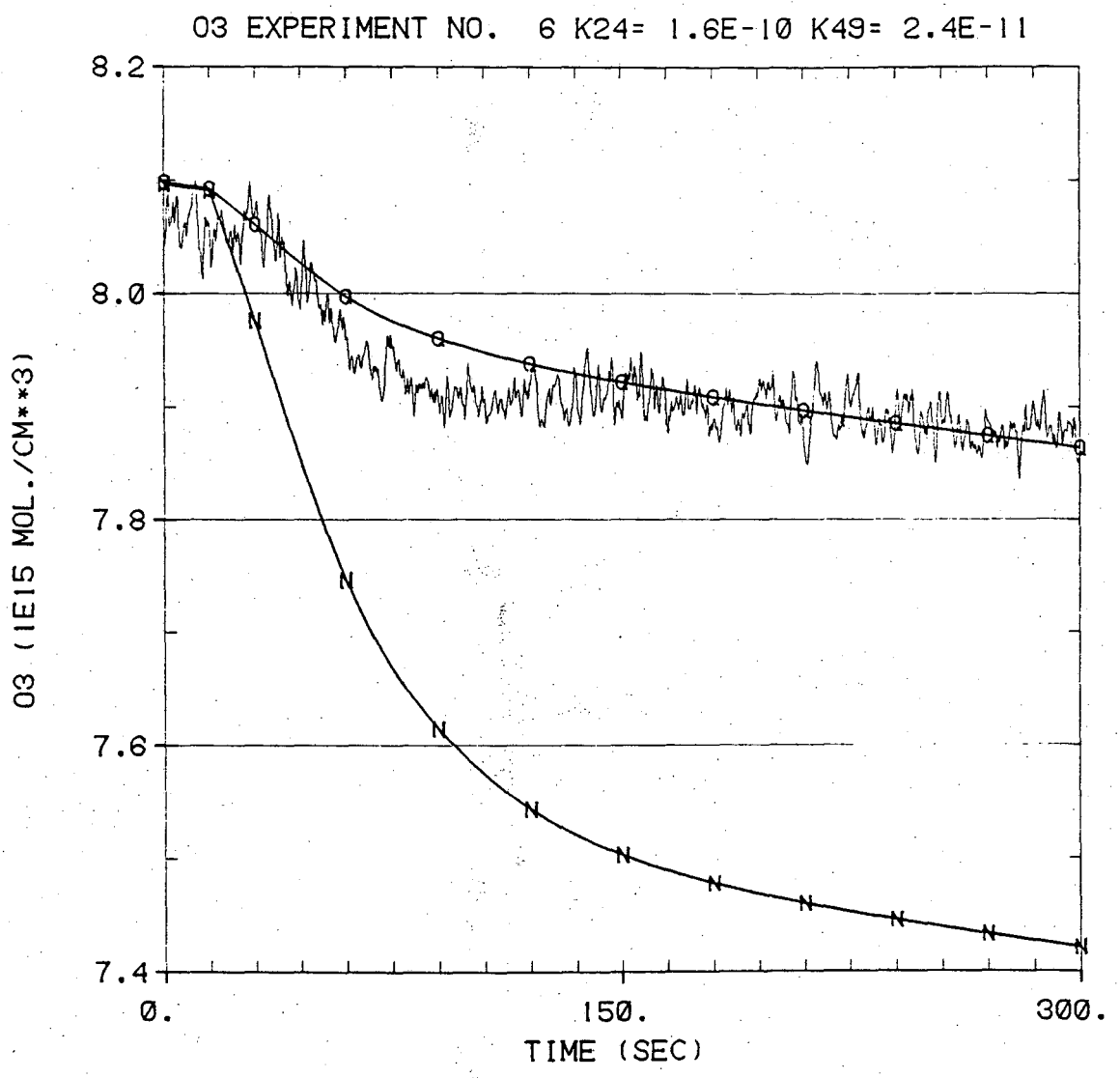

Fig. 34c. Experiment 6 observed and calculated O_3 profiles fast k_{24}.

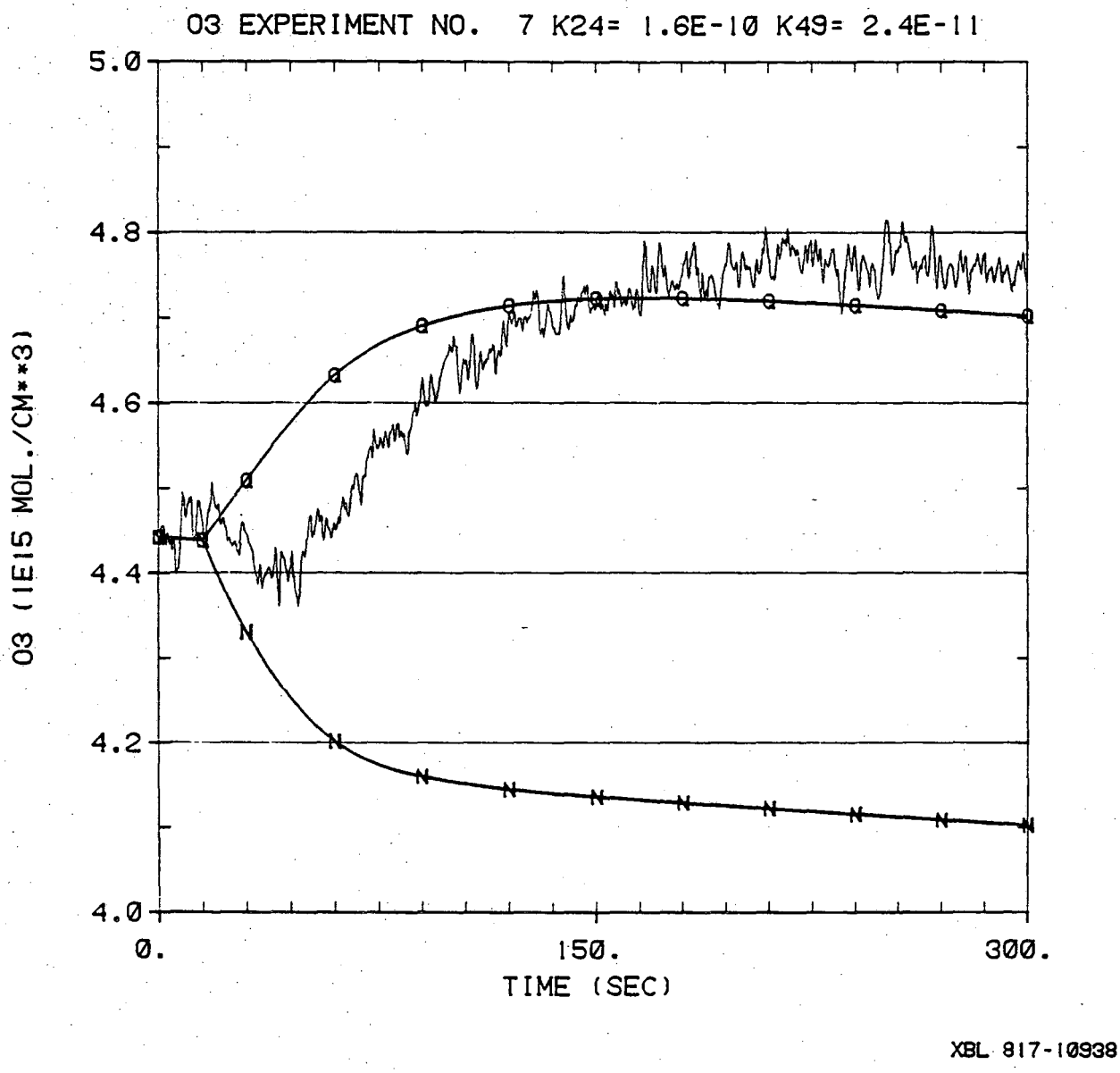

Fig. 35c. Experiment 7 observed and calculated O_3 profiles fast k_{24}.

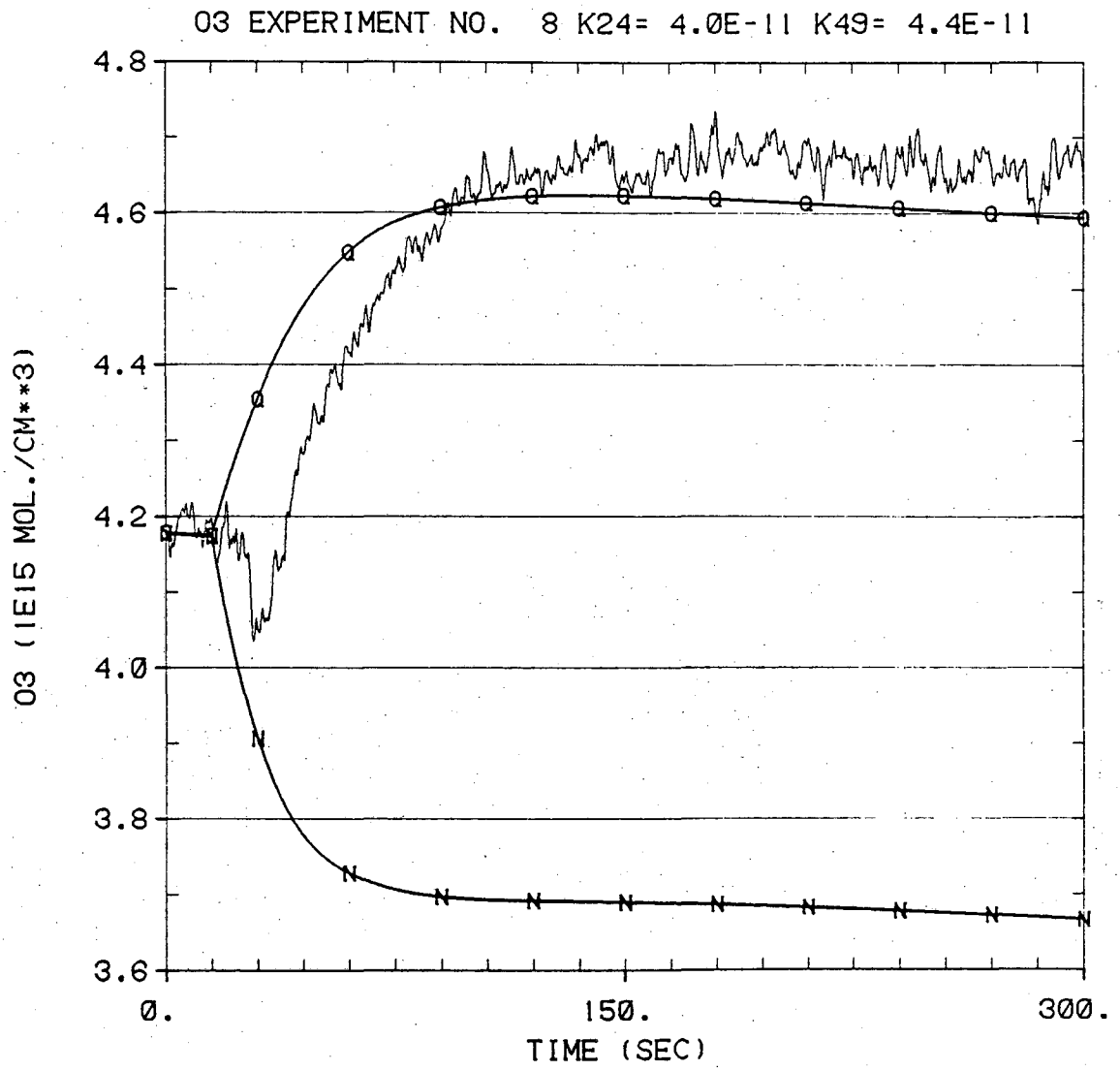

Fig. 36a. Experiment 8 observed and calculated O_3 profiles slow k_{24}.

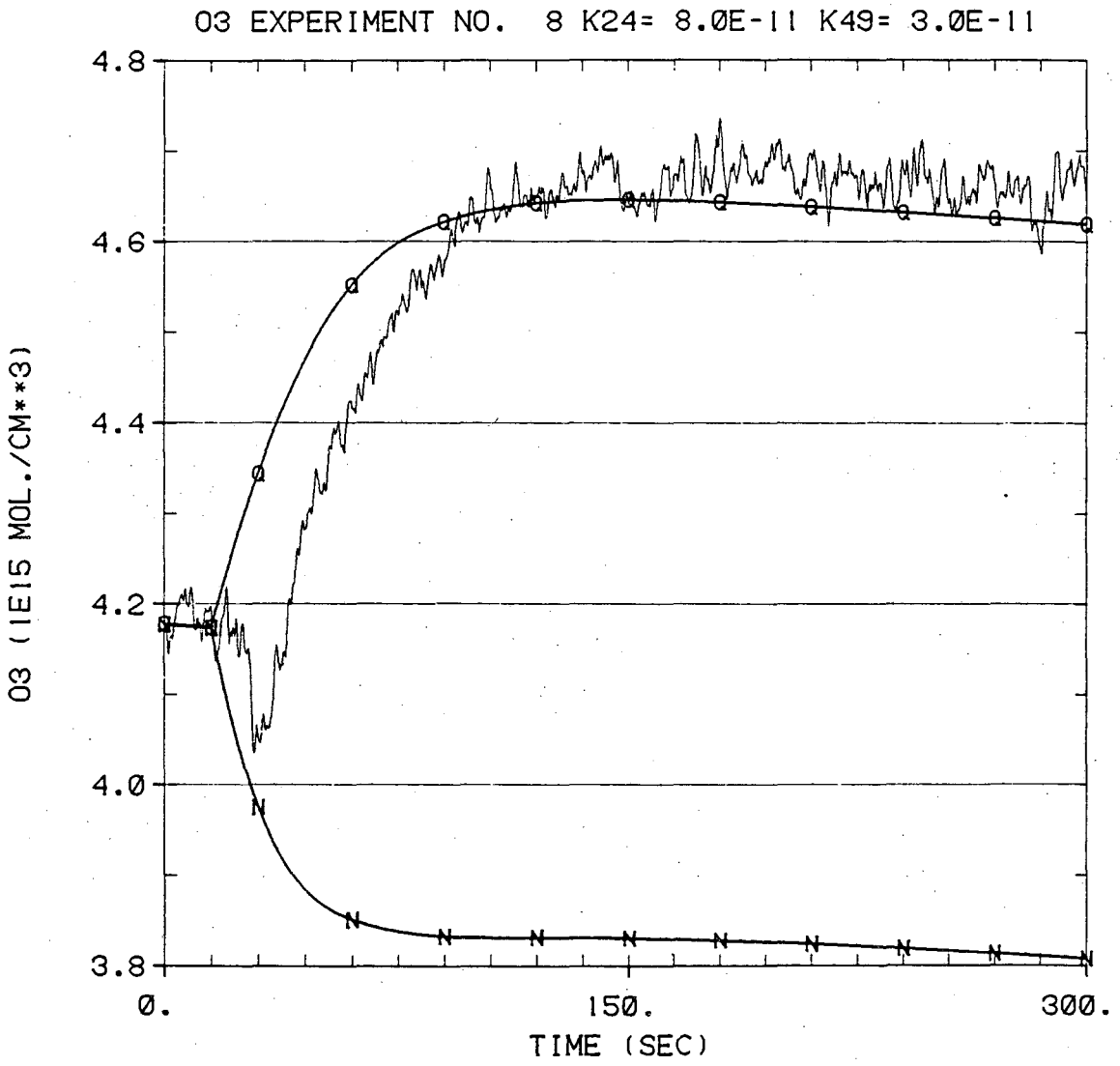

Fig. 36b. Experiment 8 observed and calculated O_3 profiles medium k_{24}.

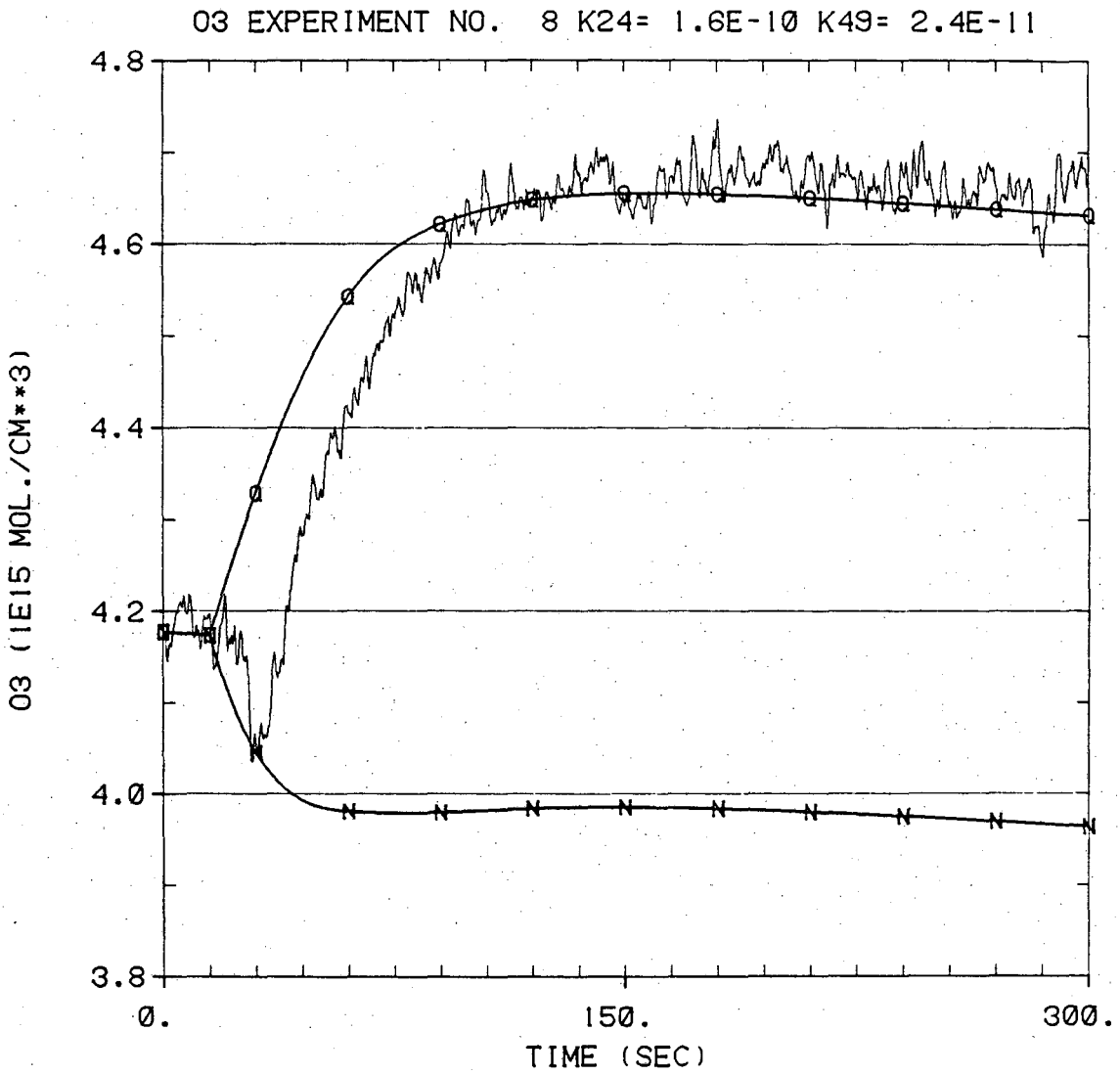

XBL 817-10941

Fig. 36c. Experiment 8 observed and calculated O_3 profiles fast k_{24}.

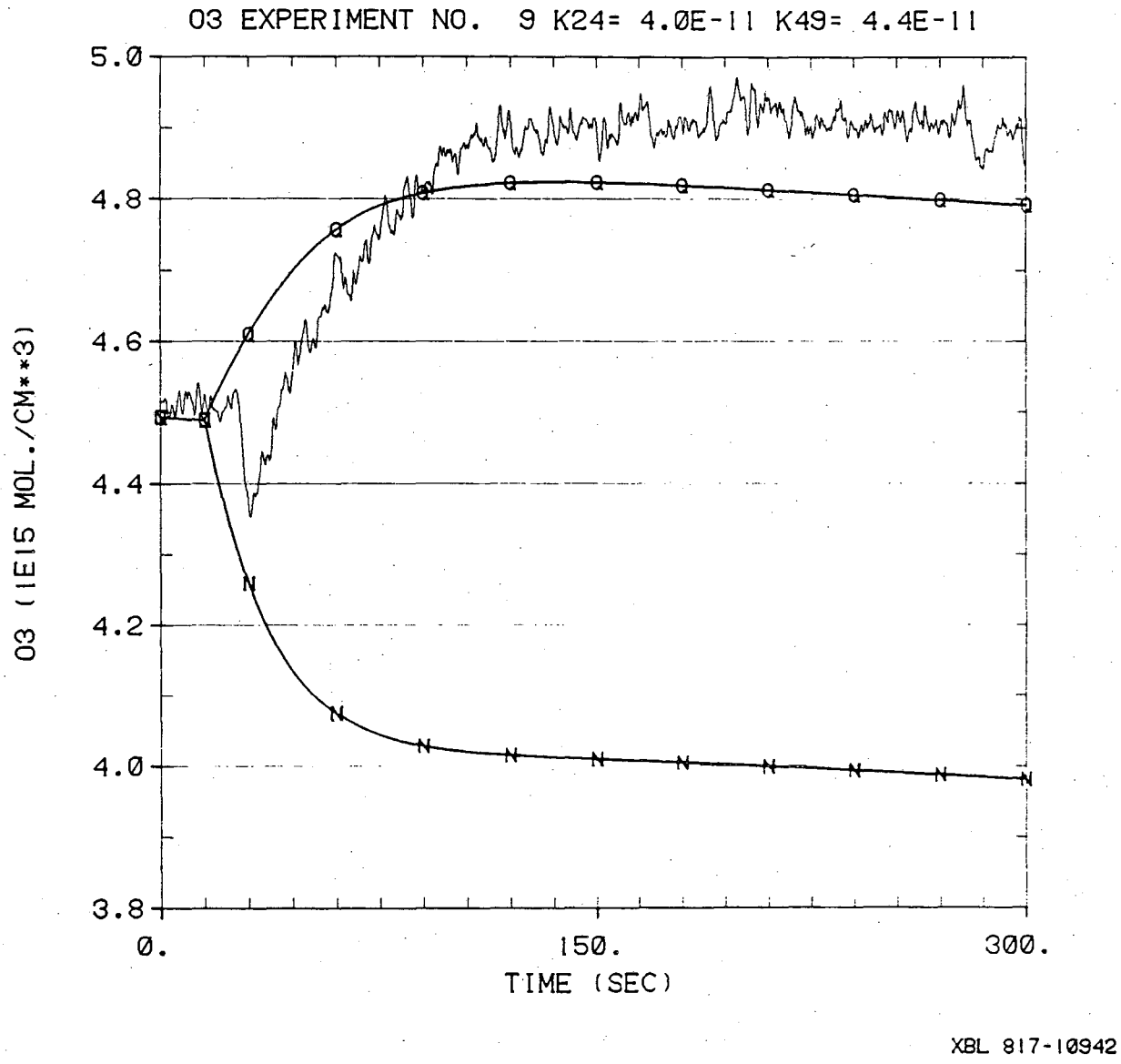

Fig. 37a. Experiment 9 observed and calculated O_3 profiles slow k_{24}.

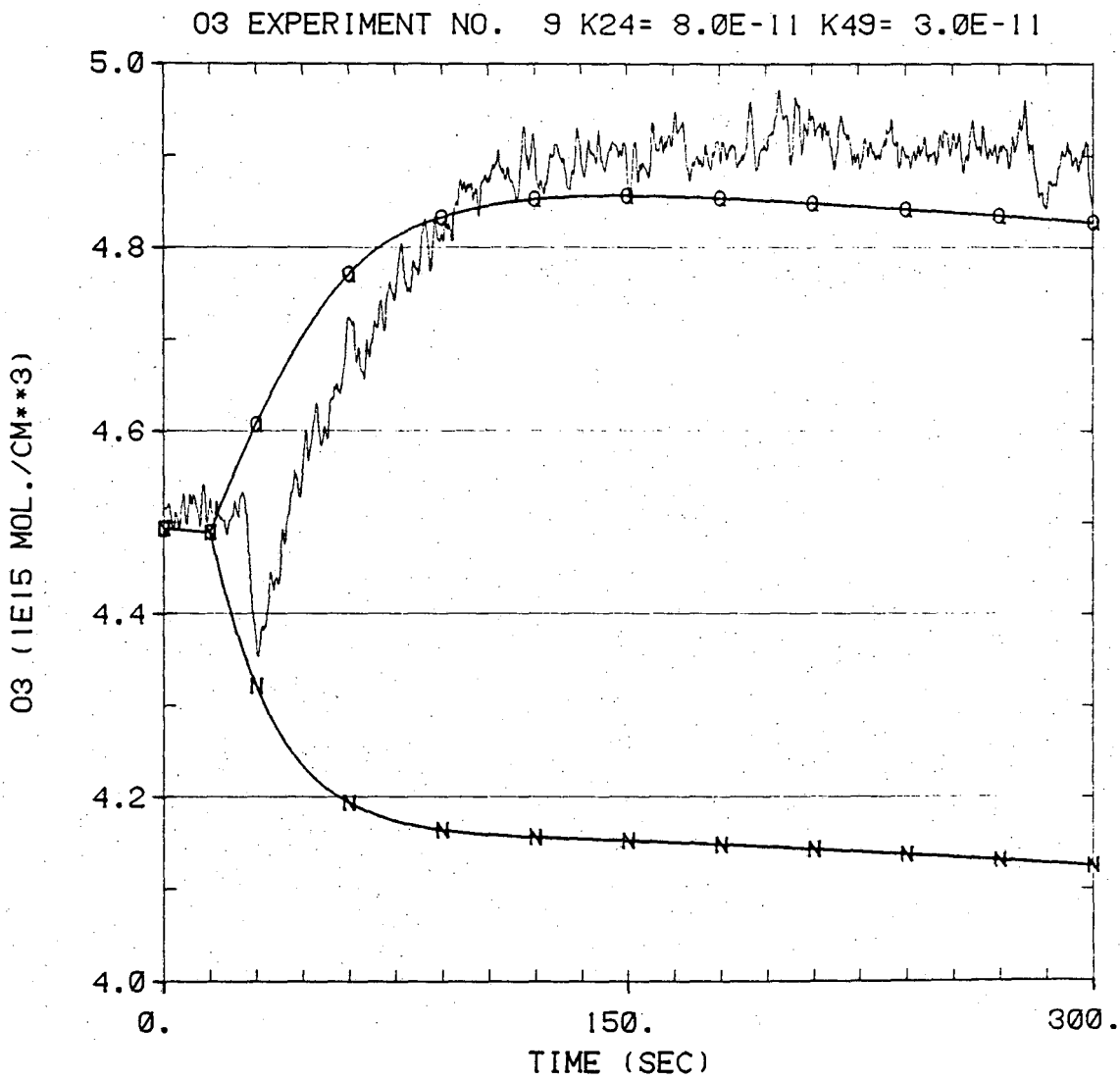

Fig. 37b. Experiment 9 observed and calculated O_3 profiles medium k_{24}.

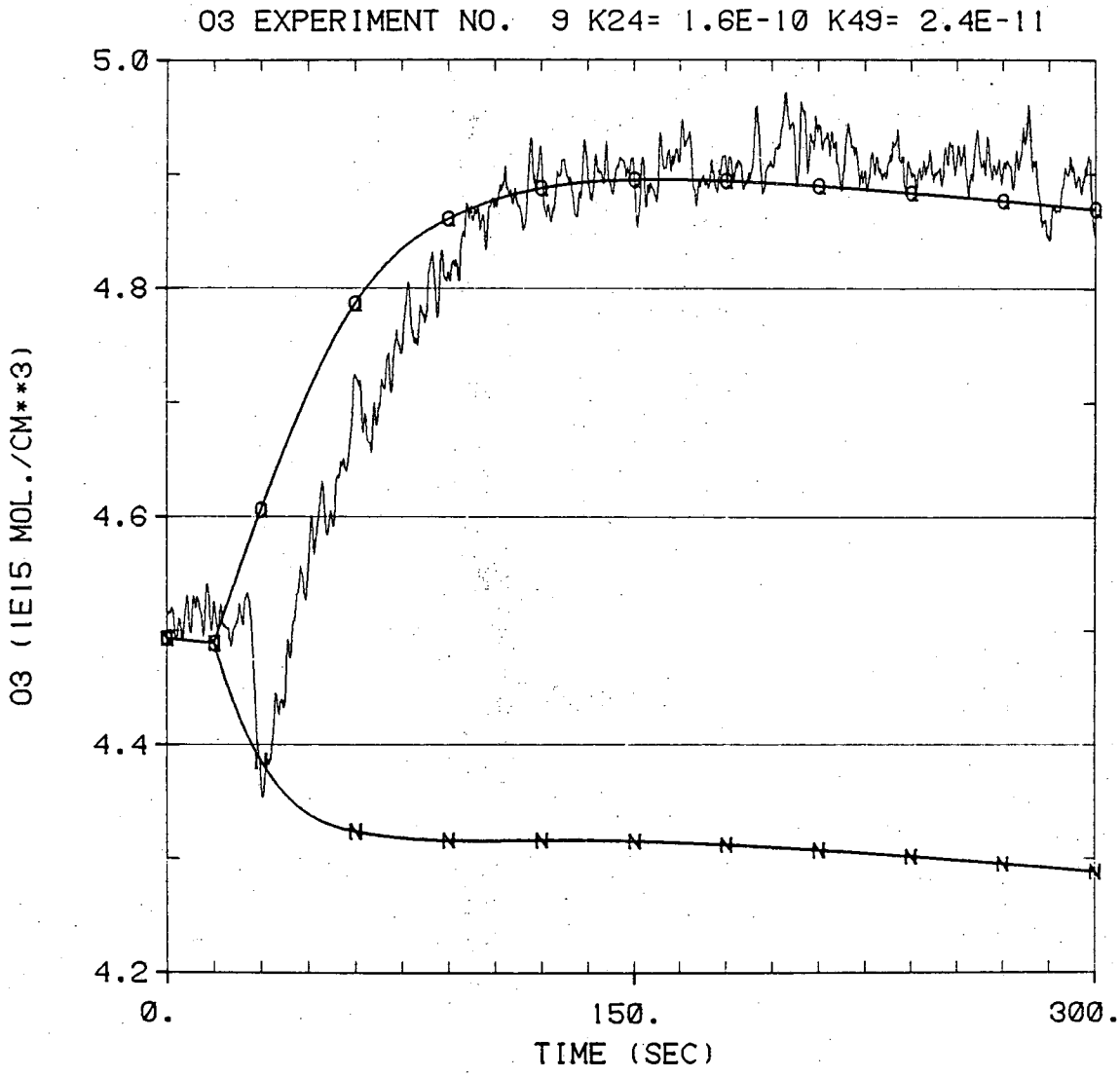

XBL 817-10944

Fig. 37c. Experiment 9 observed and calculated O_3 profiles fast k_{24}.

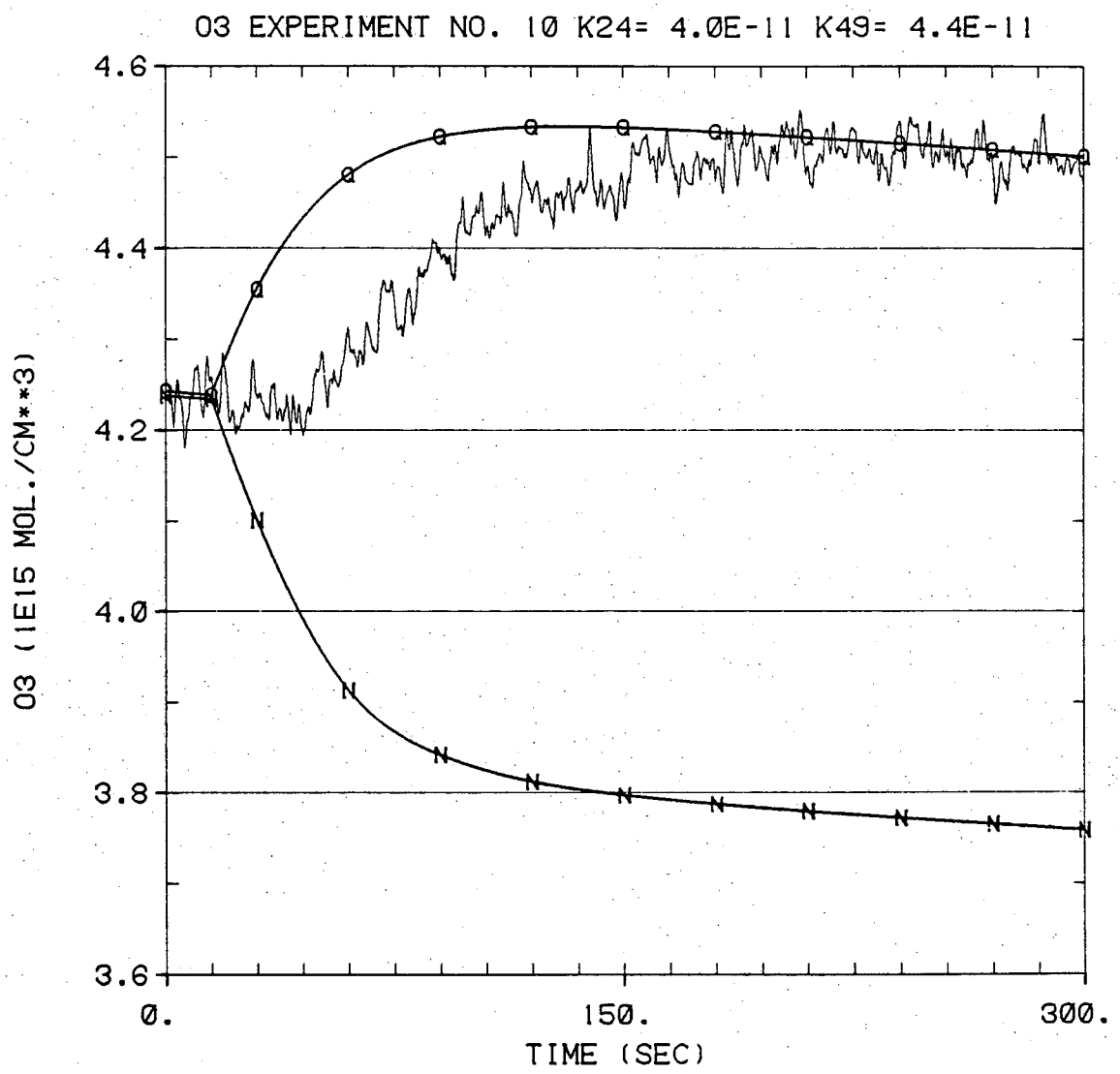

Fig. 38a. Experiment 10 observed and calculated O_3 profiles slow k_{24}.

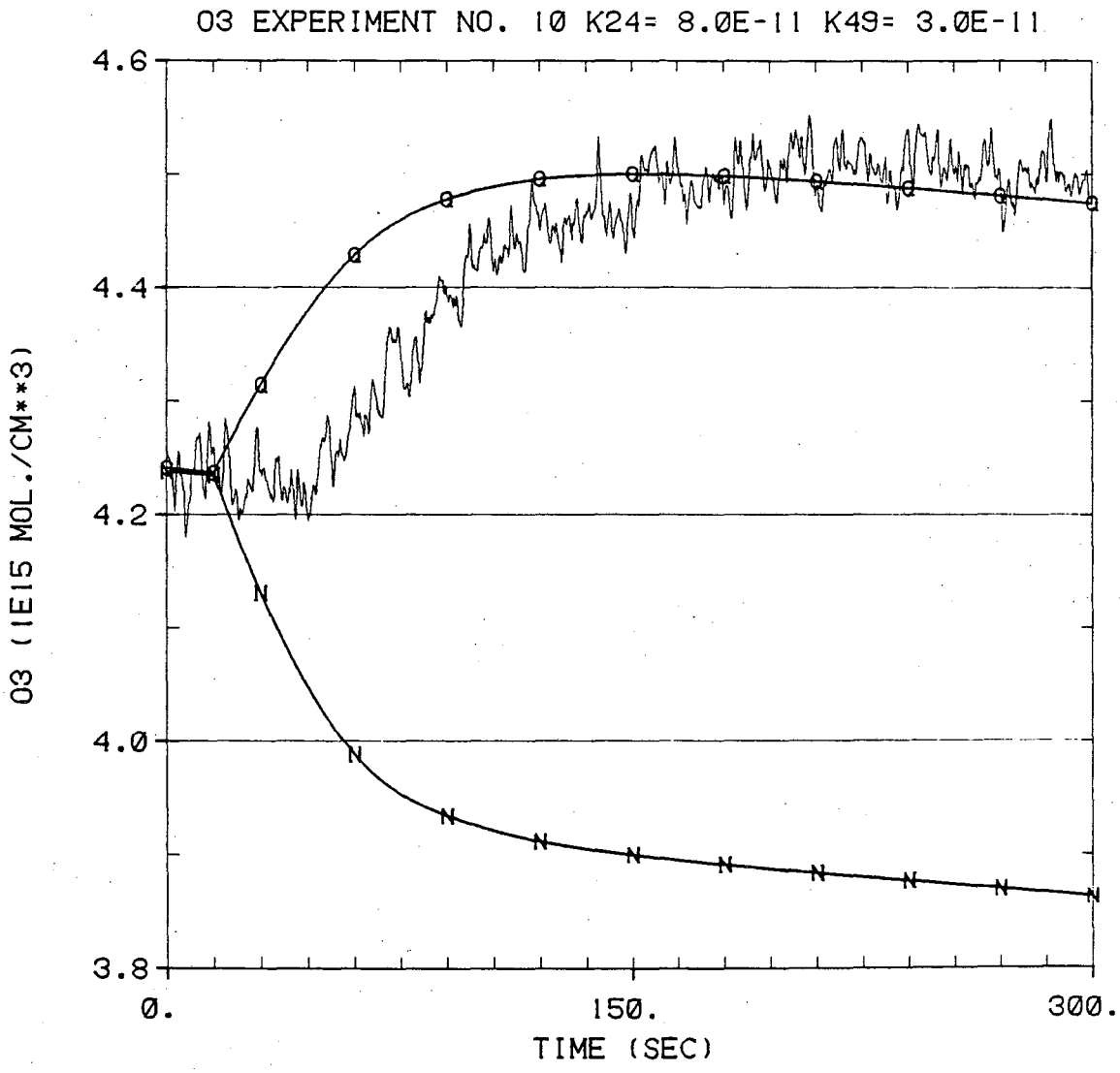

Fig. 38b. Experiment 10 observed and calculated O_3 profiles medium k_{24}.

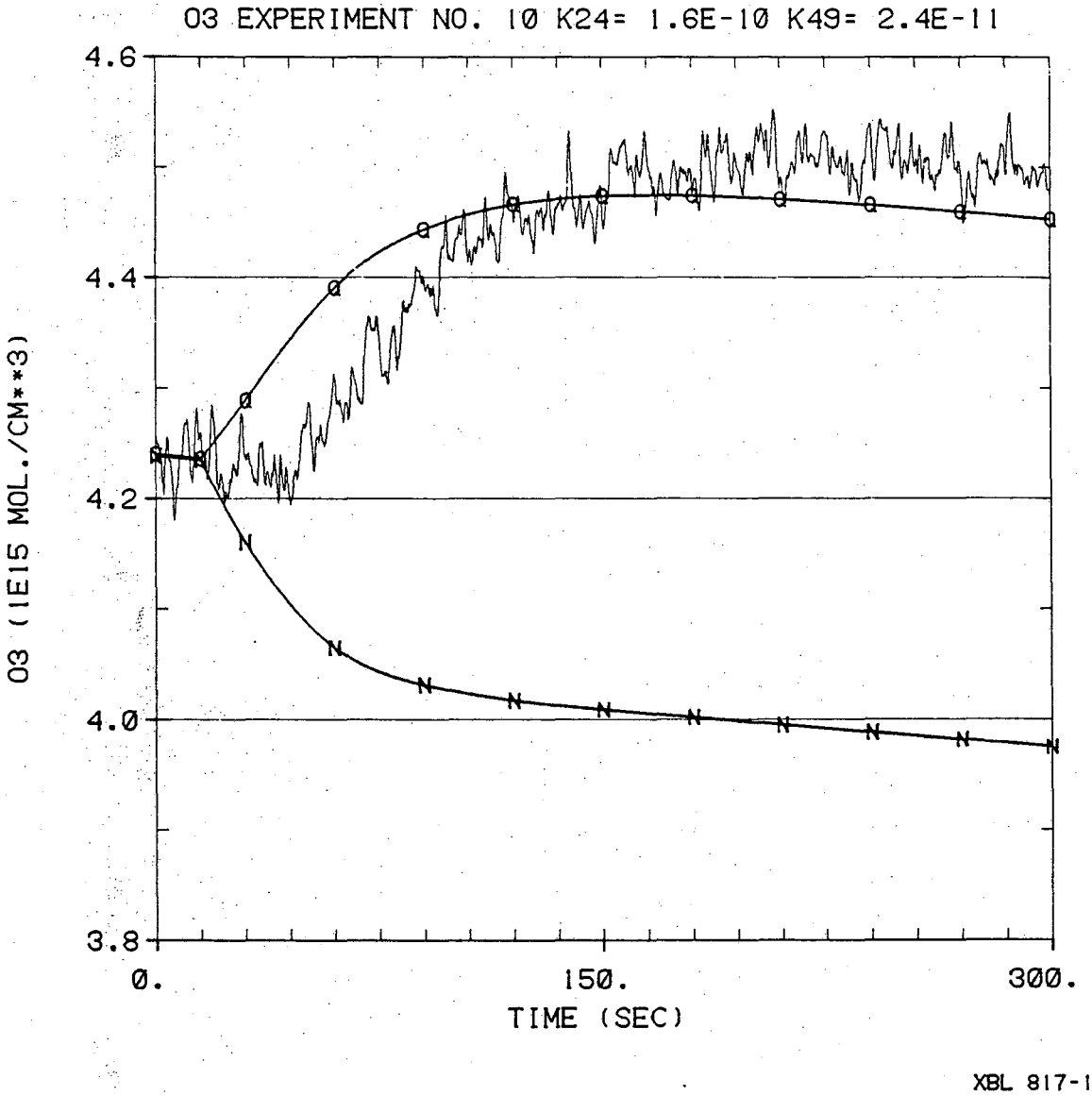

Fig. 38c. Experiment 10 observed and calculated O_3 profiles fast k_{24}.

curves are not real effects, but are due to H_2O addition timing mismatch between the measurements of I and I_o curves. Since this time interval is not included in the comparison between experimental and calculated O_3, they do not affect the determination of optimum k_{24} and k_{49} values. Inspection of figs. 29-38 reveals that the inclusion of the quenching process in the calculations is necessary to bring them into good agreement with experiment, but that no best choice of k_{24} in this range can be made.

If O_2 and HO_2 are assumed to be hard spheres with diameters of 3.4 and 3.5 Å, respectively,[74] the calculated gas kinetic rate constant for this electronic energy transfer reaction is 2.3×10^{-10} cm^3/molecule s, meaning this process has a collisional efficiency between 0.1 and 0.2. Comparison of the range of values obtained in this study with a list of $O_2(^1\Delta)$ quenching rate constants for other typical molecules[75] indicates this energy transfer process is on the order of 10^7 times faster than quenching by other molecular species, presumably due to the near resonance between $O_2(^1\Delta_g \longrightarrow {}^3\Sigma_g^-)$ and HO_2 ($^2A'(001) \longrightarrow {}^2A''(000)$).[27] Even the relatively fast reaction of O_3 with $O_2(^1\Delta)$ is 10^3 times slower than this process.

The implications of this result must be examined in several contexts. Since HO_2 quenching is so much more efficient than any other process in an O_x-HO_x photochemical system, its effects should always be considered when analyzing the kinetics of such a system, particularly when O_3 is being photolyzed below 3000 Å to

produce $O_2(^1\Delta)$. The calculated O_3 profiles in Figs. 29a-c demonstrate the significant difference inclusion of this process can make under some experimental circumstances.

The magnitude of the effect of this process on stratospheric chemistry can be estimated from the recent measurements of HO_2 mixing ratio at mid-latitudes.[10] At 37 km Anderson measures an HO_2 mixing ratio of 4.7×10^{-10}, and Krueger's 1976 U.S. Standard Atmosphere Mid-Latitude Ozone Model[76] indicates an O_3 mixing ratio at this altitude of 8.0×10^{-6}. Thus, the relative rates of destruction of $O_2(^1\Delta)$ at this altitude are:

Species	$\langle k_Q \rangle$	[Q]	$\langle k_Q \rangle$ [Q]
Air	4.5×10^{-19}	1.0	4.5×10^{-19} (1.00)
O_3	4.4×10^{-15}	8.0×10^{-6}	3.5×10^{-20} (0.08)
HO_2	3.3×10^{-11}	4.7×10^{-10}	1.6×10^{-20} (0.03)

This process therefore contributes several percent to the quenching of $O_2(^1\Delta)$ in this region of the atmosphere.

In addition to the quenching of $O_2(^1\Delta)$, the fate of the excited HO_2 produced should be considered. No rates have yet been measured for this state either for reaction with or deactivation by other molecules. A relatively long fluorescence lifetime of 7.6 milliseconds has been estimated for this state,[30] but never measured. This product state has been exploited in the laboratory to

measure relative HO_2 concentrations at the end of a flow tube,[34] by adding a constant large excess of $O_2(^1\Delta)$ to the flow and observing the strength of the 1.43 micron emission from $HO_2(^2A')$ produced. Knowledge of the $O_2(^1\Delta)$ concentration, energy transfer rate constant, fluorescence quantum yield under the experimental conditions, and absolute collection and detection efficiencies of the detection system would be required to make absolute HO_2 measurements using this method.

In the stratosphere, $O_2(^1\Delta)$ concentrations are known to be quite large, reaching an estimated maximum at 50 km of 4×10^{10} molecules/cm^3.[77] This implies that every HO_2 molecule at 50 km is collisionally excited at a rate of about 1 s^{-1}. In the absence of quenching this would result in about 1 percent of the HO_2 molecules being in the excited state, and about 10^7 photons/cm^3 s being emitted from the excited molecules. Of course quenching would reduce both these quantities, but even so, observable HO_2 emission from this region of the atmoshere may result, and interesting excited state HO_2 chemistry is possible. If HO_2 emission could be observed, the possibility even exists of measuring HO_2 in situ, in a manner similar to the laboratory technique described earlier.

B. OH Integrated Absorption Coefficients

The spectroscopy of the OH radical has been studied extensively,[11,18-20] and only a brief description will be given here. OH has an unpaired electron whose orbital angular momentum (L=1) is coupled to the internuclear axis, and in the ground electronic state the projection of L on this axis is designated $\Lambda=1$. The electron spin (S=1/2) also couples to the internuclear axis to give $\Sigma=1/2$, and the projection of the resultant total angular momentum on the axis is $\Omega = \Lambda + \Sigma$. This gives rise to two sub-states, $^2\pi_{3/2}$ ($\Omega=3/2$, F_1) and $^2\pi_{1/2}$($\Omega=1/2$, F_2), with $^2\pi_{3/2}$ lying lower in energy. Since the total electronic angular momentum Ω can be either parallel or antiparallel to the internuclear axis each energy level is split into two different levels, called lambda doublets. The inclusion of angular momentum due to mechanical rotation results in total angular momentum J, which can have values of Ω, $\Omega + 1$,... The energy level diagram for the first two vibrational levels of OH is shown in Fig. 39. The lambda doubling splitting has been exaggerated for display purposes, and the parity shown using the notations of both references 18 (e,f) and 17(+,=). The four transitions investigated,

P(4.5) 1-	3407.6069 cm^{-1}
P(4.5) 1+	3407.9890 cm^{-1}
P(3.5) 2-	3421.9360 cm^{-1}
P(3.5) 2+	3422.0123 cm^{-1}

are shown in Fig. 39 to avoid notational confusion.

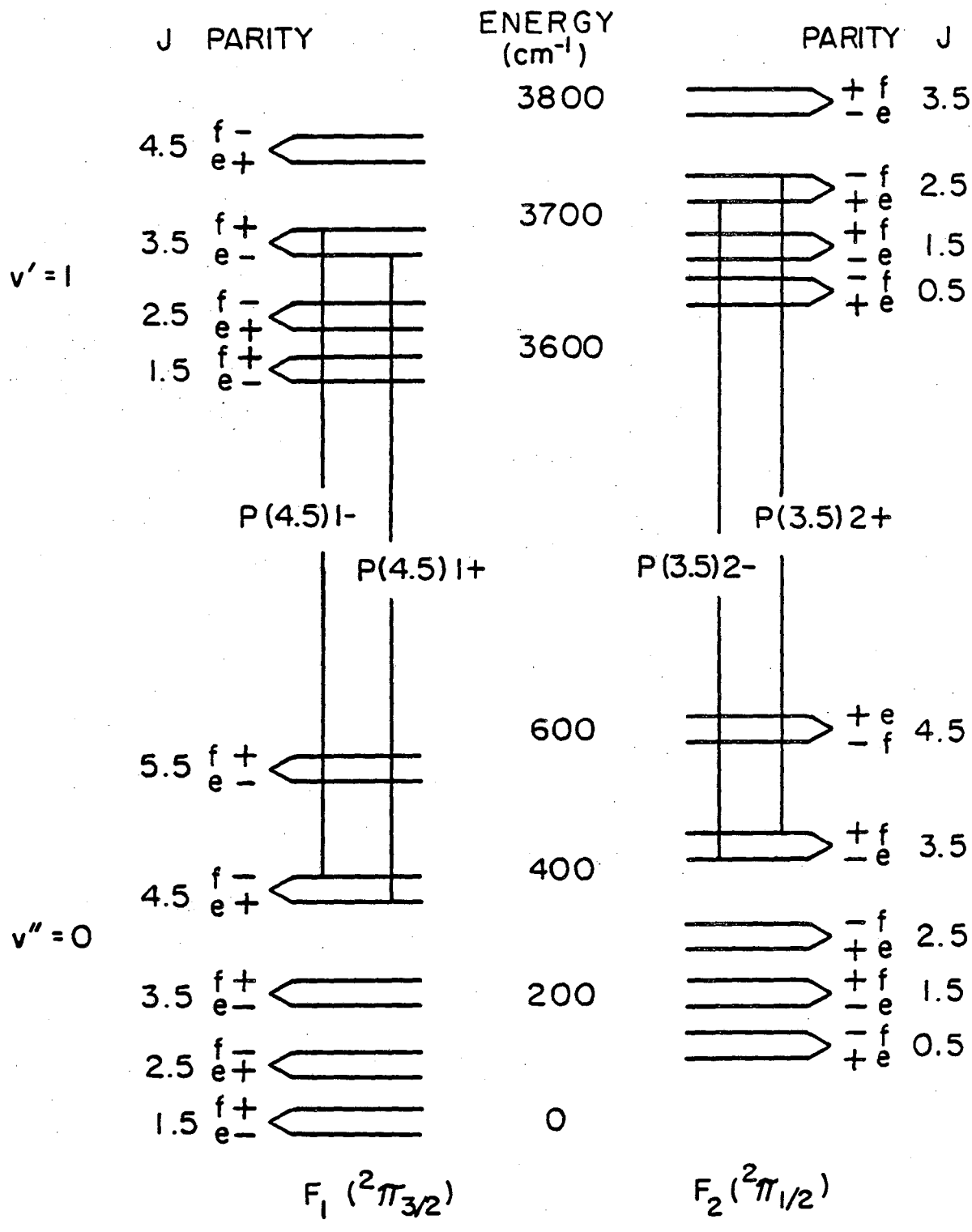

Fig. 39. Energy level diagram for the OH molecule.
In the notation for the transitions:
the letter P indicates $\Delta J = -1$,
the number in parenthesis indicates J of the lower state,
the last number indicates the spin-orbit state (F_1 or F_2),
the sign indicates the parity of the lower state.

The data obtained during run sequences 1-3, described in Section III-E, are listed in Table 8. The absorption lines are referred to in Table 8 by the last two characters of the notation listed above (eg., 1- refers to the P(4.5) 1- transition).

The linewidth data, shown in Table 8, was calculated from the widths determined by fitting a gaussian to each measured absorption profile, together with the tuning rate measured with the etalon (~22 cm^{-1}/A) and the total current scanned in each run. The relatively large dispersion in the linewidth data for each line does not reflect actual change in the true absorption profile, since all measurements were performed at the same temperatures and with the same H_2O and He pressures, but rather is due to laser frequency jitter. Since all four transitions investigated are expected to have nearly equal linewidths, an average value for the linewidth of 0.0138 ± 0.0016 cm^{-1} FWHM was calculated, weighting each value by the signal/noise for that determination as indicated by the gaussian fitting routine. The values indicated by an asterisk next to them were not included because of irregular tuning rate measurements in their frequency region with the laser mode used or because of insufficient number of data points. A separate determination of the average linewidths for the 1± and 2± line groups indicated that they are equal to better than 1 percent.

Relative line intensities were calculated from the results of runs 1 and 3. The two measurements during run 1 of the 1- transition were weighted by their fitted uncertainties and averaged. The two measurements during run 3 of both the 2+ and 2- transitions were averaged and

Table 8
OH Modulation Results

Run	Line	Mod. Freq. (Hz)	Mod. Signal Phase (deg)	Mod. Signal ΔI (mv)	Mod. Signal I (mv)	Mod. Signal ΔI/I ($x10^3$)	Linewidth FWHM (cm^{-1})
1(fast)	1-	15.625	-10.81	21.10	6750	3.13	.0099*
1(fast)	1+	15.625	-28.13	15.17	5800	2.62	.0087*
1(slow)	1-	15.625	-16.94	20.72	7000	2.96	.0133
2(1800 Hz)	1-	7.8125	- 4.15	12.08	4500	2.68	.0111
2(1800 Hz)	1-	15.625	-31.89	11.09	4500	2.44	.0127
2(1800 Hz)	1-	31.25	-29.34	8.34	4550	1.81	.0080*
2(1800 Hz)	1-	62.5	-80.19	9.43	4600	2.10	.0057*
2(D.C.)	1-	7.8125	- 5.03	6.96	---	---	.0147
2(D.C.)	1-	15.625	-13.97	6.32	---	---	.0146
2(D.C.)	1-	31.25	-25.84	5.31	---	---	.0158
2(D.C.)	1-	62.5	-56.22	4.03	---	---	.0135
3(Scan 1)	2-	15.625	-16.63	3.74	3100	1.21	.0112
3(Scan 1)	2+	15.625	-23.79	4.11	3950	1.04	.0123
3(Scan 2)	2-	15.625	-23.06	7.33	8400	.87	.0170
3(Scan 2)	2+	15.625	-21.59	11.82	9000	1.31	.0141
3	1+	15.625	-23.65	10.81	5500	1.82	.0160*

the uncertainty of each average value estimated. The results are summarized in Table 9. Listed uncertainties are one standard deviation.

The absolute intensity of the P(4.5) 1- transition was determined from analysis of run 2. In order to calculate OH cross sections from the observed peak absorption modulation amplitudes, the modulation amplitudes of the OH concentration first had to be determined using the numerical simulation program. Most of the input parameters for the simulation had been determined during the O_3-H_2O steady state photolysis experiments. The two parameters which had to be determined for each run were the O_3 flow in rate and the photolysis intensity, which were inferred from the steady state O_3 measurements made with the photolysis lamps off and on, and the H_2O flow off and on. The three different sets of rate constant values for the $OH+HO_2$ and $HO_2+O_2(^1\Delta)$ reactions, described in Section IV-A, were used in separate simulations of each set of conditions to estimate the uncertainty of the calculated OH concentration amplitudes. The O_3 measurements and calculated OH amplitudes and phases are listed in Table 10. Listed uncertainties are one standard deviation. The peak absorption cross section was calculated for the 1- line from the 7.8 and 15.6 Hz results from run 2 and the 15.6 Hz results of run 1 from the formula:

$$(\Delta I/I)_{peak} = \sigma_{peak} nl \qquad (60)$$

Table 9
Relative Intensity Determination

	Line	Observed Modulation Amplitude
Run 1	<1->	$(\Delta I/I) = 2.98 \pm 0.13 \times 10^{-3}$
Run 1	<1+>	$(\Delta I/I) = 2.62 \pm 0.37 \times 10^{-3}$
Run 3	<2->	$(\Delta I/I) = 1.04 \pm 0.24 \times 10^{-3}$
Run 3	<2+>	$(\Delta I/I) = 1.18 \pm 0.19 \times 10^{-3}$
Run 3	<1+>	$(\Delta I/I) = 1.82 \pm 0.21 \times 10^{-3}$

Calculated Line Intensity Ratios

$S_{1+}/S_{1-} = 0.878 \pm 0.131$

$S_{2-}/S_{1+} = 0.573 \pm 0.146$

$S_{2+}/S_{1+} = 0.646 \pm 0.128$

$S_{2+}/S_{2-} = 1.128 \pm 0.316$

$S_{2-}/S_{1-} = 0.503 \pm 0.146$

$S_{2+}/S_{1-} = 0.567 \pm 0.154$

Table 10
Measured O_3 and Calculated OH Modulation Behavior

RUN	O_3(dark) (10^{15} molecules/cm^3)	O_3(H_2O+hν) (10^{15} molecules/cm^3)	Mod. Freq. (Hz)	Calculated Phase (deg)	[OH] Modulation Amplitude (10^{11} molecules/cm^3)
pre-1	17.18	2.053	15.625	-19.22 ± 0.53	4.56 ± 0.34
pre-2	17.14	2.056	---	---	---
<2>[a]			7.8125	-9.53 ± 0.75	3.95 ± 0.89
<2>[a]			15.625	-18.32 ± 1.17	3.82 ± 0.85
<2>[a]			31.25	-34.43 ± 1.90	3.35 ± 0.69
<2>[a]			62.5	-54.47 ± 1.85	2.36 ± 0.44
post-2	14.15	2.400	---	---	---
pre-3	18.62	2.334	---	---	---

[a] Listed phase and amplitude are average of results calculated using pre-2 and post-2 conditions.

where $\Delta I/I$ is the peak absorption modulation obtained from the gaussian fits, n is the calculated OH modulation amplitude and l is the absorption pathlength. The results of run 2 at 31 and 63 Hz were not considered due to the poor quality of the data. The calculated peak cross section values are:

Run 2	7.8125 Hz	$\sigma = 2.29 \pm 0.63 \times 10^{-18}$ cm^2/molecule
Run 2	15.625 Hz	$\sigma = 2.16 \pm 0.64 \times 10^{-18}$ cm^2/molecule
Run 2	Average	$\sigma = 2.23 \pm 0.45 \times 10^{-18}$ cm^2/molecule
Run 1	15.625 Hz	$\sigma = 2.21 \times 10^{-18}$ cm^2/molecule

The listed uncertainties include both the uncertainty in $\Delta I/I$ and OH modulation amplitude, n, and correspond to one standard deviation. The uncertainty for the run 1 results is not listed because chemical conditions were not determined both before and after run 1, as they were for run 2; so, the uncertainty in the calculated OH amplitude does not reflect possible changes in O_3 concentration and photolysis intensity during the course of the run. Nevertheless, the good agreement between the run 1 and run 2 results lends support to the run 2 average value.

To confirm the simulation program's ability to accurately model experimental conditions, the observed phase shifts and amplitude profiles for run 2 were compared with those predicted by the numerical simulation program. Figure 40 shows the calculated phase shifts versus frequency as a solid line with dotted lines indicating the

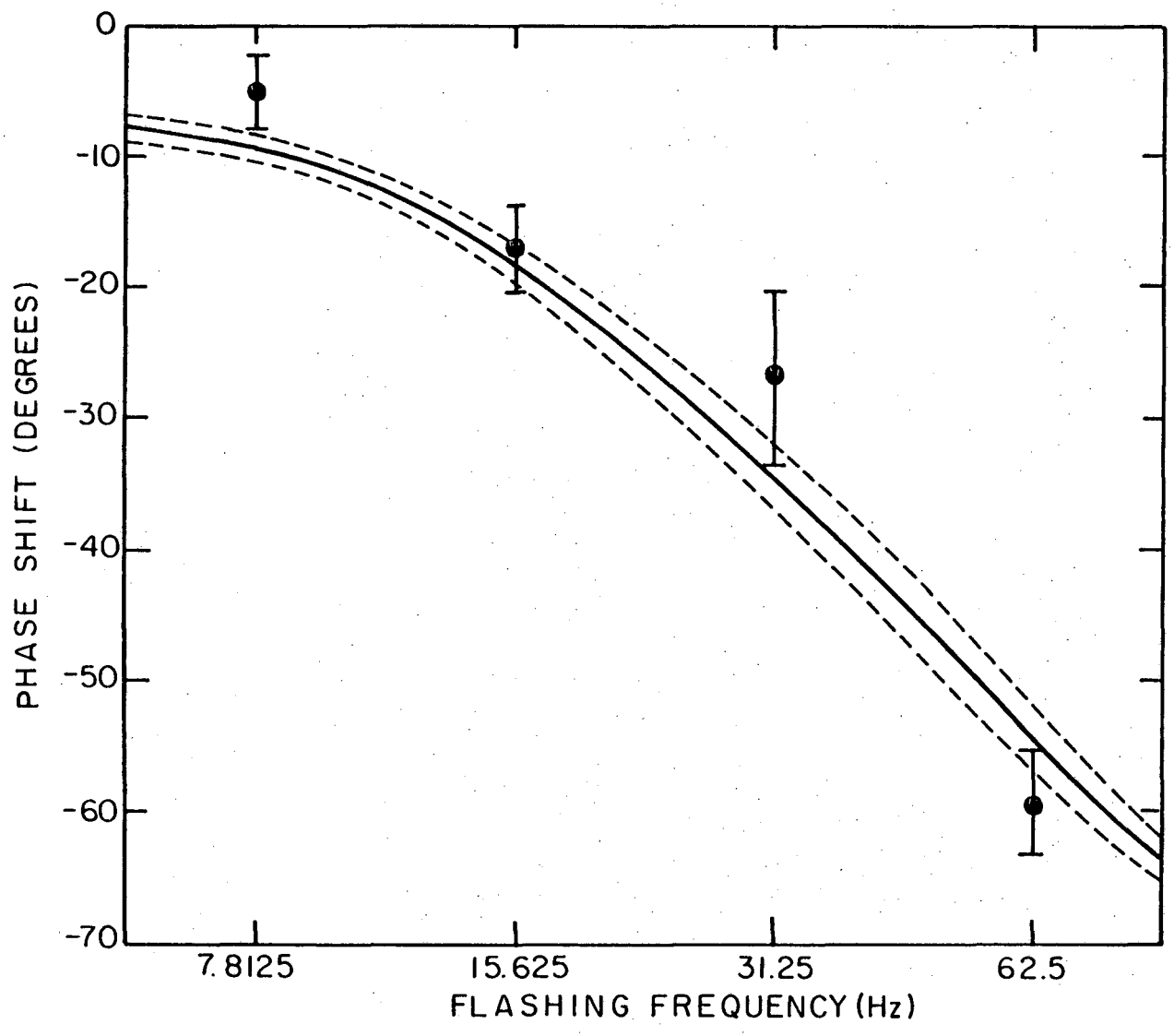

XBL 818-6373

Fig. 40. Calculated and experimental OH phase shift versus flashing frequency. (From Run 2 D.C. and 1800 Hz results. See Tables 8 and 10.)

uncertainty range in the calculated value due to uncertainty in experimental conditions and rate constants. The dots are the experimental determinations, made from both the 1800 Hz (demodulated) and D.C. (direct) carrier results. For comparison of amplitude profiles, only the D.C. carrier results are considered, because even though they are unnormalized for absolute carrier amplitude, their signal/noise is better than the 1800 Hz demodulated results. To compare the calculated and experimental amplitude profiles, which are in different units, each set of four amplitude values was normalized by the geometric mean of the set, and the log (base e) of the normalized amplitudes compared. The results are shown in Fig. 41, which again shows the uncertainty of both the calculated and experimental results. The good agreement between phase shifts and relative amplitudes versus frequency as predicted by numerical simulation and determined experimentally confirms the validity of using calculated OH concentrations in this investigation.

The integrated absorption coefficient is readily obtained from the quantities already determined, since the absorption profile was assumed to be gaussian.

$$\sigma(\nu) = \frac{S}{(2\pi)^{1/2} W} e^{-\frac{(\nu-\nu_0)^2}{2W^2}} \qquad (61)$$

$$W = FWHM/(8 \ln 2)^{1/2}$$

$$S = (2\pi)^{1/2} W \sigma_{peak}$$

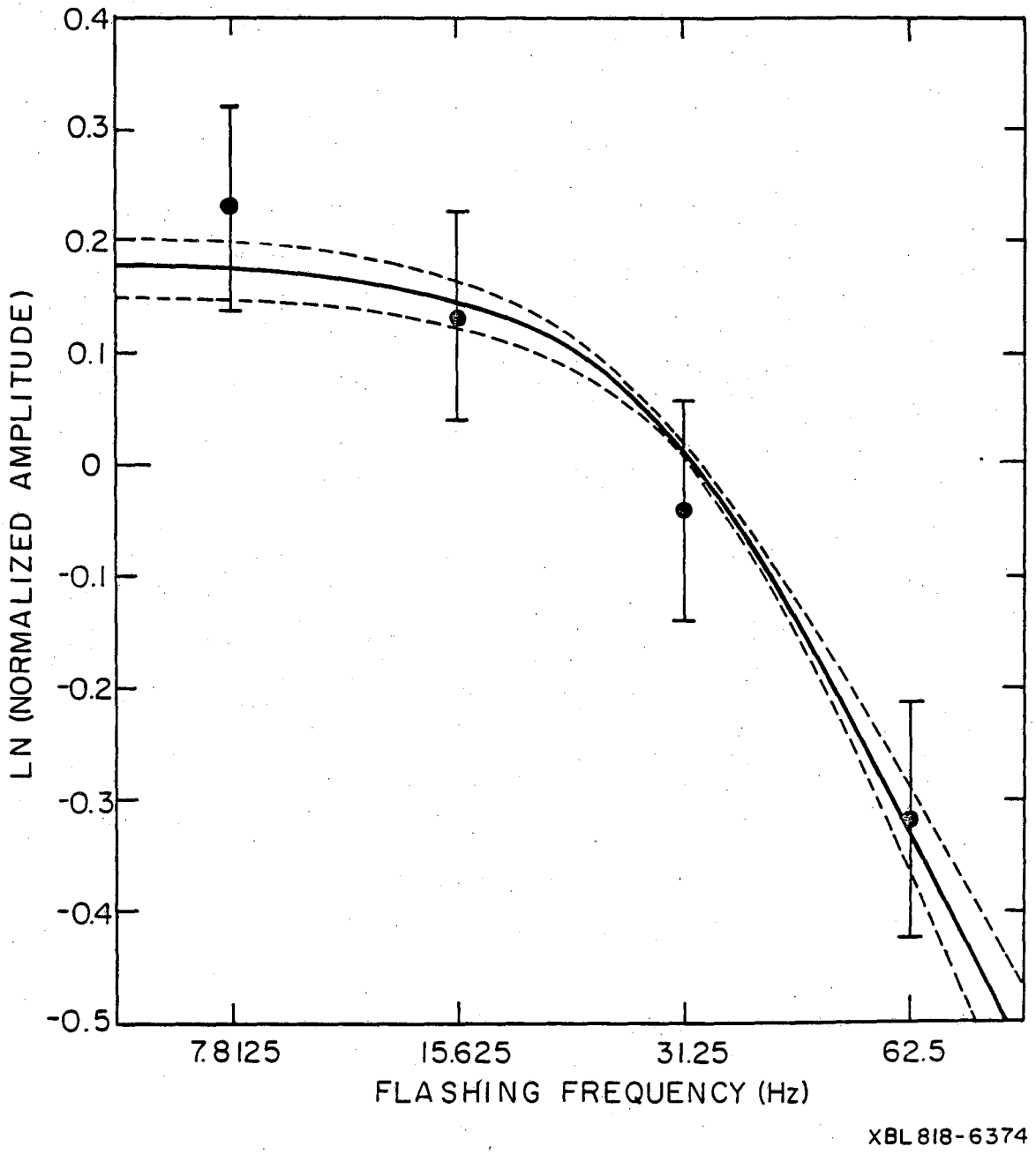

Fig. 41. Calculated and experimental relative OH amplitude versus flashing frequency. (From Run 2 D.C. results; see Tables 8 and 10.)

Using the average peak cross section from run 2 for the P(4.5) 1- line, the FWHM determined earlier and the line intensity ratios obtained from runs 1 and 3, the following integrated absorption coefficients were calculated:

line	frequency cm^{-1}	S (cm/molecule)
P(4.5) 1-	3407.6069	$3.26 \pm 0.76 \times 10^{-20}$
P(4.5) 1+	3407.9890	$2.87 \pm 0.79 \times 10^{-20}$
P(3.5) 2-	3421.9360	$1.64 \pm 0.61 \times 10^{-20}$
P(3.5) 2+	3422.0123	$1.85 \pm 0.66 \times 10^{-20}$

Listed uncertainties are one standard deviation.

The only other results available to date on the intensities of these OH transitions are the values calculated by Gillis and Goldman.[19,78] They obtain $S(1\pm) = 1.06 \times 10^{-19}$ cm/molecule and $S(2\pm) = 5.95 \times 10^{-20}$ cm/molecule, which are about a factor of 3 higher than the values determined in this study. Since calculated intensities usually have about a factor of 2 uncertainty ascribed to them[79,80] and the experimental values are probably good to a factor of 1.5 (two standard deviations), the intensities of the two studies are in rough agreement. The theoretical results predict the two lambda components of each vibration-rotation transition to be very nearly equal (±0.3 percent) differing only slightly due to a small difference in the energy of their lower states (~0.8 cm^{-1}). The experimental results, listed in Table 9, indicate differences of about

13 percent for both the 1 ± and 2± doublets, although they could be equal within experimental uncertainty. The ratio $S_{2\pm}/S_{1\pm}$ is calculated to be 0.561 and the average obtained in the experiments $\langle S_{2\pm}/S_{1\pm} \rangle$ is 0.572. Therefore, the agreement between theory and experiment for relative intensities is very good.

The results of this investigation have application in several areas. Although the sensitivity of the instrument used in this study was not particularly good, diode laser systems are presently capable of measuring absorptions as small as 10^{-9} cm^{-1},[43] which corresponds to an OH concentration at low pressure of ~10^9 molecules/cm^3. This is not as sensitive as resonance fluorescence detection using the A ⟶ X band of OH, but circumvents the disruption which the UV fluorescence excitation source can cause.[25] Since OH is a key reactive intermediate in many gas phase chemical systems, the potential for exploitation of its infrared absorptions in laboratory investigations is great.

Infrared techniques for measurement of trace species in the atmosphere have developed rapidly in the last decade because of their high selectivity. Recently the ClO free radical has been measured in the atmosphere using a laser heterodyne radiometer.[81] ClO has typical line intensities of 1 x 10^{-20} cm/molecule,[40] comparable to OH, and has been measured at the 100 ppt level (~10^7 molecules/cm^3). Since OH is also present in the mid-stratosphere (30 km) in this concentration range,[82] the possibility exists of measuring atmospheric OH with sensitive infrared detection systems.

Such a system would provide a better estimate of average OH concentration than the local sampling techniques now employed, as very long optical paths are employed ($[M]l \sim 1\text{-}50 \times 10^5$ atm-cm).[81]

V. CONCLUSIONS

This investigation resulted in the first experimental determination of integrated absorption coefficients for several vibration rotation transitions of the OH radical and the first measurement of the rate constant for the HO_2-$O_2(^1\Delta)$ energy transfer reaction. A combination of molecular modulation kinetics[46] and diode laser spectroscopy was employed to measure the following OH integrated absorption coefficients:

P(4.5) 1-	(3407.6067 cm^{-1})	$S = (3.26 \pm 1.52 \times 10^{-20}$ cm/molecule)
P(4.5) 1+	(3407.9890 cm^{-1})	$S = (2.87 \pm 1.58 \times 10^{-20}$ cm/molecule)
P(3.5) 2-	(3421.9360 cm^{-1})	$S = (1.64 \pm 1.22 \times 10^{-20}$ cm/molecule)
P(3.5) 2+	(3422.0123 cm^{-1})	$S = (1.85 \pm 1.32 \times 10^{-20}$ cm/molecule)

Photolysis of an O_3-H_2O system was investigated in a flow reactor and simulated using numerical techniques to determine the energy transfer rate constant for $HO_2 - O_2(^1\Delta)$:

$$k_{49} = 3.3 \pm 1.6 \times 10^{-11} \text{ cm}^3/\text{molecule s}$$

The sensitivity of this result to the $OH+HO_2$ reaction rate constant was considered in detail.

The integrated absorption coefficients reported here are about a factor of 3 smaller than those calculated by Gillis and Goldman,[19] but this can be reconciled by the estimated uncertainties of the two

studies. Further investigation of the intensities of these OH transitions would be useful, using both a less complex chemical system to generate OH and an improved detection system and source, either a carefully selected diode laser or an F-center laser. A comparison of the line intensities and concentrations of OH and ClO in the atmosphere indicates that current infrared detection techniques[81] may be sensitive enough to measured OH radical concentrations in the stratosphere.

The rate constant for the near resonant energy transfer process:

$$HO_2\ (^2A'') + O_2\ (^1\Delta_g) \longrightarrow HO_2\ (^2A') + O_2$$

is about 10^7 times faster than the $O_2(^1\Delta)$ quenching rate constants of other molecular species. Because of this, trace amounts of HO_2 can effectively compete with major species for $O_2(^1\Delta)$ in many systems, and the possible results should always be considered. Rough upper limit estimates show that a significant fraction (~1 percent) of the HO_2 in the upper atmosphere may exist in the excited $^2A'$ state and fluorescence from this state could be relatively strong (~10^7 photons/cm^3 s). In order to investigate the effect of excited state HO_2 chemistry on the stratosphere and possibly exploit the predicted HO_2 fluorescence caused by ambient $O_2(^1\Delta)$, measurements of HO_2 ($^2A'$) reaction and quenching rate constants for a variety of molecular species are needed.

ACKNOWLEDGEMENTS

I wish to express my appreciation to Professor Harold S. Johnston for his guidance and support throughout the course of this research. His patient and understanding approach to graduate research allowed me to pursue a variety of research interests of my own choosing and develop resourcefulness and initiative. His knowledge and enthusiasm regarding atmospheric chemistry proved to be a valuable asset and focal point for me.

I have enjoyed the assistance and encouragement that I received from my fellow graduate students, friends and colleagues, and wish to thank them all. Richard Graham introduced me to the areas of optics, electronics and minicomputers. Herb Nelson, Dave Littlejohn and Bill Marinell: were constantly available with advice on experimental technique and moral support. Frank Magnotta provided me a perspective on chemical research alternate to the academic one prevalent at Berkeley.

Sincere appreciation goes to my wife, Claudia, for her emotional support and encouragement during this challenging and rewarding experience.

I wish to thank the personnel of the Department of Chemistry and of the Lawrence Berkeley Laboratory for their generous support, and especially Tom and Don of the electronics shop for their advice and helpful discussions.

This work was supported by the Director, Officer of Energy Research, Office of Basic Energy Sciences, Chemical Sciences, Division of the U.S. Department of Energy under Contract No. W-7405-ENG-48.

APPENDIX A: Reaction Mechanism for Simulation of the O_3-H_2O System

The reaction set listed below was used throughout this investigation to model the O_3-H_2O photochemical system. The simulations were performed with the CHEMK chemical kinetics program described in Section III-A-3. The rate constants are in units of $(cm^3/molecule)^{x-1}$ sec^{-1}, where the order of the reaction is given by:

X = 0 for species independent flow in

X = 1 for unimolecular processes

X = 2 for bimolecular processes

X = 3 for termolecular processes

In the HO_2-$O_2(^1\Delta)$ study O_2 and O_3 flow in were represented by reactions 46' to 51', while in the OH modulation study just 46 and 47 were used.

		$\sigma(cm^2/molecule)$	σ
1.	$O_3 + h\nu \longrightarrow O_2(^1\Delta) + O(^1D)$	1.0E-17	1.0
2.	$O_3 + h\nu \longrightarrow O_2 + O$	1.0E-18	1.0
28.	$H_2O_2 + h\nu \longrightarrow OH + OH$	7.4E-20	1.0
		k	
3.	$O(^1D) + O_3 \longrightarrow O_2 + O_2$	1.2E-10	
4.	$O(^1D) + O_3 \longrightarrow O_2 + O + O$	2.3E-10	
5.	$O(^1D) + H_2O \longrightarrow OH + OH$	2.3E-10	
6.	$O(^1D) + O_2 \longrightarrow O + O_2$	3.6E-11	
7.	$O(^1D) + He \longrightarrow O + He$	1.0E-15	

8. $O(^1D) + H_2O_2$	$\longrightarrow OH + HO_2$	5.2E-10
9. $O_2(^1\Delta) + O_3$	$\longrightarrow O_2 + O_2 + O$	4.4E-15
49. $O_2(^1\Delta) + HO_2$	$\longrightarrow O_2 + HO_2$	Note 1
10. $O_2(^1\Delta) + H_2O$	$\longrightarrow O_2 + H_2O$	4.0E-18
11. $O_2(^1\Delta) + O_2$	$\longrightarrow O_2 + O_2$	1.7E-18
12. $O_2(^1\Delta) + He$	$\longrightarrow O_2 + He$	8.0E-21
13. $O + O_3$	$\longrightarrow O_2 + O_2$	8.8E-15
14. $O + O_2 + H_2O$	$\longrightarrow O_3 + He$	5.6E-33
15. $O + O_2 + He$	$\longrightarrow O_3 + He$	3.4E-34
16. $O + O_2 + O_2$	$\longrightarrow O_3 + O_2$	6.4E-34
17. $O + O_2 + O_3$	$\longrightarrow O_3 + O_3$	1.7E-33
18. $O + OH$	$\longrightarrow H + O_2$	4.0E-11
19. $O + HO_2$	$\longrightarrow OH + O_2$	3.5E-11
20. $O + H_2O_2$	$\longrightarrow OH + HO_2$	2.2E-15
21. $OH + O_3$	$\longrightarrow HO_2 + O_2$	6.8E-14
22. $OH + OH$	$\longrightarrow H_2O + O$	1.9E-12
23. $OH + OH + M$	$\longrightarrow H_2O_2 + M$	2.6E-31
24. $OH + HO_2$	$\longrightarrow H_2O + O_2$	Note 1
25. $OH + H_2O_2$	$\longrightarrow HO_2 + H_2O$	1.7E-12
26. $HO_2 + O_3$	$\longrightarrow OH + O_2 + O_2$	1.6E-15
27. $HO_2 + HO_2$	$\longrightarrow H_2O_2 + O_2$	3.6E-12
29. $H + O_3$	$\longrightarrow OH + O_2$	2.9E-11
30. $H + O_2 + He$	$\longrightarrow HO_2 + He$	1.8E-32
31. $H + O_2 + H_2O$	$\longrightarrow HO_2 + H_2O$	4.5E-31
32. $H + O_2 + O_2$	$\longrightarrow HO_2 + O_2$	5.6E-32

33. He	$\longrightarrow$	1.8E-2
34. O_3	$\longrightarrow$	1.8E-2
35. O_2	$\longrightarrow$	1.8E-2
36. $O_2(^1\Delta)$	$\longrightarrow$	1.8E-2
37. $O(^1D)$	$\longrightarrow$	1.8E-2
39. H	$\longrightarrow$	1.8E-2
40. OH	$\longrightarrow$	1.8E-2
41. HO_2	$\longrightarrow$	1.8E-2
42. H_2O	$\longrightarrow$	1.8E-2
43. H_2O_2	$\longrightarrow$	1.8E-2
44.	$\longrightarrow$ He	4.03E16
45.	$\longrightarrow H_2O$	Note 2
46.	$\longrightarrow O_3$	Note 3
47.	$\longrightarrow O_2$	Note 3
46.'	$\longrightarrow$ A	1.860E11
47.' A	$\longrightarrow$	1.860E-4
48.' B	$\longrightarrow$	5.552E-5
50.' A + B	$\longrightarrow$ A + B + O_3	1.0E-15
51.' A + B	$\longrightarrow$ A + B + O_2	1.0E-16

Note 1: These rate constants were varied to obtain the best fit to experimental results in the HO_2-$O_2(^1\Delta)$ study, and these values used in the OH modulation experiment simulations.

Note 2: This rate constant was either 0, 1.234×10^{15} or 1.234×10^{16} depending on whether conditins were supposed to be either dry or wet, and whether the low or standard H_2O concentration was being simulated.

Note 3: k_{46} was adjusted to give the observed dark O_3 value. The amount of O_2 impurity in the O_3 stream was estimated to be about 10 percent,[69] so k_{47} was always set to 0.1 x k_{46}.

APPENDIX B: LOW FREQUENCY DIGITAL SINE WAVE GENERATOR[83]

Although the generation of sinusoidal waveforms by analog oscillators is widely used, this method has several drawbacks in the low frequency region. First, these oscillators require large valued capacitors or inductors, which are generally costly, and whose values are affected by temperature, age, etc. Second they may require some time after adjustment of their frequency to settle down to their final frequency and amplitude. Third, their frequency may be difficult to measure accurately, or at least be time consuming, as several seconds to several hours may be required to accumulate enough cycles in a counter to characterize the frequency. Lastly, the harmonic distortion of the oscillator is difficult to assess, as generally it will be a function of frequency and non-ideal characteristics of the circuit elements.

The digital sine wave generator overcomes these low frequency problems. Since the frequency is set only by the digital clock frequency, temperature and aging of analog components have little effect upon it. By starting with a reasonably high clock frequency and dividing it down by a known factor, sine wave frequencies in the millihertz region may be measured in seconds. Also, the frequency and amplitude change within fractions of a cycle after they are adjusted, rather than many cycles. The amplitude of the sine wave is set by a reference voltage and a resistor string, and so is independent of frequency, as is the harmonic distortion, which is primarily due to resistor string mismatch.

The method of digital sine wave generation by nonrecursive filtering of a binary waveform was first described by A. C. Davies.[84] Basically it involves sending a binary waveform into a series of n shift registers, which are shifted 2n times per cycle, to produce n delayed versions of the input waveform, and then taking a weighted sum of the first n-1 available waveforms in such a way that the closest possible approximation to a sinusoidal waveform, equal in frequency to the binary waveform, is produced. By proper feedback the shift register series can both produce and delay the binary waveform in the required way. Thus, the generator produces a square wave and non-recursively filters out as many of the harmonics as possible, leaving only the fundamental and several high order harmonics. The remaining components are given by the formulas:[84]

$$\frac{1}{(2kn-)}\sin(2kn-1)w_o t \qquad \frac{1}{(2kn+1)}\sin(2kn+1)w_o t$$

The feedback shift register described here consists of four 4018 CMOS Divide by N circuits connected together in such a way that they form a 16 stage shift register, Fig. B-1. By feeding the inverted output of the last stage into the data input terminal (pin 1) of the first stage, a twisted ring counter results which produces a binary waveform at Q_1 with a frequency 1/2n times the clock frequency and 15 verisions of it, each successively delayed by one clock period, Fig. B-2. To avoid undesired sequences from developing in the registers, a RST reset pulse is produced by differentiating the positive going edge of the Q_{16} output so that all stages are forced

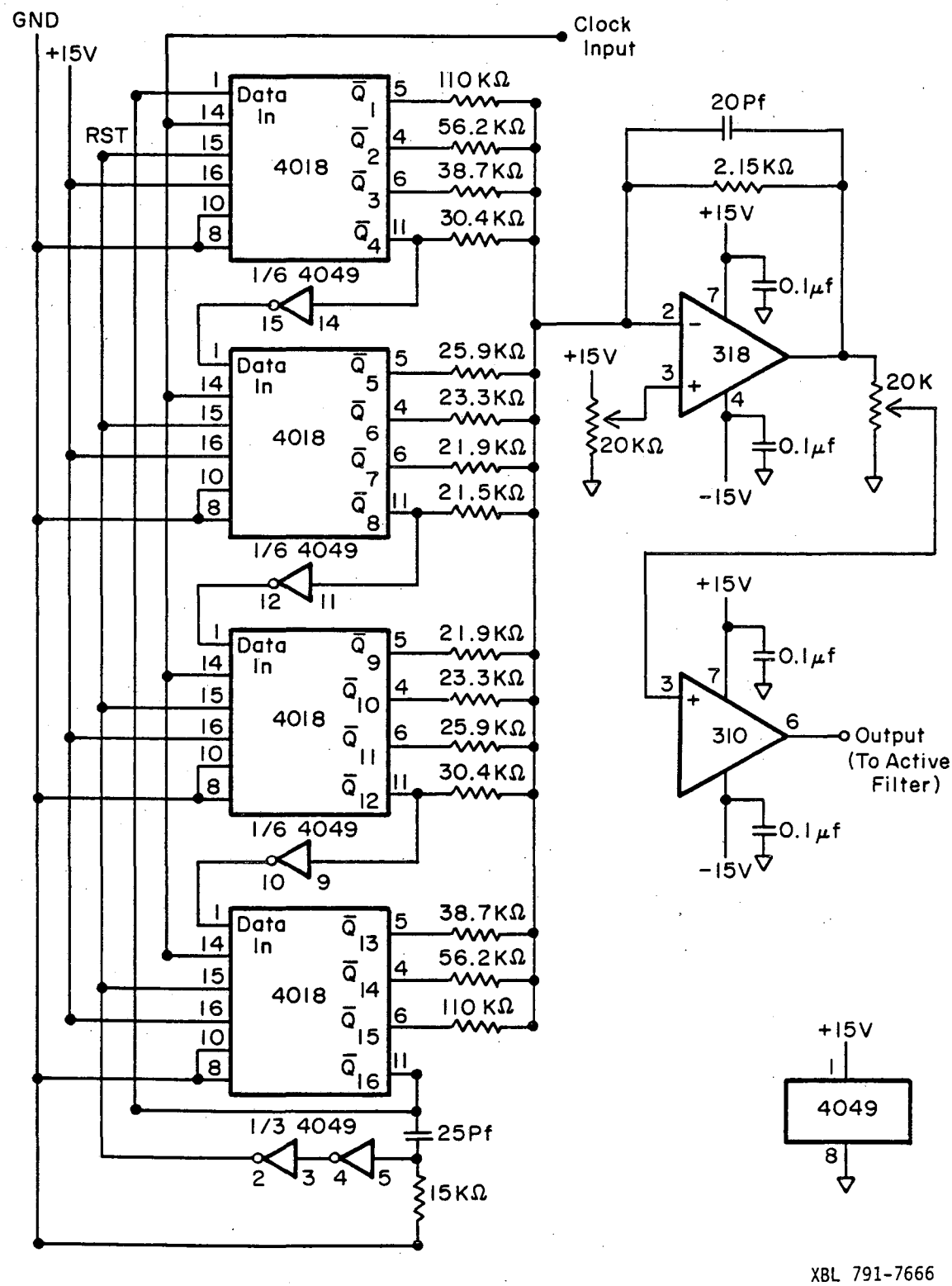

Fig. B-1. Schematic diagram of digital sinewave generator circuit.

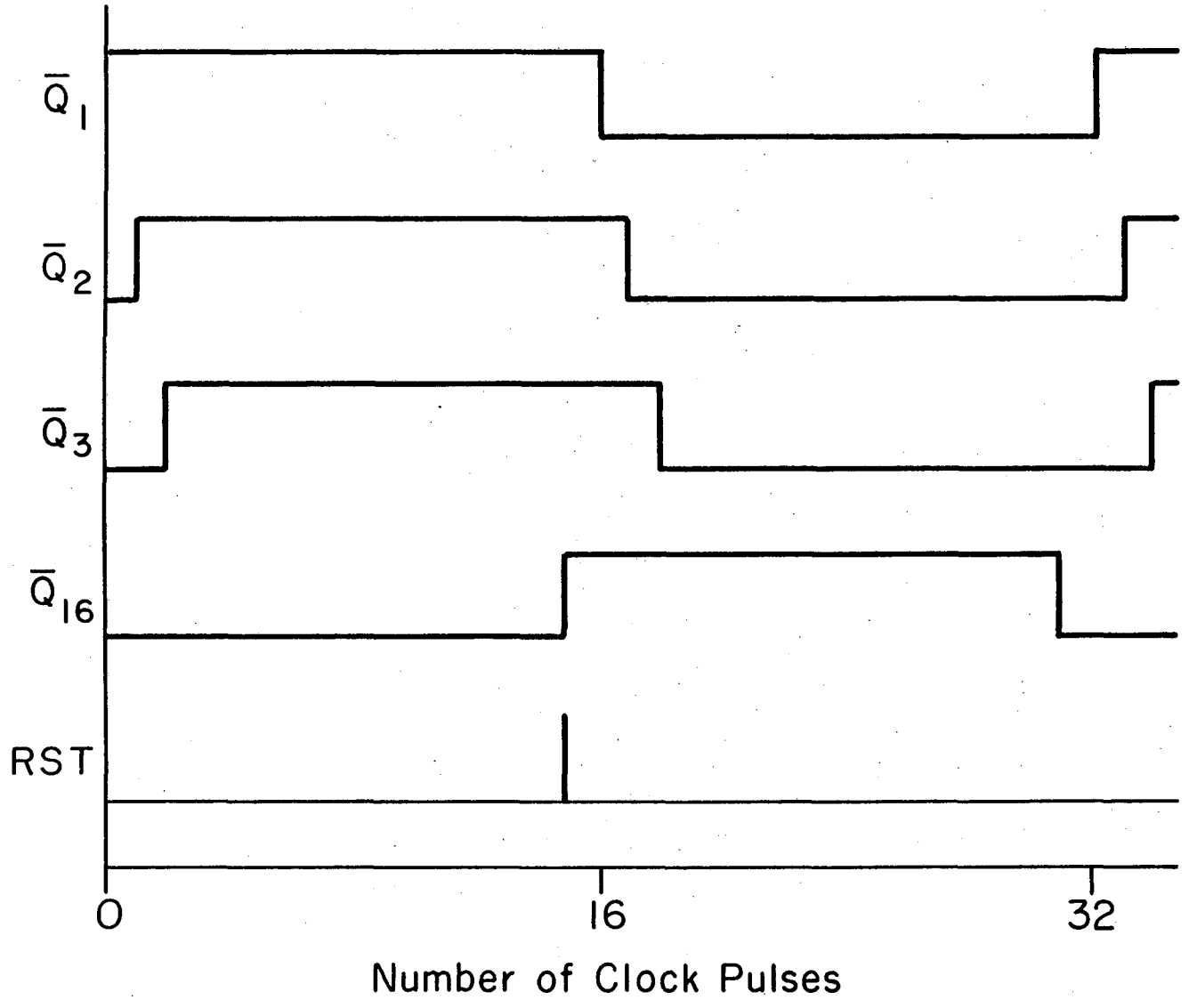

XBL 791-7667

Fig. B-2. Shift register timing diagram.

clear ($\overline{Q}$'s set high) at the time when this condition would normally occur in the proper sequence.

The proper weighting coefficients for each of the n-1 outputs used to give minimum harmonic distortion are given by the formula:[84]

$$W_i = \sin\left(\frac{i\pi}{n}\right) \quad i = 1,n-1$$

where in this case n = 16. From this formula relative conductances for the summing resistors are calculated, followed by relative resistances. In order to lightly load the CMOS shift register outputs so that they will swing to within millivolts of the supply voltage and thus yield a stable output amplitude, the smallest relative resistance was set equal to 21.5 kΩ, which then determines the value of the rest of the resistors. By setting the value of feedback resistor equal to the parallel resistance of the summing resistors, the peak to peak amplitude of the waveform coming out of the summing amplifier equals the shift register supply voltage (about 15 volts). An adjustable positive voltage is applied to the non-inverting input of the summing amplifier so that the output waveform can be centered around zero volts. The waveform is then sent to a variable attenuator, followed by a voltage follower buffer. The waveform is now ready to be used, as is, or to be filtered further to remove the remaining harmonics. A representation of the unfiltered waveform is shown in Fig. B-3.

The generator described above can be driven by any CMOS compatible time base from d.c. to several Megahertz. The one described here, Fig. B-4, was designed for use as an excitation source for a molecular

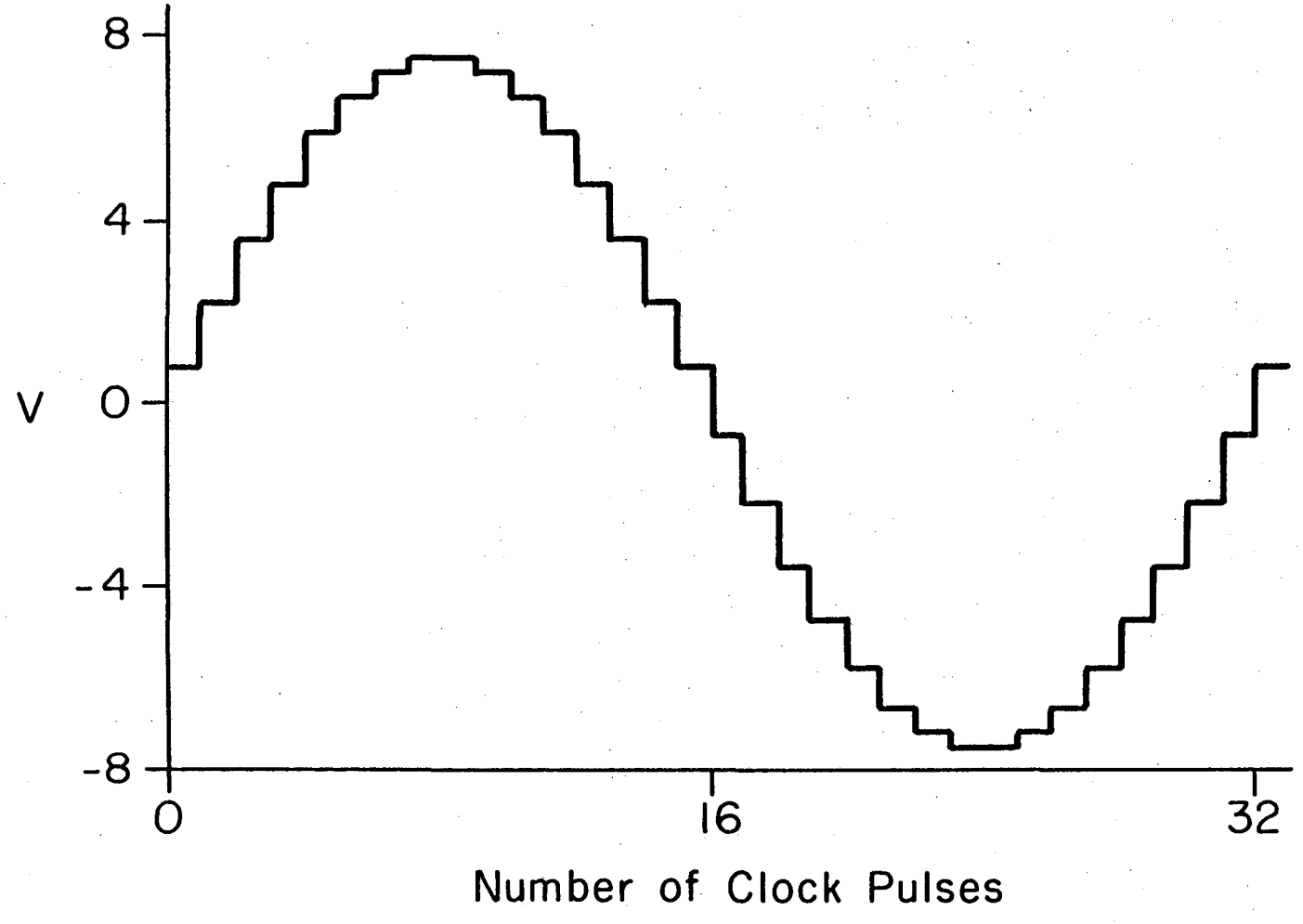

XBL 791-7668

Fig. B-3. Unfilter output waveform of the generator circuit.

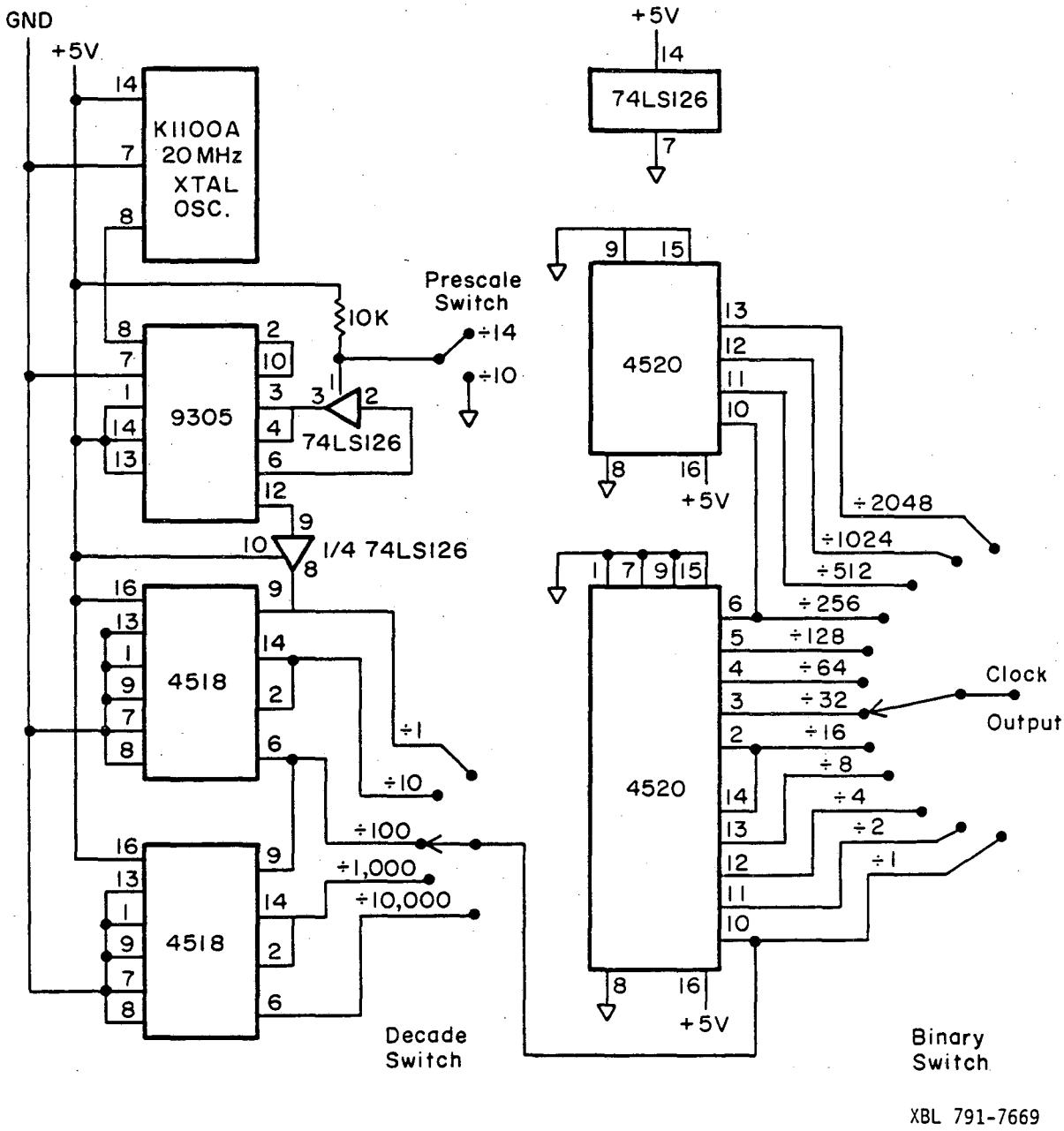

Fig. B-4. Crystal controlled time base circuit schematic.

modulation spectrometer.[46] This method involves measuring the chemical lifetime of a gas phase radical produced in a photochemically driven reaction sequence by measuring the phase shift of the radical concentration with respect to the modulated light source as a function of modulation frequency. For this application, a sine wave generator capable of stable operation below 1 Hz and with half-octave frequency settings was required.

The time base starts with a 20 MHz crystal oscillator (Motorola K1100A). Its output goes through a programmable divider, which divides the oscillator frequency either by 10 or 14 (switch selectable). Since 1.4 is very nearly equal to $2^{1/2}$, switching from the ÷10 to the ÷14 mode allows the output frequency to be shifted downward by half an octave. Next the output of the programmable divider is sent to a series of 4 decade counters, which allow the user to scale the output frequency by factors of 10, from 1 to 10000, by means of the decade switch. From the decade section the selected clock frequency is sent to a series of binary counters, where the user may scale the clock frequency further by factors of 2, from ÷1 to ÷2048, by means of the binary switch. Finally the clock frequency is sent to the generator, which produces a sine wave at 1/32 to the clock frequency. Thus, the span of frequencies of the sine wave generator using this time base is 62.5 kHz to 2.18 milliHertz.

Since the first harmonics produced by the generator are the 31st and 33rd, analog filtering to remove them without allowing the fundamental amplitude to be dependent on filter components is

straightforward. A two pole Butterworth filter[85] was constructed, Fig. B-5, with switch selectable cut off frequency. The selectable R and C values were arranged so that there would be a one to one correspondence between available time base frequencies (excluding half-octave shifts) and filter frequencies. The design criterion decided upon for the filter cut off frequency was that it be 4 times the sine wave frequency it was filtering. This means the fundamental is only attenuated by a factor of 0.998, whereas the 31st harmonic is attenuated by 0.017. Use of this filter makes the generatour output look indistinguishable from a pure sine wave.

Special thanks to Thomas Merrick of the Chemistry Department electronics shop for many helpful discussions related to the design and construction of this instrument.

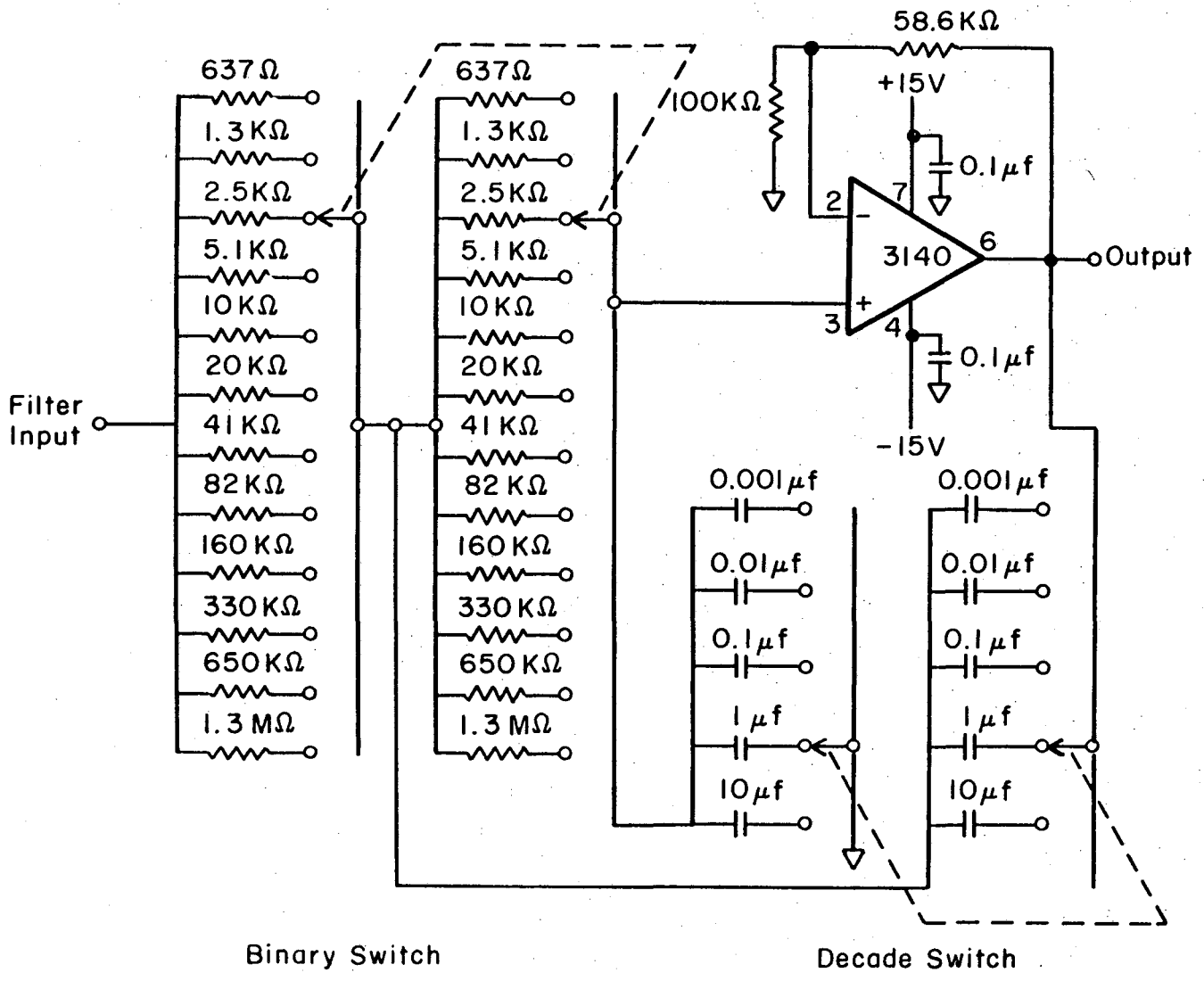

XBL 791-7670

Fig. B-5. Two pole Butterworth active filter circuit schematic.

APPENDIX C: STABLE TUNING FORK CHOPPER DRIVER[86]

Mechanical choppers, especially those of the tuning fork variety, are used extensively in photometric and molecular beam systems today, in conjunction with phase sensitive detection, as a powerful method of signal enhancement. By shifting the center frequency of the information content of the beam from d.c. to the chopper frequency, a good portion of the 1/f noise in analog electronics can be overcome. The advantage of avoiding d.c. baseline drift by this method can be offset however, in cases where accurate measurements are required, by the drift in the amplitude of the mechanical chopper. Thus, for optimum performance, a stable driving circuit for these devices is required.

Starting with a factory supplied driver circuit to determine the necessary characteristics of the driving circuit, first, an improvement was made on the standard circuit and, finally, a different circuit was developed which had the desired properties. The new circuit was tested against the improved standard circuit and found to give a more stable drive amplitude.

Standard drive circuits for tuning fork choppers typically work by taking a signal from a pickup coil on the chopper, usually a slightly distorted sine wave, and amplifying it in a non-linear manner to produce an approximately square wave drive and reference waveform in phase with the pickup signal. In trying to drive the inductive load of the driver coil, switching transients are produced on both the drive waveform, Fig. C-1, and pickup coil waveform. The amplitude of the drive signal is proportional to the power supply voltage, and in the

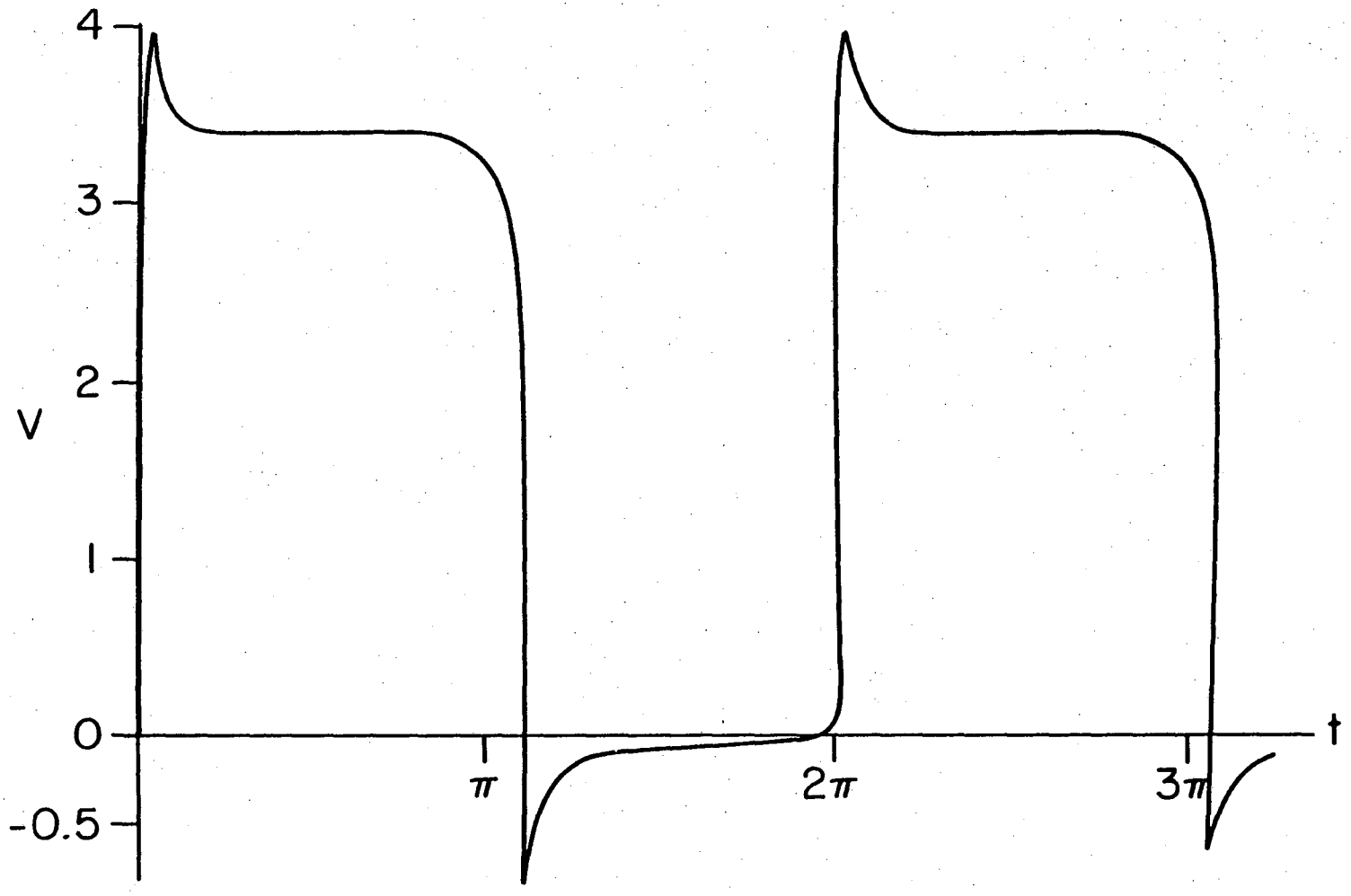

XBL 791-7664

Fig. C-1. Drive coil waveform from conventional driver circuit.

case of the Bulova 5A driver with just a full wave rectified bridge as a d.c. power source, the drive amplitude changes with variations in line voltage. A major improvement in long term stability was obtained by replacing the internal power supply with a regulated 28 vdc power supply. All further work and testing of the factory circuit was done with this configuration.

The new circuit, Figure C-2, works as follows. First the pickup signal goes to a CA3130AT CMOS op amp, which acts as a comparator to produce a square wave. If the output of this particular amplifier is only slightly loaded its output will swing to within millivolts of the positive and negative supplies. Further, if a well regulated power supply is used the amplitude of the square wave will be very stable. The square wave is then attenuated by a potentiometer and fed into a four pole Butterworth filter whose cut-off frequency is set to be the same as the resonant frequency of the tuning fork. For this filter the square wave input will produce purelr sinusoidal output of the same frequency and 180° out of phase (simply inverted). By reversing the polarity on the drive coil connections this well regulated sine wave output is now in phase with the pickup signal and will drive the chopper.

A driver was constructed for both a 400 Hz and an 1800 Hz chopper, the only difference being the values of R and C used in the filter. For a 4 pole Butterworth Filter using the Sallen-Key equal component configuration the value of R and C are set by the cutoff frequency (where the phase shift of the filter is 180°)[85,87]

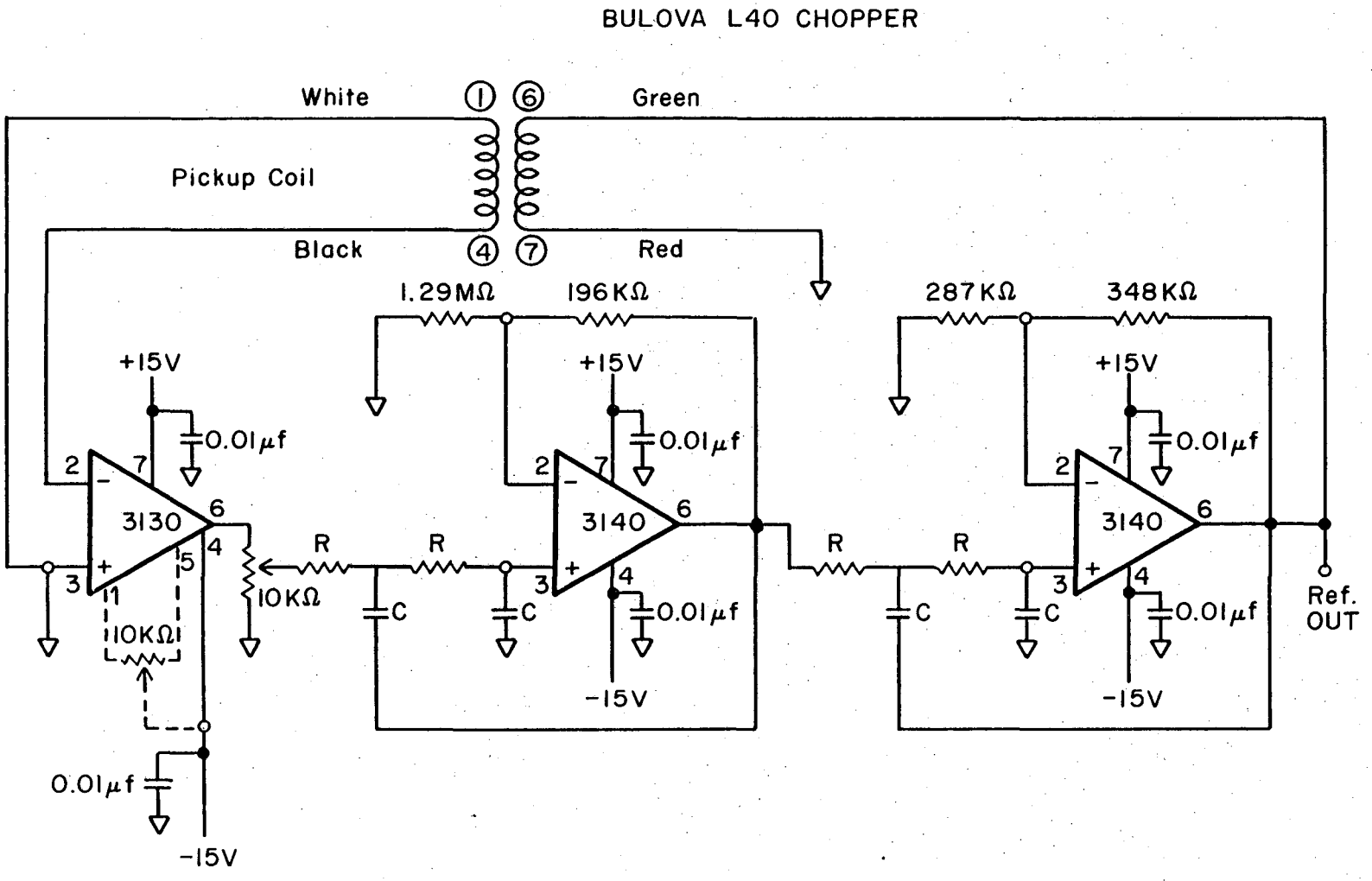

Fig. C-2. Tuning fork chopper driver circuit schematic.

XBL 791-7665

$$RC = \frac{1}{2\pi f_o} \qquad (1)$$

For the 400 Hz chopper C = .0047 μf and R = 8.25 kΩ. Metal Film 1 percent resistors and low leakage capacitors with ±5 - 10 percent tolerances are recommended.

In order to assure positive startup, either a 3130 op amp can be selected which has several volts of positive output when both inputs are grounded in an open loop configuration, or this condition can be produced by adding a 10 kΩ offset adjusting pot across pins 1 and 5 of the 3130.

The maximum drive voltage which a particular tuning fork can handle before harmonic modes are excited must be determined by experiment. By looking at the reference waveform while adjusting the drive amplitude, the onset of severe distortion can be observed. On start up it may be necessary with some tuning forks to decrease the drive amplitude initially to a small value (.5 volts) until stable operation occurs. Then the amplitude can be increased to a level below the maximum level at which the tuning fork can operate.

In order to test the amplitude stability of the chopper movement directly, as opposed to the driver voltage stability, a test arrangement was set up with a tungsten lamp shining through a 400 Hz tuning fork chopper onto a photodiode. By measuring the ratio of the A.C. to D.C. components of the photodiode signal, a good measure of the chopper amplitude was obtained. Each drive circuit was tested for 1-1/2 hours, with sampling taking place every 5 minutes. The result was that the

RMS deviation of the readings using the new driver was a factor of 4 smaller than that obtained with the improved factory supplied driver.

Observation of the drive/reference waveform on an oscilloscope showed a symmetric sine wave, free of any switching transients. This feature may be advantageous in that a sinusoidal input is the optimum waveform for the reference channel of many lockin amplifiers.

APPENDIX D: SOLID STATE TEMPERATURE SENSOR

Because the temperature of the reaction cell could be varied over the range of 250 to 320 K, a method was needed to monitor both the average and the spatial variations of the cell temperature. Several types of sensors were considered for this purpose. Thermistors are very sensitive and relatively inexpensive, but have a nonlinear output versus temperature transfer function. Thermocouples are commonly used in this type of application, but require a cold-junction reference and produce an output voltage which is a quadratic function of temperature. The silicon transistor temperature transducer was ultimately chosen because of its linear output and long term stability.

The configuration employed is illustrated in Fig. D-1. This circuit takes advantage of the fact that a silicon transistor's base-emitter voltage is proportional to absolute temperature when the emitter current is held constant.[88] Ten identical circuits were constructed, with remotely locatable sensing transistors, as were ten variable voltage sources, to provide offsets for the final temperature readout. A rotary switch selected which sensor output and offset were displayed on the differential input digital voltmeter.

The circuits were calibrated by nulling the collector-base voltage with the linearity potentiometer, placing the sensor in a 0° C bath and adjusting the offset voltage for that sensor so the DVM read zero, and finally placing the sensor in a 50° C bath and adjusting the sensitivity potentiometer to get a 500 mV reading on the DVM. These last two adjustments had to be repeated several times until both conditions were met simultaneously.

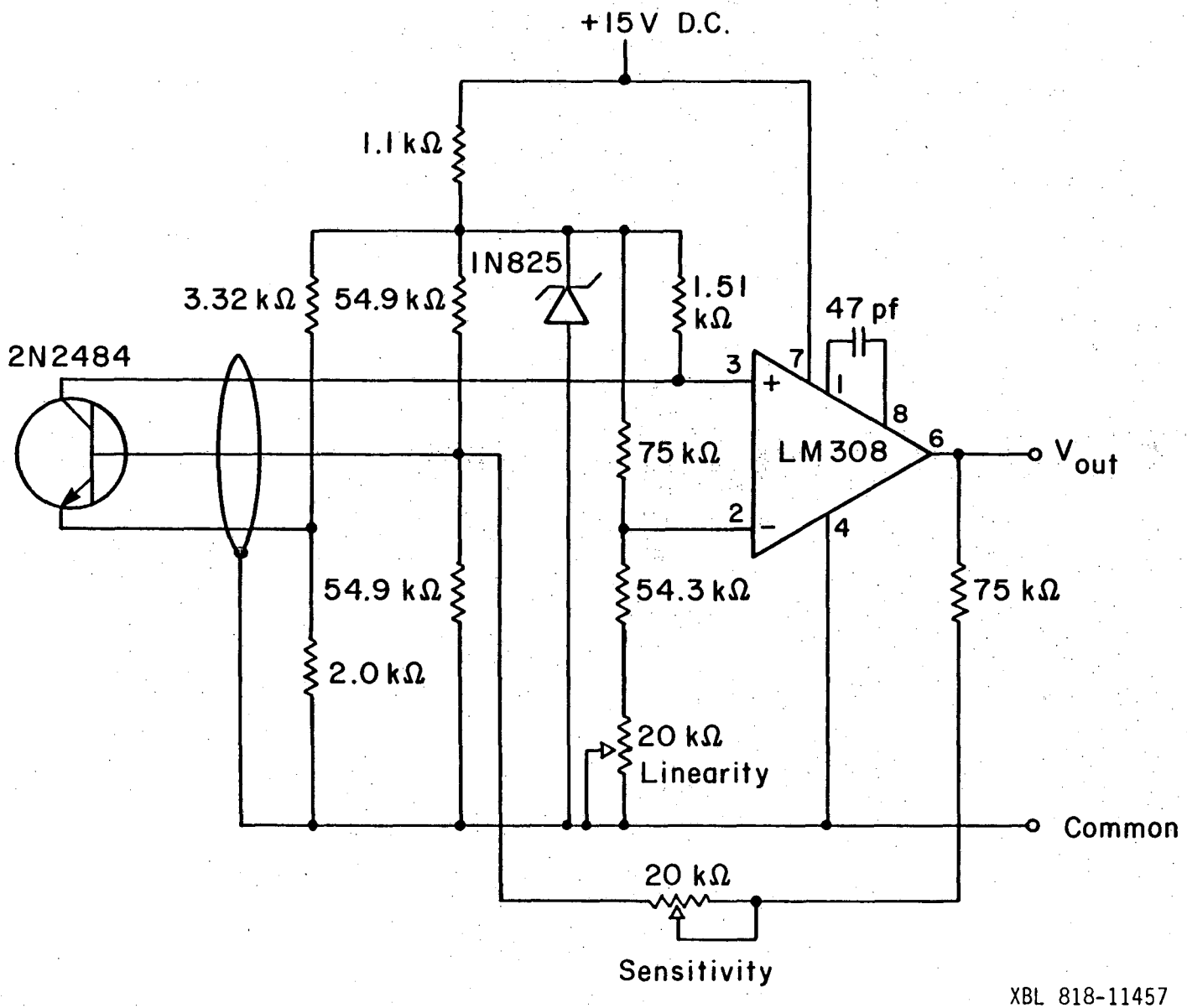

Fig. D-1. Solid state temperature sensor circuit schematic.

REFERENCES

1. D. D. Drysdale and A. C. Lloyd, Oxidation Combustion Review, (Elsevier, Amsterdam, 1970).
2. E. P. Dougherty and H. Rabitz, J. Chem. Phys. 72, 6571 (1980).
3. M. W. Werner, S. Beckwith, I. Gatley, K. Sellgren, G. Berriman, and D. L. Whiting, Astrophys. J. 239, 540 (1980).
4. D. F. Dickinson, C. A. Gottlieb, E. W. Gottlieb, and M. M. Litvak, Astrophys. J. 206, 79 (1976).
5. P. A. Leighton, Photochemistry of Air Pollution, (Academic Press, New York, 1961).
6. N. D. Sze, Science 195, 673 (1977).
7. J. G. Anderson, Geophys. Res. Lett. 3, 165 (1976).
8. H. S. Johnston and J. Podolske, Rev. Geophys. Space Phys. 16, 491 (1978).
9. H. S. Johnston, Science 173, 517 (1971).
10. J. G. Anderson, H. J. Grassl, R. E. Shetter, and J. J. Margitan, Geophys. Res. Lett. 8, 280 (1981).
11. G. H. Dieke and H. M. Crosswhite, J. Quant. Spect. Radiat. Transfer 2, 97 (1962).
12. J. L. Destombes, C. Marliere, and F. Rohart, J. Mol. Spect. 67, 93 (1977).
13. I. L. Chidsey and D. R. Crosley, J. Quant. Spect. Radiat. Transfer 23, 187 (1980).
14. A. Goldman and J. R. Gillis, J. Quant. Spect. Radiat. Transfer 25, 111 (1981).

15. A B. Meinel, Astrophys. J. 111, 555 (1950).

16. A B. Meinel, Astrophys. J. 112, 120 (1950).

17. J. P. Maillard, J. Chauville, and A. W. Mantz, J. Mol. Spect. 63, 120 (1976).

18. J. A. Coxon, Can. J. Phys. 58, 933 (1980).

19. J. R. Gillis and A. Goldman, J. Quant. Spect. Radiat. Transfer 26, 23 (1981).

20. F. Roux, J. D'Incan, and D. Cerny, Astrophys. J. 186, 1141 (1973).

21. R. K. Sparks, L. R. Carlson, K. Shobatake, M. L. Kowalczyk, and Y. T. Lee, J. Chem. Phys. 72, 140 (1980).

22. S. T. Amimoto, A. P. Force, J. R. Wiesenfeld, and R. H. Young, J. Chem. Phys. 73, 1244 (1980).

23. Chemical Kinetic and Photochemical Data for Use in Stratospheric Modelling, Evaluation No. 4, (NASA-Jet Propulsion Laboratory, Pasadena, CA. January 1981).

24. W. Demore and E. Tschuikow-Roux, J. Phys. Chem. 78, 1447 (1974).

25. D. D. Davis, M. O. Rodgers, S. D. Fischer, and K. Asai, Geophys. Res. Lett 8, 69 (1981).

26. J. P. Burrows, R. A. Cox, and R. G. Derwent, J. Photochem. 16, 147 (1981).

27. K. H. Becker, E. H. Fink, P. Langen, and U. Schurath, J. Chem. Phys. 60, 4623 (1974).

28. A. D. Walsh, J. Chem. Soc. 2260 (1953).

29. J. C. Gole and E. F. Hayes, J. Phys. Chem. 57, 360 (1972).

30. S. K. Shih, S. D. Peyerimhoff, and R. J. Buenker, Chem. Phys. 28, 299 (1978).

31. K. H. Becker, E. H. Fink, A. Leiss, and U. Schurath, Chem. Phys. Lett. 54, 191 (1978).

32. R. P. Tuckett, P. A. Freedman, and W. J. Jones, Mol. Phys. 37, 379 (1979).

33. H. E. Hunziker and H. R. Wendt, J. Chem. Phys. 60, 4622 (1974).

34. I. Glaschick-Schimpf, A. Leiss, P. B. Monkhouse, U. Schurath, K. H. Becker, and E. H. Fink, Chem. Phys. Lett. 67, 318 (1979).

35. P. D. Foo, T. Lohman, J. Podolske, and J. R. Wiesenfeld, J. Phys. Chem. 79, 414 (1975).

36. R. F. Heidner III, C. E. Gardner, T. M. El-Sayed, G. I. Segal, and J.V.V. Kaspar, J. Phys. Chem. 74, 5618 (1981).

37. S. T. Amimoto, A. P. Force, and J. R. Wiesenfeld, Chem. Phys. Lett. 60, 40 (1978).

38. H. Okabe, Photochemistry of Small Molecules (Wiley-Interscience, New York, 1978).

39. J. F. Butler, K. W. Nill, A. W. Mantz, and R. S. Eng, ACS Symposium Series 85, 12 (1978).

40. J. S. Margolis, R. T. Menzies, and E. D. Hinkley, Appl. Opt. 17, 1680 (1978).

41. M. S. Zahniser and M. E. Gersh, J. Chem. Phys. 75, 52 (1981).

42. S. S. Penner, K.G.P. Sulzmann, and H. K. Chen, J. Quant. Spect. Radiat. Transfer 13, 705 (1973).

43. J. Reid, M. El-Sherbiny, B. K. Garside, and E. A. Ballik, Appl. Opt. 19, 3349 (1980).

44. E. D. Hinkley, Laser Monitoring of the Atmosphere, (Springer-Verlag, New York, 1976), p. 269.

45. P. S. Connell, R. A. Perry, and C. J. Howard, Geophys. Res. Lett 7, 1093 (1980).

46. H. S. Johnston, G. E. McGraw, T. T. Paukert, L. W. Richard, and J. Van den Bogaerde, Proc. Natl. Acad. Sci. 57, 1146 (1967).

47. S. E. Schwartz, Ph.D. Thesis, University of California, Berkeley (1968).

48. D. R. Martin, Ph.D. Thesis, University of California, Berkeley (1973).

49. T. T. Paukert, Ph.D. Thesis, University of California, Berkeley (1969).

50. H. E. Huniker, IBM J. Res. Develop. 15, 10 (1971).

51. G. Z. Whitten, Rate Constant Evaluation Using a New Computer Modeling Scheme, presented at the ACS National Meeting (Spring, 1974).

52. G. Z. Whitten and J. P. Meyer, CHEMK: A Computer Modeling Scheme for Chemical Kinetics (Systems Applications, Inc., 1979).

53. C. W. Gear, Numerical Initial Value Problems in Ordinary Differential Equations, (Prentice-Hall, New Jersey, 1971).

54. A. C. Hindmarsh, Lawrence Livermore Laboratory Report UCID-30001, Rev. 3 (1974).

55. J. U. White, J. Opt. Soc. Am. 32, 285 (1942).

56. G. Hass and E. Ritter, J. Vacuum Sci. Tech. 4, 71 (1966).

57. D. Littlejohn, Ph.D. Thesis, University of California, Berkeley (1980).

58. EMI Photomultiplier Catalog, p. 10 (1979).

59. R. A. Graham, Ph.D. Thesis, University of California, Berkeley (1975).

60. G. A. Cook, A. D. Kiffer, C. U. Klumpp, A. H. Malik, and L. A. Spence, Ozone Chemistry and Technology-Advances in Chemistry No. 21 (1959), p. 44.

61. E.C.Y. Inn and Y. Tanaka, J. Opt. Soc. Am. 43, 870 (1953).

62. M. Griggs, J. Chem. Phys. 49, 857 (1968).

63. C. L. Lin, N. K. Rohatgi, and W. B. Demore, Geophys. Res. Lett. 5, 113 (1978).

64. L. T. Molina, S. D. Schinke, and M. J. Molina, Geophys. Res. Lett. 4, 580 (1977).

65. T. T. Paukert and H. S. Johnston, J. Chem. Phys. 56, 2824 (1972).

66. C. J. Hochanadel, J. A. Ghormley, and P. J. Ogren, J. Chem. Phys. 56, 4426 (1972).

67. S. R. Langhoff and R. L. Jaffe, J. Chem. Phys. 71, 1475 (1979).

68. H. H. Willard, L. L. Merritt, Jr., and J. A. Dean, Instrumental Methods of Analysis. (Van Nostrand Reinhold, New York, 1965), p. 91.

69. E.C.Y. Inn and Y. Tanaka, Ozone Chemistry and Technology-Advances in Chemistry Series No. 21 (1959), p. 263.

70. John Reid, private communication.

71. E. J. Hamilton, Jr., and R. R. Lii, Int. J. Chem. Kinet. 9, 875 (1977).

72. J. M. Flaud and C. Camy-Peyret, J. Mol. Spect. 55, 278 (1975).

73. R. A. Toth, J. Quant. Spect. Radiat. Transfer 13, 1127 (1973).

74. J. O. Hirschfelder, C. F. Curtiss and R. B. Bird, Molecular Theory of Gases and Liquids (John Wiley and Sons, New York, 1954), p. 1111.

75. K. H. Becker, W. Groth, and U. Schurath, Chem. Phys. Lett. 8, 259 (1971).

76. A. J. Krueger and R. A. Minzer, J. Geophys. Res. 81, 4477 (1976).

77. J. F. Noxon, Space Sci. Rev. 8, 92 (1968).

78. A. Goldman, private communication.

79. A Komornicki and R. L. Jaffe, J. Chem. Phys. 71, 2150 (1979).

80. J. D. Rogers and J. J. Hillman, J. Chem. Phys. 75, 1085 (1981).

81. R. T. Menzies, Geophys. Res. Lett. 6, 151 (1979).

82. J. G. Anderson, Geophys. Res. Lett. 3, 165 (1976).

83. J. Podolske, Rev. Sci. Instrum. 50, 1010 (1979).

84. A. C. Davies, IEEE Trans. Instrum. Meas. IM-18, 97 (1969).

85. D. Lancaster, Active Filter Cookbook, (Sams, Indianapolis, 1975).

86. J. Podolske, Rev. Sci. Instrum. 50, 1025 (1979).

87. J. G. Graeme, G. E. Tobey, and L. P. Huelsman, Operational Amplifiers-Design and Application (McGraw-Hill, New York, 1971).

88. R. A. Ruehle, Electronics 48, 127 (1975).

This report was done with support from the Department of Energy. Any conclusions or opinions expressed in this report represent solely those of the author(s) and not necessarily those of The Regents of the University of California, the Lawrence Berkeley Laboratory or the Department of Energy.

Reference to a company or product name does not imply approval or recommendation of the product by the University of California or the U.S. Department of Energy to the exclusion of others that may be suitable.

TECHNICAL INFORMATION DEPARTMENT
LAWRENCE BERKELEY LABORATORY
UNIVERSITY OF CALIFORNIA
BERKELEY, CALIFORNIA 94720